High-spin gamma-ray spectroscopy of doubly odd ^{124}La; signature inversion in $\pi h_{11/2} \otimes \nu h_{11/2}$ bands.

Thesis submitted in accordance with the requirements of
the University of Liverpool for the degree of Doctor in Philosophy

by

Hannah Jane Chantler

Oliver Lodge Laboratory

November 2002

Dedicated to the Chantlers and Hastings past and present.

Acknowledgements

I would like to take this opportunity to thank the following people, without whom the writing of this thesis would not have been possible.

- Prof. P.J. Nolan for all his supervision and support throughout my Ph.D. years, and for allowing me to be involved in experiments and conferences, both nationally and internationally.
- Dr. E.S. Paul for his ubiquity and dedication during my research, and for proof reading this thesis.
- Dr. N.J. Hammond and Dr. A.J. Boston for proof reading this thesis and, along with Dr. R.-D. Herzberg and Dr. J.F. Smith, for help and advice.
- Miss J.A. Sampson, Dr. J.R. Cresswell and Dr. I.M. Hibbert for all their support in computing matters.
- The Engineering and Physical Sciences Research Council (EPSRC) which has financed my studies and enabled me to attend experiments throughout Europe and the U.S.
- All the physicists I have met during my Ph.D. years: the Liverpool nuclear structure group past and present, all the other Ph.D. students in the Oliver Lodge laboratory, and the Stonybrook group. Particular thanks go to Chris, Jenny, Kit, Martina, Pascale and Taz.
- Neil, who has been a rock for as long as I have known him and shall be for many years to come.

It is the nature of all greatness not to be exact.

Edmund Burke (1729 1797)

Abstract

The doubly odd nucleus ^{124}La has been populated using the ^{64}Zn(^{64}Zn,3p1n) reaction in order to analyse the characteristic signature inversion that is known to be present in this mass region. The experiment was performed at the Argonne National Laboratory using a 260 MeV ^{64}Zn beam supplied by the ATLAS superconducting linear accelerator. The gamma-ray spectrometer Gammasphere was used in conjunction with the Microball charged-particle detector, the Neutron Shell and the Fragment Mass Analyser (FMA) to cleanly select the desired evaporation residues. High-spin states of ^{124}La have been observed and the level scheme extended with the addition of two new bands. The spin and parity of many states have been inferred for the first time due to the observation of linking transitions between four of the five observed bands. Comparison of band properties to cranking calculations has allowed configuration assignments to be made and includes the first identification of the $g_{9/2}$ proton-hole in an odd-odd lanthanum isotope. Two bands have been assigned a $\pi h_{11/2} \otimes \nu h_{11/2}$ structure; the yrast one exhibits a signature inversion in its energy levels below $I = 18.5\hbar$, while the excited one exhibits a signature inversion above $I = 18.5\hbar$.

Contents

Chapter 1

Introduction to Nuclear Structure

1.1 Introduction

The atomic nucleus displays a rich variety of phenomena, and an understanding of how the components of the nucleus interact to generate such phenomena is the fundamental aim of nuclear structure physics. One of the most valuable experimental techniques available to the nuclear structure physicist is gamma-ray spectroscopy. Developments in this field, for instance the construction of multi-detector arrays, have allowed increasingly exotic nuclei to be studied, with a progression to more extreme regions of the Segré chart.

The neutron-deficient A$\sim$120 mass region holds an abundance of nuclear structure information. Here the structures of nuclei are governed by the close proximity to the proton dripline and the presence of large nuclear deformation. This thesis pertains to the study of ^{124}La, which is both neutron deficient and doubly odd. Though many even-even and odd-mass lanthanum nuclei have been studied, much less is known of the doubly-odd light lanthanum systems.

The thesis is arranged as follows. An introduction to nuclear models and aspects of nuclear structure which relate to the A$\sim$120 region is given in this chapter. In Chapters 2 and 3, a discussion is given of the experimental techniques used in the present study of ^{124}La; the former providing an introduction into the field of gamma-ray spectroscopy while the latter discusses the specific techniques and equipment employed in the present study. In Chapter 4 the results of this study are presented, with a subsequent interpretation and discussion provided in Chapter 5. Finally, Chapter 6 presents the conclusions which have

been drawn from these investigations.

1.2 Nuclear deformation

A variety of models has been applied in the desire to gain an understanding of the nucleus. One early approach, the Liquid Drop Model (LDM), provides a macroscopic view, describing the nucleus as analogous to a drop of incompressible liquid; here the nucleus is treated as a sphere of constant density. However, though successful at describing certain *bulk* properties of the nucleus, the LDM proves unable to explain nuclear phenomena which result from the motion of individual nucleons. Specifically, some properties, such as nucleon separation energies, show evidence of a nuclear shell structure; certain nuclei, containing *magic numbers* of nucleons, appear to be particularly stable when compared to their neighbours. A shell model was therefore proposed, based upon a similar concept to the atomic Shell Model, namely the confinement of individual nucleons to "orbits" around a core. The nuclear Shell Model is used to reproduce the particular properties in which only the nucleons in the vicinity of the Fermi surface are involved, and is based upon the assumption that nucleons move almost independently in an average potential created by the interactions with all the other nucleons. The potential produced by the nucleons themselves and their mutual interactions is known as the *mean field.* Using a simple harmonic oscillator potential (SHO) to describe the mean field proves insufficient to produce the magic numbers however. The addition of a term proportional to $\mathbf{l}^2$, where $\mathbf{l}$ is the orbital angular momentum, which effectively flattens the potential towards the centre and makes the walls of the well steeper, yields a more "realistic" potential but still fails to reproduce the observed magic numbers. It is only with the addition of a spin-orbit interaction ($\mathbf{l} \cdot \mathbf{s}$), that the magic numbers are reproduced by the nuclear Shell Model. This coupling gives rise to a splitting in otherwise degenerate levels with $j = l \pm \frac{1}{2}$, where j denotes the total angular momentum of the nucleon. The spin-orbit interaction is chosen to be attractive to account for the experimental observation that $l + \frac{1}{2}$ orbitals are energetically always below the $l - \frac{1}{2}$ orbitals, the difference (splitting) increasing with an increase in l.

In nuclear systems which lie far from the magic numbers, that is those nuclei which possess several valence nucleons, experimental features are observed which suggest collective motion. Examples of such features are: rotational bands, the fission process, large

quadrupole moments and strongly enhanced quadrupole transition probabilities. These effects, which occur due to the correlated motion of nucleons, are evidence of nuclear deformation [Rin80].

1.3 The Nilsson model

Correlated nucleonic motion occurs through the long range residual interactions of the nucleon-nucleon force, where the term "residual" here refers to those components of the force which are non-central and are not covered by the spin-orbit interaction. As the number of valence nucleons increases, these residual interactions become increasingly dominant and the Spherical Shell Model discussed so far becomes intractable. An alternative approach is therefore required. Nilsson proposed the use of a deformed potential to approximate the effects of the long-range residual interaction [Nil55]. By making the mean field deformed, the nuclear shape is constrained to be deformed also. This approach, which is also referred to as the deformed shell model, is useful for the study of single particle nature in a deformed nuclear system [Boh51] [Rai76] [Rai50].

1.3.1 The anisotropic harmonic oscillator (AHO) potential

Assuming that an ellipsoidal distribution represents the density of a deformed nucleus, it follows that the mean field potential should be of the same shape. Following the harmonic oscillator approach, this is achieved using the anisotropic harmonic oscillator to describe the mean field,

$$h_0 = -\frac{\hbar^2}{2m}\Delta + \frac{m}{2}(\omega_x^2 x^2 + \omega_y^2 y^2 + \omega_z^2 z^2). \tag{1.1}$$

Here, the frequencies ω_x, ω_y, ω_z, are proportional to the inverse half axes of the ellipsoid and thus give the condition for the volume conservation as:

$$\omega_x\omega_y\omega_z \;=\; \text{const} \;=\; \omega_0^3. \tag{1.2}$$

The Hamiltonian given in Eq. 1.1 is separable in x, y, z, where the eigenstates are characterised by the quantum numbers n_x, n_y, n_z, giving the following eigenvalues:

$$\epsilon_0(n_x, n_y, n_z) \;=\; \hbar\omega_x\left(n_x + \frac{1}{2}\right) + \hbar\omega_y\left(n_y + \frac{1}{2}\right) + \hbar\omega_z\left(n_z + \frac{1}{2}\right). \tag{1.3}$$

In the case of the axially symmetric shapes, the z-axis is commonly chosen as the symmetry axis ($\omega_x = \omega_y \neq \omega_z$) and a deformation parameter δ can be introduced by the following definitions:

$$\omega_\perp^2 = \omega_x^2 = \omega_y^2 = \omega_0^2(\delta)(1 + \tfrac{2}{3}\delta), \tag{1.4}$$

$$\omega_z^2 = \omega_0^2(\delta)(1 - \tfrac{4}{3}\delta), \tag{1.5}$$

where δ is a deformation parameter and ω_0 is the oscillator frequency in the spherical $\delta = 0$ case. The determination of $\omega_0(\delta)$ is made in such a way that volume conservation is guaranteed, enabling the single-particle states to be calculated as a function of the deformation parameter δ. More commonly however, with the introduction of non-Cartesian coordinates, another deformation parameter ε is introduced. This distortion parameter is obtained from $\varepsilon = (\omega_\perp - \omega_z)/\omega_0$ and is defined such that $\varepsilon > 0$ and $\varepsilon < 0$ correspond to prolate and oblate shapes, respectively.

1.3.2 The Nilsson Hamiltonian

The addition of the $\mathbf{l}^2$ and $\mathbf{l}\cdot\mathbf{s}$ terms to the anisotropic harmonic oscillator potential gives the enhanced Hamiltonian:

$$h = -\frac{\hbar^2}{2m}\Delta + \frac{m}{2}\omega_\perp^2(x^2+y^2) + \frac{m}{2}\omega_z^2 z^2 + C\mathbf{l}\cdot\mathbf{s} + D\mathbf{l}^2 \tag{1.6}$$

$$= \hbar\omega_0(\delta)\left(-\frac{1}{2}\Delta' + \frac{1}{2}r'^2 - \beta r'^2 Y_{20}\right) - \kappa\hbar\omega_0\left(2\mathbf{l}\cdot\mathbf{s} + \mu\mathbf{l}^2\right), \tag{1.7}$$

where κ and μ are coefficients which determine the strength of the $\mathbf{l}\cdot\mathbf{s}$ and $\mathbf{l}^2$ terms respectively, and are different for each major oscillator shell. The constants C and D are given by:

$$C = -2\hbar\omega_0\kappa, \qquad D = -\hbar\omega_0\kappa\mu, \tag{1.8}$$

with C representing the strength of the spin orbit force and $D\mathbf{l}^2$ shifting the levels with higher l-values lower in energy. For states with large N quantum numbers, N defining the major oscillator shell, this shift of the levels is too strong and must be compensated using the following replacement [Gus67]:

$$D\left(\mathbf{l}^2 - \langle\mathbf{l}^2\rangle_N\right), \tag{1.9}$$

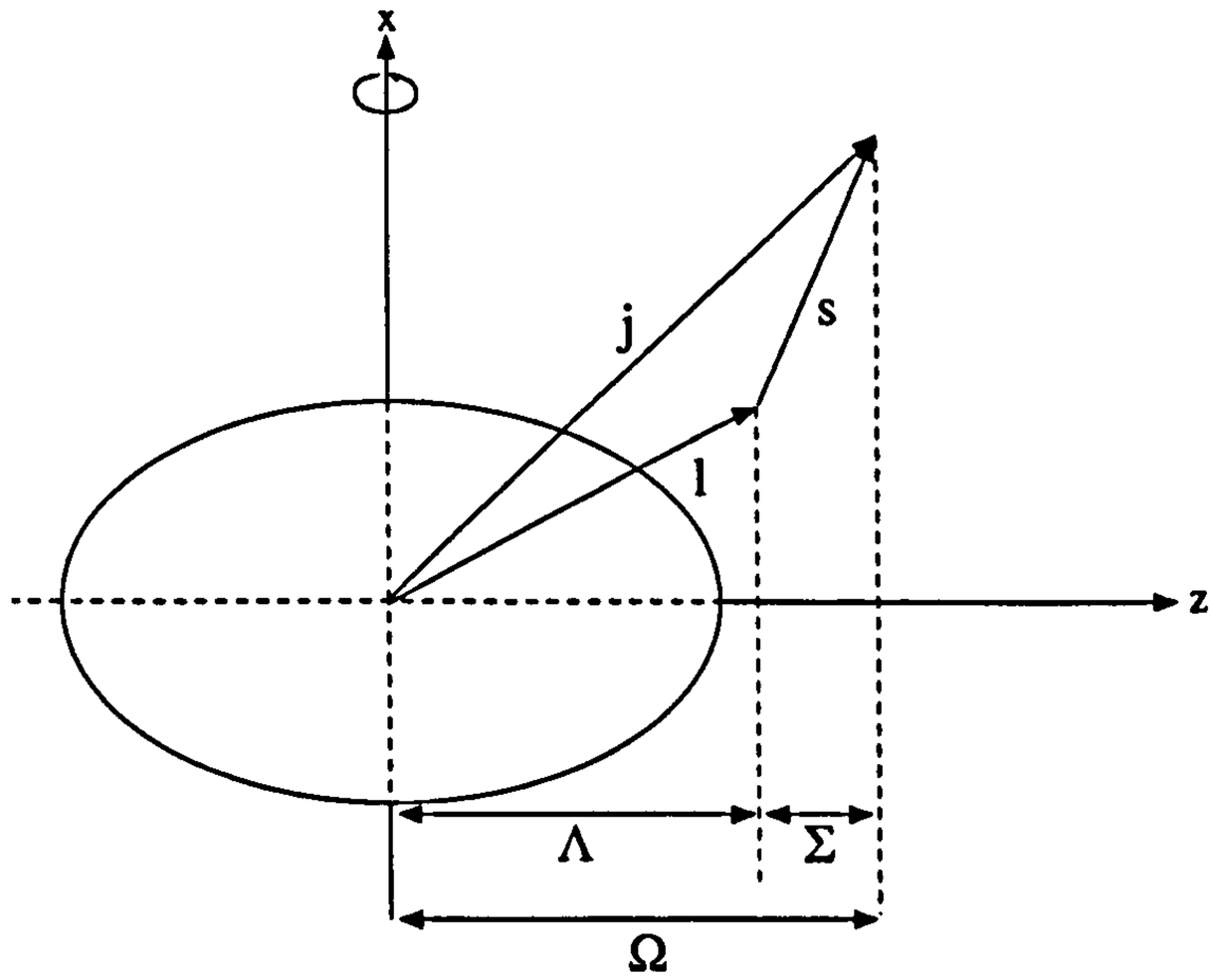

Figure 1.1: An illustration of how the orbital angular momentum **l**, the intrinsic spin angular momentum **s**, and the single-particle angular momentum **j**, are related. The projection of **l** and **s** onto the symmetry axis are denoted by Λ and Σ respectively, where $\Lambda + \Sigma = \Omega$ and $\Sigma = \pm 1/2$.

where $\langle \mathbf{l}^2 \rangle_N = \frac{1}{2}N(N+3)$ is the expectation value of $\mathbf{l}^2$ averaged over one major shell with quantum number N. Under deformation, l and j are no longer good quantum numbers, the only quantum numbers which are now conserved are the parity π, and Ω, the eigenvalue of j_z. The Nilsson Hamiltonian can be used to evaluate the total energy of a particular nuclear configuration as a function of deformation. Plotting the energies of individual nucleon orbitals against deformation yields a Nilsson diagram such as those shown in Figs. 1.2 and 1.3 for neutrons and protons respectively. The Nilsson orbitals are labelled using the asymptotic quantum numbers,

$$[Nn_z\Lambda]\Omega^\pi. \tag{1.10}$$

Here, N is the total number of oscillator quanta, n_z is the number of oscillator quanta along the symmetry axis, Λ is the projection of **l** onto the symmetry axis and $\Omega = \Lambda \pm \frac{1}{2}$ is the projection of **j** onto the symmetry axis, as illustrated in Fig. 1.1.

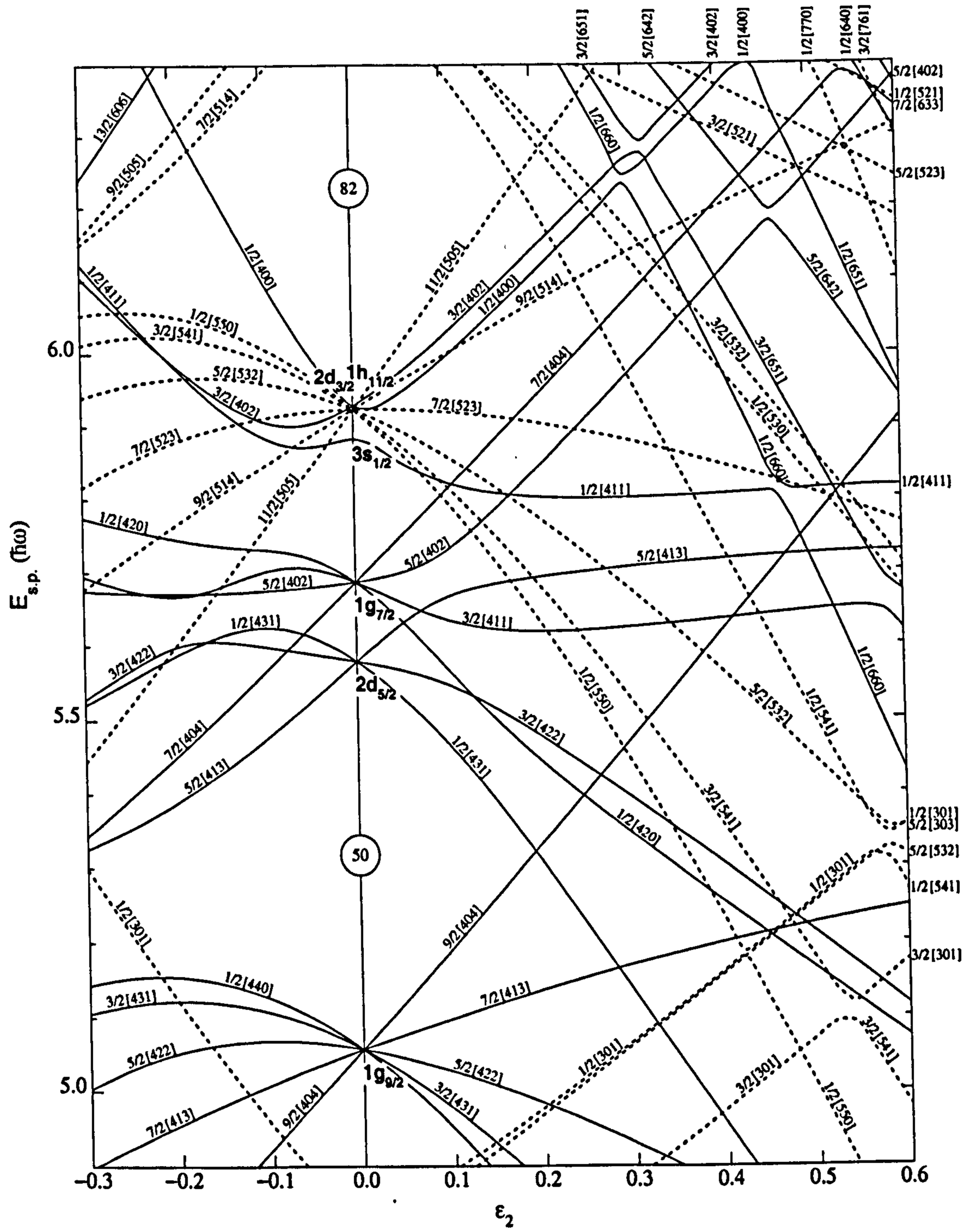

Figure 1.2: A Nilsson diagram for neutrons with $50 \leq N \leq 82$. Solid lines show positive-parity states and dashed lines show negative-parity states. The states are labelled by the asymptotic quantum numbers and the energies are given as a function of the quadrupole deformation parameter ε_2, with higher orders of deformation set to zero.

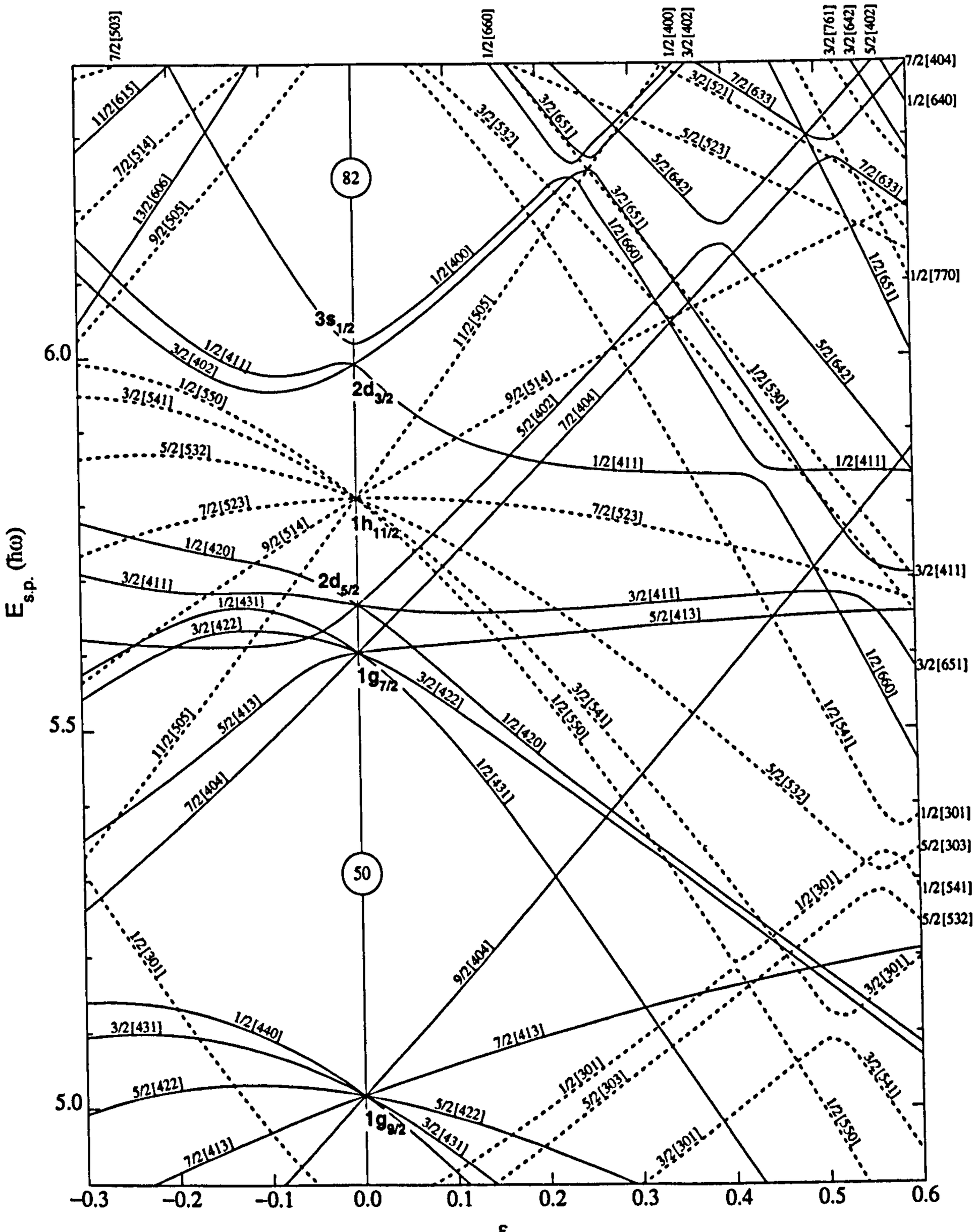

Figure 1.3: Nilsson diagram for protons with $50 \leq N \leq 82$. Solid lines show positive-parity states and dashed lines show negative-parity states. The states are labelled by the asymptotic quantum numbers and the energies are given as a function of the quadrupole deformation parameter ϵ_2, with higher orders of deformation set to zero.

1.4 Strutinski shell correction procedure

The Nilsson Model provides a useful description of the single-particle potential of the nucleus, but it does fail to reproduce the bulk properties of the nucleus to which all, or many, of the nucleons contribute. Strutinski proposed a hybrid method [Str67] [Str68] which employs the single-state descriptions of the Deformed Shell Model and augments them with the bulk predictions of the Liquid Drop Model [Mye69] [Boh53] [Eis70], thus taking into account both microscopic and macroscopic influences. The correction involves the separation of the total energy E_{total} into two terms:

$$E_{total} = E_{smooth} + E_{oscillating} \tag{1.11}$$

where E_{smooth} represents the LDM contribution and $E_{oscillating}$ corresponds to the fluctuations from shell effects which can be found from the Nilsson Model. Further dissection of the shell model energy is required to separate an oscillating term given as δE_{shell}, from a smooth contribution $\tilde{E}_{shell}$ (which is effectively to be replaced by the LDM). The Shell Model energy can thus be described as:

$$E_{shell} = \tilde{E}_{shell} + \delta E_{shell}. \tag{1.12}$$

Here it is advantageous to introduce the concept of the level density $g(\epsilon)$ by defining $g(\epsilon)d\epsilon$ as the number of levels in the energy interval between ϵ and $\epsilon + d\epsilon$; as E_{shell} is given by,

$$E_{shell} = \sum_{i=1}^{A} e_i, \tag{1.13}$$

it can also be given in terms of the density function $g(e)$,

$$E_{shell} = \int_{-\infty}^{\lambda} \epsilon g(\epsilon) d\epsilon. \tag{1.14}$$

Here, λ is the Fermi energy. In the Shell Model approach λ is not defined exactly, but is arbitrarily taken to be between the last filled and first unfilled level. The smoothed Shell Model energy is taken to be,

$$\tilde{E}_{shell} = \int_{-\infty}^{\tilde{\lambda}} \epsilon \tilde{g}(\epsilon) d\epsilon, \tag{1.15}$$

where the averaged density function $\tilde{g}(\epsilon)$ is used to smooth out the single-particle effects. Equation 1.12 can now be used to ascertain δE_{shell}, which can subsequently be used to

approximate $E_{oscillating}$ in Eq. 1.11, yielding the full macroscopic plus microscopic energy. If the Nilsson model is used to obtain the microscopic term then E_{total} can be plotted as a function of deformation and subsequently minimised to find the equilibrium deformation of the nucleus. An accurate reproduction of the experimental ground state energies, as well as the dependence on the deformation parameters, can be achieved with this approach.

1.5 Deformed Woods-Saxon potential

The Woods-Saxon potential is a more realistic description of the nuclear mean field potential than the harmonic oscillator. Specifically, its form is close to that of the charge density of the nucleus. Like the harmonic oscillator it can be extended to include deformation, giving the deformed Woods-Saxon potential,

$$V(r,\theta,\phi) = -V_0\left[1+\exp\left(\frac{r-R(\theta,\phi)}{a(\theta,\phi)}\right)\right]^{-1}, \tag{1.16}$$

where the parameter a describes the diffuseness of the nuclear surface and is approximately constant over all nuclei if spherical. However, to obtain a constant diffuseness for deformed nuclei, a is required to be a function of the angles θ and ϕ [Boh75] [Bra72]. Within the context of the Woods-Saxon potential, the nuclear surface is parametrised in terms of deformation parameters β - which will be defined shortly, in contrast to the ϵ parametrisation associated with variants of the harmonic oscillator potential. The expression for the Hamiltonian is defined as:

$$H = \frac{-\hbar}{2m}\nabla^2 + V_{WS} - f(r)\mathbf{l}\cdot\mathbf{s}, \tag{1.17}$$

with the spin-orbit term again added to reproduce the magic shell numbers. Single particle energies included in this work have been calculated assuming a deformed Woods-Saxon potential using the code WSBETA [Cwi87] with the universal parameter set [Naz85].

1.6 Definition of the nuclear shape

Only in nuclei with non-spherical equilibrium is rotational motion observed, where the shape of the nucleus is most commonly represented by an ellipsoid of revolution. In order to parameterise a deformed nucleus the assumption is made that a sharp-surfaced spherical nucleus has undergone either a dynamical, shape or surface, oscillation. However, before

such oscillations can be investigated, the surface of the nucleus must be specified. This is commonly achieved using the length of a radius vector pointing from the origin to the surface:

$$R(\theta,\phi) = R_0\left(1 + \alpha_{00} + \sum_{\lambda=1}^{\infty}\sum_{\mu=-\lambda}^{\lambda}\alpha_{\lambda\mu}Y_{\lambda\mu}(\theta,\phi)\right), \tag{1.18}$$

where R_0 is the radius of a sphere with the same volume. This multipole expansion of the nuclear radius is given in terms of the spherical harmonics $Y_{\lambda\mu}(\theta,\phi)$ of λ^{th} order deformation with a projection of μ onto the symmetry axis. The extent of the deformation is governed by the shape parameters $\alpha_{\lambda\mu}$, and the term α_{00} ensures volume conservation. For axially-symmetric deformations, the z-axis is chosen as the symmetry axis and $\alpha_{\lambda\mu}$ disappears except when $\mu = 0$. The deformation parameters $\alpha_{\lambda 0}$ are then referred to as β_λ, the same parameters used in the Woods-Saxon parameterisation, where λ is the multipolarity of the oscillations. The oscillations corresponding to $\lambda = 2$ look like ellipsoidal deformations. In the case of the $\lambda = 2$ quadrupole deformation, if the $\alpha_{2\mu}$ coefficients are defined in the system of principal axes, α_{20} and $\alpha_{22} = \alpha_{2-2}$ as $\alpha_{21} = \alpha_{2-1} = 0$, and so the five $\alpha_{2\mu}$ coefficients are reduced to the two independent coefficients, α_{20} and α_{22}. These two coefficients, together with the three Euler angles (describing the transformation from laboratory to intrinsic frames and thus the orientation of the nucleus in space), completely define the system. However, it is convenient to replace the α_{20} and α_{22} coefficients with the Hill-Wheeler [Hil53] polar coordinates, β_2 and γ ($\beta_2 > 0$) through the relations:

$$\begin{aligned} \alpha_{20} &= \beta_2 \cdot \cos\gamma, \\ \alpha_{22} &= \frac{1}{\sqrt{2}} \cdot \beta_2 \cdot \sin\gamma, \end{aligned} \tag{1.19}$$

from which:

$$\sum_{\mu} |\alpha_{2\mu}|^2 = \alpha_{20}^2 + 2\alpha_{22}^2 = \beta_2^2. \tag{1.20}$$

The $\lambda = 2$ shapes are displayed in Fig. 1.4 as represented by the polar coordinates β_2 and γ, known as the Lund convention [And76]. Values of $\gamma = 0°$, $120°$ and $240°$ yield prolate spheroids, γ values of $60°$, $180°$ and $300°$ lead to corresponding oblate shapes, and when γ is not a multiple of $60°$, the nucleus has a triaxial shape ($x \neq y \neq z$).

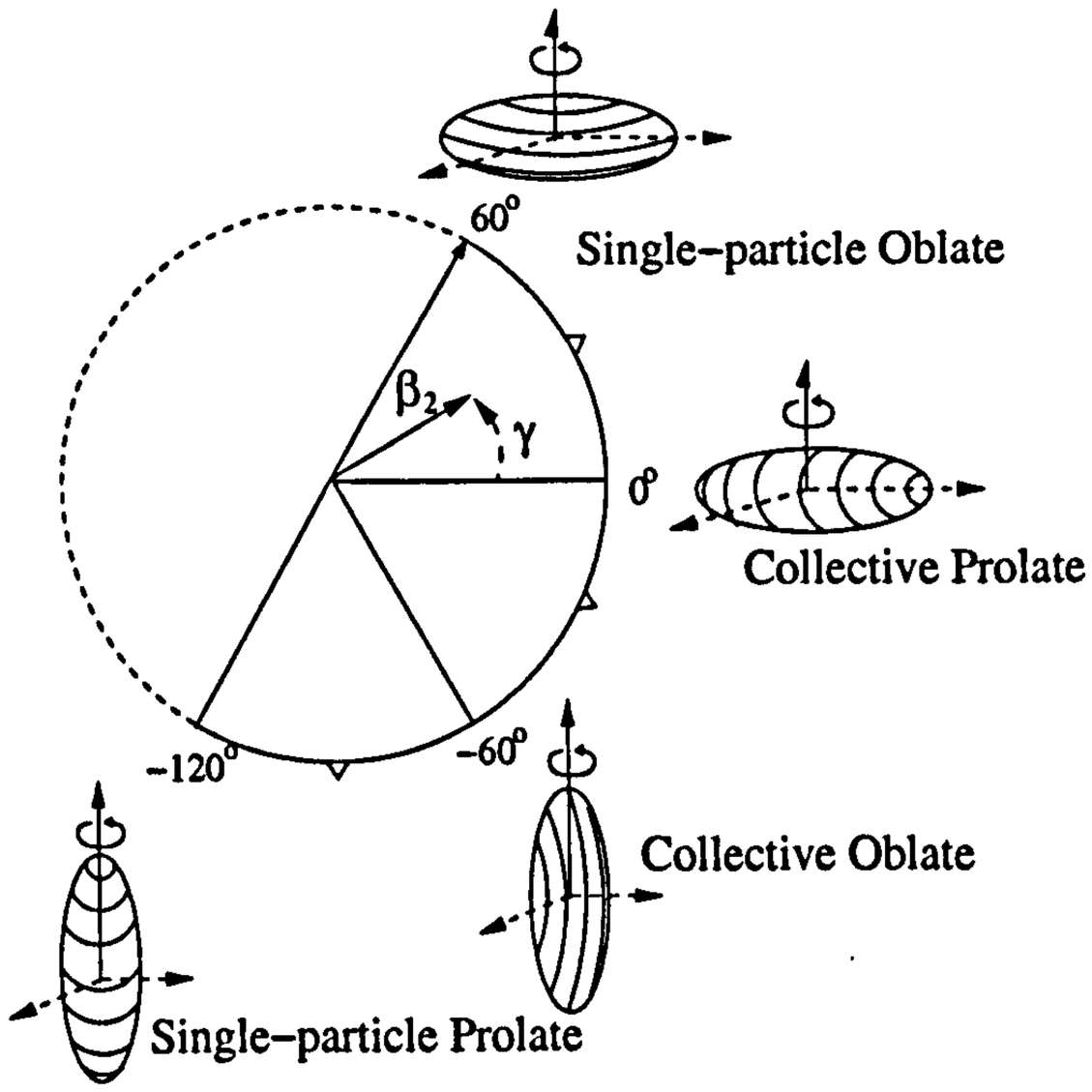

Figure 1.4: The Lund convention, describing quadrupole nuclear shapes in the β_2, γ plane.

1.7 Pairing and Quasiparticles

The effects of pairing are experimentally very evident, two prime examples are:

- the ground states of all even-even nuclei have $I^\pi = 0^+$.
- non-collective excitation energies of even-even nuclei exhibit a large energy gap (of approximately 1.5 MeV).

In order to reproduce these observations, an addition to the average central potential is needed from the short-range part of the nucleon-nucleon interaction [May50]. The pairing interaction is effective when the spatial overlap of particles is high, and as the Pauli principle restricts two particles to possess identical orbits, the greatest overlapping of particles occurs for those in *time reversed* orbitals. In this way the spins cancel and the pair produces a net contribution of $I^\pi = 0^+$. Without the effects of pairing all levels would be occupied with consecutive particles up to the Fermi surface, while those levels above would be empty. However, it is possible for time-reversed paired particles to scatter from one orbit to another,

creating partially (time averaged) filled orbits, leading to a smearing of the Fermi surface over the region $\pm\Delta$, where Δ is the pairing gap parameter.

With the application of the Bogoliubov-Valatin transformation [Bog58] it is possible to describe this system as a gas of *non-interacting quasiparticle excitations.* The common referral to these quasiparticles is as a combination of particles and holes; an unoccupied particle state being equivalent to an occupied hole state. The total state can be described in terms of the occupation amplitudes given by:

$$U_\nu = \frac{1}{\sqrt{2}}\left[1+\frac{\epsilon_\nu+\lambda}{E_\nu}\right]^{1/2};\ V_\nu = \frac{1}{\sqrt{2}}\left[1+\frac{\epsilon_\nu-\lambda}{E_\nu}\right]^{1/2};\quad |\,U_\nu\,|^2+|\,V_\nu\,|^2=1, \tag{1.21}$$

where ϵ_ν are the energies of the single-particle states, λ is the Fermi level, E_ν is quasiparticle excitation energy of the state, and $|V_\nu|^2$ and $|U_\nu|^2$ are the probabilities of occupation and non-occupation, respectively.

1.8 Rotational states in deformed nuclei

Rotation is an example of collective motion and is characterised by the coherent movement of a large number of nucleons. However, if a quantum mechanical description is required then it is important to observe that collective motion cannot be defined about a symmetry axis; such rotation would change only a minor phase factor in the wavefunction, which is in direct contrast to collective rotation. Instead, the description is based upon small angular momentum contributions from a large number of particles; the wavefunction of these particles changing slowly with increasing angular momentum. This implies that only deformed nuclei can rotate collectively and an axially symmetric nucleus would have only one rotation axis perpendicular to the symmetry axis. The following Hamiltonian can therefore be defined by analogy with the classical moment of inertia $\mathcal{I}$:

$$H_{rot} = \frac{R^2}{2\mathcal{I}}E_I = \frac{\hbar^2}{2\mathcal{I}}I(I+1), \tag{1.22}$$

where R is the angular momentum generated by the collective motion of the nuclei, see Fig. 1.5 and I is the total angular momentum. The rotational bands that are found experimentally are the eigenvalues of this Hamiltonian. The quantum number K, as illustrated in Fig. 1.5, is defined as the projection of I onto the symmetry axis, and as it is not determined

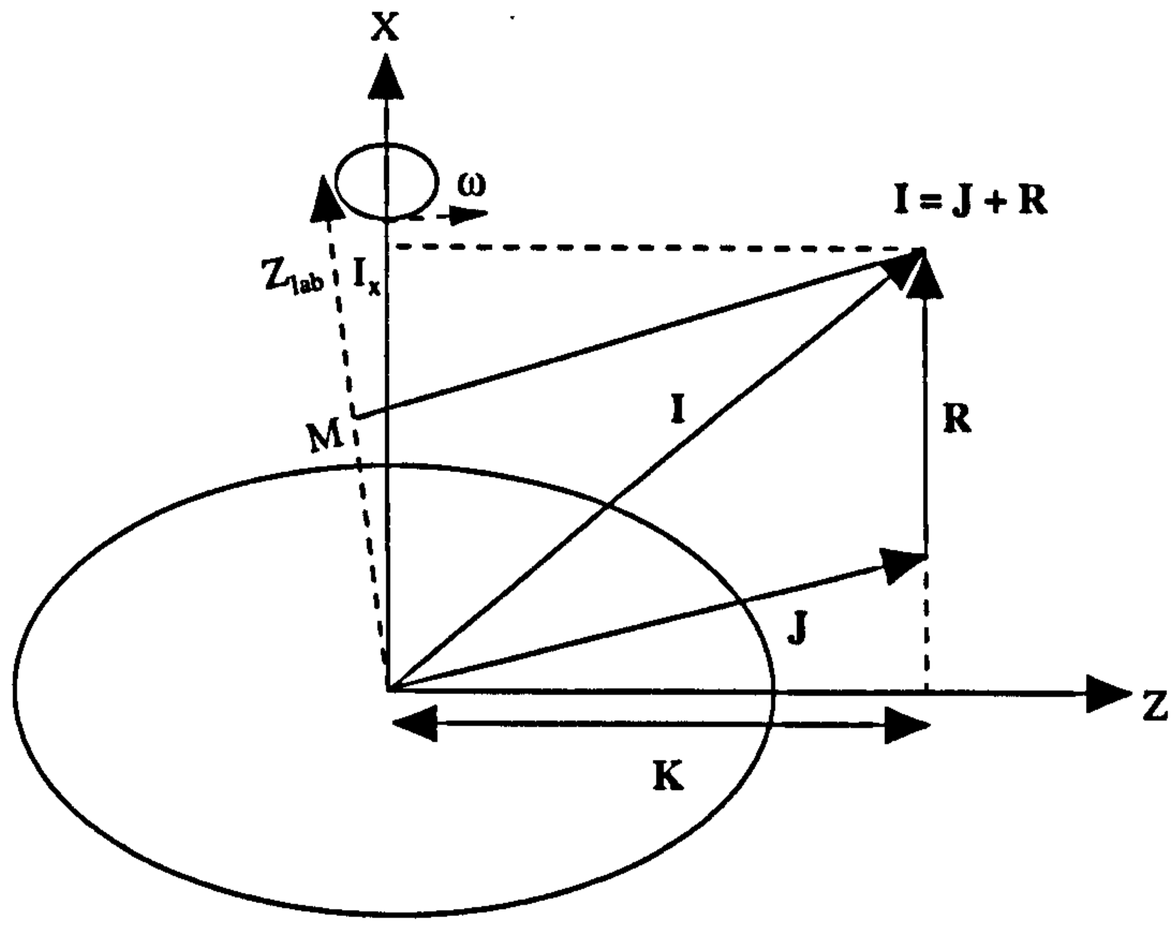

Figure 1.5: For an axially symmetric shape, rotation about the symmetry axis is quantum mechanically forbidden. The projections $I_x = J_x = K\hbar$ are conserved quantities for rotational motion about an axis perpendicular to the symmetry axis (x). **R** is the collective rotation of the core, **J** is the total single-particle angular momentum, and **I** is the total angular momentum of the nucleus. The projection of **I** onto the symmetry axis is denoted by K.

by R, it is a convenient label with which to assign rotational bands. The rotational energy can be expressed as:

$$E_{rot} = \frac{\hbar^2}{2\mathcal{J}}[I(I+1) - K^2]. \tag{1.23}$$

For $K \neq 0$ the total nuclear wavefunction takes the antisymmeterised form in order to satisfy invariance with respect to rotation by 180° and leads to a sequence of rotational states with spins:

$$I = K, K+1, K+2, ... \tag{1.24}$$

1.8.1 The particle rotor model

The description of the interplay between the motion of single particles and the collective rotation of the nuclear core is based upon the coupling of the few valence particles, which move relatively independently in the deformed well of the core, and the collective rotation of the remaining particles [Boh53]. Although the division between the core and the valence

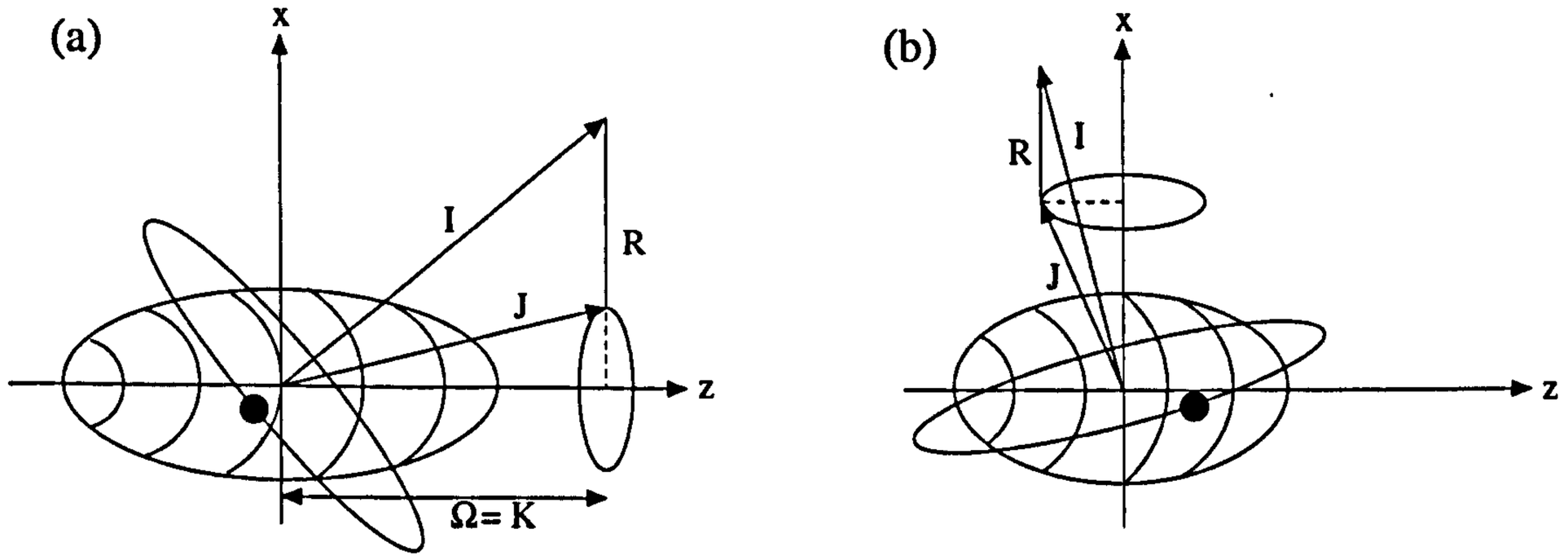

Figure 1.6: The two extremes of particle-rotor coupling. (a) shows the strong coupling limit where the odd particle aligns with the symmetry axis. (b) shows the decoupled limit with the odd particle aligning its angular momentum with the rotation axis.

particles is not uniquely defined, it is reasonable to use the unpaired nucleon in an odd-mass nucleus as a valence nucleon coupled to an even-even core. The Hamiltonian can be divided into two parts, the intrinsic part H_{int} which deals microscopically with the valence particle, or whole subgroup of particles near the Fermi level, and a phenomenological part H_{coll} which describes the inert core:

$$H = H_{int} + H_{coll}. \tag{1.25}$$

Two extremes of the nucleon-core coupling can be defined in terms of the relative effects of the core deformation and the strength of the Coriolis interaction. Fig. 1.6 shows the strong-coupling limit or deformation aligned (DAL) scheme (a), and the weak-coupling or rotation aligned (RAL) scheme (b). When the energy splitting of single-particle excitations are large compared with the Coriolis interaction matrix elements, the DAL limit is realised. The angular momentum **J** of the valence particles is strongly coupled to the motion of the core. The RAL limit is reached when the nucleus is rotating rapidly or is only weakly deformed. In such cases the Coriolis force tends to overcome the coupling of the particle to the deformed core. The Coriolis interaction aligns the angular momentum **J** of the valence particle with the rotational angular momentum **R**. In the case of an odd-odd nucleus with two valence particles (one valence proton and one valence neutron), K is defined by the

vector addition of the single-particle Ω values:

$$K = |\Omega_\pi \pm \Omega_\nu|. \tag{1.26}$$

1.8.2 Moments of inertia

The static moment of inertia of a rotating nucleus is found to be typically 50–80% of the rigid body value and is given by:

$$\mathcal{I}_{rig} = \frac{2}{5} AMR_0^2 \left(1 + \frac{1}{3}\beta_2\right) (\hbar^2 \mathrm{MeV}^{-1}), \tag{1.27}$$

where $R_0 = 1.2A^{1/3}$. For a general function $E = E(I)$, however it seems natural to define moments of inertia from the derivatives given by Bohr and Mottelson [Boh81] to reveal more of the intrinsic nuclear structure. These are the *kinematic* $\mathcal{I}^{(1)}$ and *dynamic* $\mathcal{I}^{(2)}$ moments of inertia. Note that $\mathcal{I}^{(1)}$ and $\mathcal{I}^{(2)}$ can be defined as in classical mechanics by:

$$\frac{\hbar^2}{\mathcal{I}^{(1)}} = 2\frac{dE}{dI^2} \approx \frac{E(I+1) - E(I-1)}{2I-1}, \tag{1.28}$$

and

$$\frac{\hbar^2}{\mathcal{I}^{(2)}} = \frac{d^2E}{dI^2} \approx \frac{E(I+2) - 2E(I) + E(I-2)}{4}, \tag{1.29}$$

where these moments of inertia can also be defined from experimentally measured transition energies, $E_\gamma = E(I+1) - E(I-1)$. The kinematic moment of inertia is a direct measure of the transition energies. The dynamic moment of inertia is very configuration dependent and sensitive to band crossings, and is obtained from the differences in adjacent transition energies.

1.9 Cranking

The cranking model is an approach that takes into account the semi-classical processes of rotation and the application of the mean field approximation. This approach is very useful in the interpretation of nuclear states with large angular momentum. Almost all microscopic theories of nuclear rotation are based on the cranking model, which was originated by Inglis [Ing54] [Ing56]. The cranking approach has the following advantages.

- Collective rotation as well as single-particle rotation, and all transitions in between, can be handled on the same footing.

- The model is correct for large angular momenta, where classical arguments apply but quantum mechanical derivation does not.

If a coordinate system is introduced that rotates with a constant angular velocity ω around a fixed axis in space, the motion of the nucleons in the rotating frame is simple if the angular frequency is properly chosen. The nucleons can be visualised as independent particles moving in an average potential well which is rotating with the coordinate frame. A single-particle potential V is defined, which rotates in fixed space with a fixed shape, giving an explicit time dependence in the many-body Schrödinger equation:

$$i\hbar\frac{\partial}{\partial t}\psi_t = h_t\psi_t. \tag{1.30}$$

For an axially symmetric deformation the time dependence can be eliminated using the rotation operator:

$$U = e^{-i\omega I_x t}, \tag{1.31}$$

which is now transformed into the intrinsic frame. The operator, U, produces the rotation of an angle ωt around the rotational axis x, and I_x is the component of the total angular momentum along the rotation axis x. As the time-dependent operator,

$$h_t = U h_{int} U^{-1}, \tag{1.32}$$

then

$$\psi_t = U\psi_{int}, \tag{1.33}$$

where the subscript *int* refers to the intrinsic (body-fixed) frame. By substituting the above expressions into Eq. 1.30 the Schrödinger equation therefore becomes:

$$i\hbar\frac{\partial}{\partial t}\psi_{int} = (h_{int} - \hbar\omega I_x)\psi_{int}. \tag{1.34}$$

The requirement that ω is parallel to a principal axis is the basis of the principal axis cranking (PAC) model and the potential gives the many-body Hamiltonian of the cranking model, or *Routhian*,

$$H_\omega = H_{int} - \hbar\omega I_x, \tag{1.35}$$

where H_{int} is the sum of deformed single-particle Hamiltonians, and the second term relates to the classical centrifugal and Coriolis forces. Routhians are so-named from the Routh functions of classical mechanics, and are defined as the Hamiltonians of the rotating frame of reference.

1.9.1 The Cranked Shell Model

For a fixed angular momentum, Eq. 1.35 can now be solved using the cranked shell model, which gives the cranking Hamiltonian in terms of single-particle states:

$$H_\omega = \sum_{i=1}^{A} h_\omega(i) = \sum_i [h_{int}^{(i)} - \hbar\omega j_x(i)], \tag{1.36}$$

where $j_x(i)$ is the angular momenta of the ith nucleon projected onto the rotational axis. From this relation, the single-particle Routhians can be calculated by solving the following eigenvalue equation,

$$h_\omega|\nu_\omega\rangle = e_\omega^\nu|\nu_\omega\rangle, \tag{1.37}$$

where the single-particle eigenfunctions in the rotating frame are denoted by $|\nu_\omega\rangle$. The real expectation energies are given by the expectation values of the intrinsic single-particle Hamiltonian:

$$e_\omega = \langle\nu_\omega|h_{int}|\nu_\omega\rangle = e_\omega^\nu + \hbar\omega\langle\nu_\omega|j_x|\nu_\omega\rangle. \tag{1.38}$$

The differentiation of the above equation yields:

$$\frac{de_\omega^\nu}{d\omega} = -\hbar\langle\nu_\omega|j_x|\nu_\omega\rangle. \tag{1.39}$$

This relation shows that orbitals with the largest components of angular momentum along the axis of rotation, and hence the smallest values of Ω, exhibit the largest variation in rotational energy with respect to the rotational frequency.

1.9.2 Tilted Axis Cranking (TAC)

The cranking model as described thus far, is largely based upon a common rotation about a principal axis, however this model can also be used in the description of rotation about an axis other than the principal axes of the nuclear density distribution. Bengtsson [Ben93] illustrated that the only generalisation required is that the one-dimensional cranking term, $-\omega j_k$, where k can refer to any of the three principal axes, is replaced by the general cranking term $-\boldsymbol{\omega}\cdot\boldsymbol{j}$. The vector $\boldsymbol{\omega}$ is defined as $\boldsymbol{\omega}= (\omega_x, \omega_y, \omega_z) = (\omega\sin\theta\cos\phi, \omega\sin\theta\sin\phi, \omega\cos\theta)$, thereby introducing the two tilting angles θ and ϕ, as shown in Fig. 1.7. Observed band structures which relate to the different cranking models are shown in Fig. 1.8 and can be understood as follows.

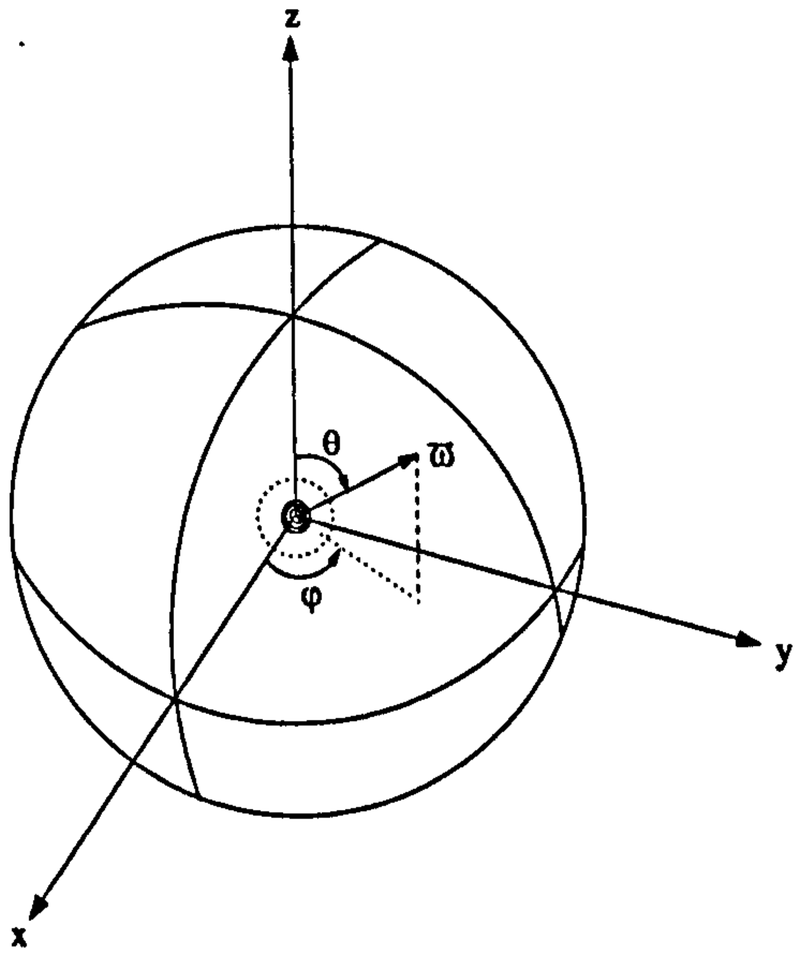

Figure 1.7: An illustration of how the direction of the cranking axis is defined by the tilting angles θ and ϕ in the general case of three-dimensional cranking (3-D TAC).

(a). The principal axis cranking model, where the angular momentum vector lies along a single principal axis. For this model K will therefore be zero, or almost zero, and hence large signature splitting will be observed.

(b). The 2-dimensional tilted-axis cranking model where the spin axis lies in a plane defined by two of the three principal axes. This model is used to describe high K, $\Delta I = 1$ bands, with little or no signature splitting, in prolate nuclei.

(c). The 3-dimensional tilted axis cranking model where the spin axis is now positioned in a quadrant defined by the three principal axes. This scenario is used, for example, to model twin $\Delta I = 1$ bands observed in triaxial odd-odd nuclei which are associated with the breaking of chiral symmetry.

1.9.3 The backbending phenomenon

An anomaly is observed in the region between 10 and 20 units of angular momentum in the yrast band, where two bands are seen with differing moments of inertia, corresponding to two parabolas in an E versus I plot as illustrated in Fig. 1.9(a). With increasing rotational frequency, the excitation energy of the excited band (S-Band) is reduced, with respect to the

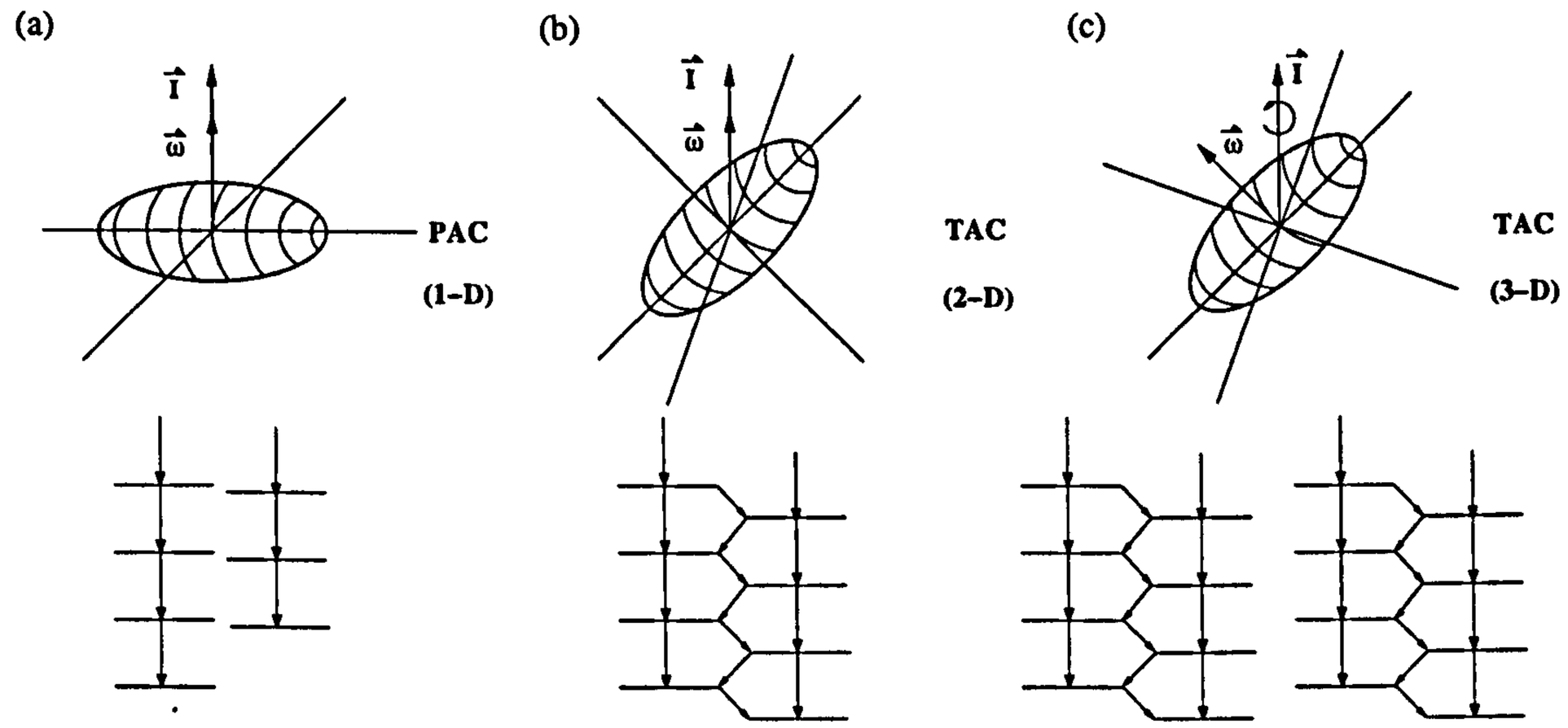

Figure 1.8: An illustration of the 1-D, 2-D and 3-D cranking. Also shown below are the types of rotational band associated with the cranking solution sketched.

ground state band (GSB), until at a particular critical frequency I_c, the S-Band becomes favoured. This phenomenon is known as *band-crossing* and is an effect of the Coriolis force acting upon two nucleons in the ground state configuration in time-reversed orbits. The Coriolis force will act in opposite directions for each nucleon in the pair and will increase as the rotational frequency increases. At the critical frequency the Coriolis force is large enough to overcome the pairing interaction and the nucleon pair is broken. Each nucleon is then able to align its intrinsic angular momentum with the rotational axis, a process known as *alignment*. The alignment of intrinsic angular momenta of the broken pair increases the total angular momentum of the nucleus and hence lowers the rotational frequency without a loss of spin. The plot of moment of inertia versus frequency shown in Fig. 1.9(b) displays the behaviour depending on the strength of the interaction. A weak interaction occurs over only a couple of states and produces the *backbend* shown by the dashed lines, however, a strong interaction occurs over more states and so the plot of $\mathcal{J}$ versus ω yields the *upbend* shown by the solid line.

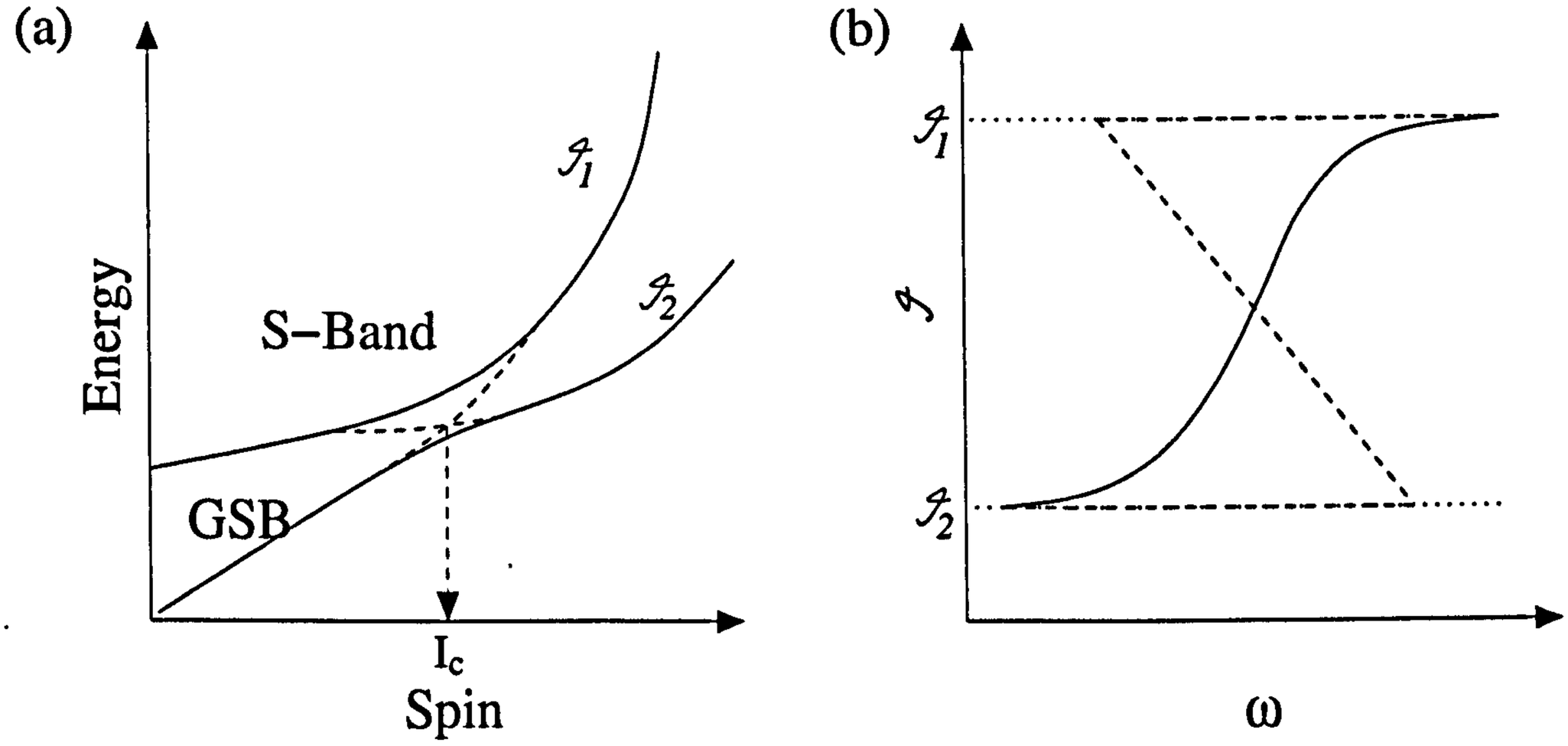

Figure 1.9: Schematic representation of two intersecting bands with different moments of inertia and the corresponding backbending plot.

1.9.4 Experimental alignments

Theoretical cranking approaches are able to predict the rotational frequencies at which particular alignments occur. However, the results of such calculations cannot be compared directly with experimental data, which provide energies rather than Routhians. Therefore, in order to make experimental measurements comparable to cranking calculations, the data need to be transformed into the intrinsic rotating frame.

The discussions of Section 1.5 have shown that the energy of rotational states follows an $I(I+1)$ law at low spin. However, at higher spin deviations from this relationship occur. In order to encompass such deviations the following parameterisation is used,

$$E(I) = A \cdot I \cdot (I+1) + B \cdot (I(I+1))^2 + C \cdot (I(I+1))^3 + ..., \tag{1.40}$$

where A is denoted by $\hbar/2\mathcal{J}$ and B, C... are higher order parameters that contain inertial terms. Alternatively, the expansion can be given in terms of the *angular frequency* ω. In principle ω is not a measurable quantity but can be defined semi-classically as follows:

$$\omega = \frac{dE}{dI}, \tag{1.41}$$

whereby, replacing the differential quotient by a quotient of finite differences, an experimental value for the angular velocity can be obtained. The experimental Routhian is given by,

$$E^{\omega}_{expt}(I) = \frac{1}{2}[E(I+1) + E(I-1)] - \omega(I)I_x(I), \tag{1.42}$$

and the subsequent subtraction of the reference energy that represents the collective rotation of the nucleus, produces a solely quasiparticle Routhian:

$$e'(I) = E^{\omega}_{expt}(I) - E^{\omega}_{ref}(I). \tag{1.43}$$

The only contributions to this quasiparticle Routhian arise from the rotation of the valence quasiparticles. The reference energy, $E^{\omega}_{ref}(I)$, can be obtained from the ground state band of an even-even nucleus which contains a zero-quasiparticle configuration. At low spin, the nuclear moment of inertia is seen to be roughly proportional to the square of the rotational frequency. An approach which is widely used for the classification of rotational nuclei is that of the *Variable moment of inertia* (VMI) model upon which the energy reference is based. One notable feature of this approach is the Harris parameterisation [Har65]:

$$\mathcal{J}^{(1)}_{ref} = \mathcal{J}_0 + \mathcal{J}_1\omega^2. \tag{1.44}$$

The Harris parameters $\mathcal{J}_0$ and $\mathcal{J}_1$ can be obtained by fitting the expression,

$$I_{x,ref}(\omega) = \omega[\mathcal{J}_0 + \mathcal{J}_1\omega^2] + i_x \tag{1.45}$$

to the reference band, where i_x is the experimental alignment, given by,

$$i_x(I) = I_x(I) - I_{x,ref}(I), \tag{1.46}$$

and the reference energy is,

$$E^{\omega}_{ref} = -\hbar\int I_{ref}d\omega = -\frac{1}{2}\omega^2\mathcal{J}_0 - \frac{1}{4}\omega^4\mathcal{J}_1 + \frac{1}{8}\frac{\hbar^2}{\mathcal{J}_0}. \tag{1.47}$$

The relative quantities, e' and i_x, can be directly compared to the calculated Routhians and alignments of the Cranking model, which are usually represented in the form of a quasiparticle diagram where the single-particle Routhian is plotted against the frequency, ω.

1.10 Symmetries of the Rotating Nucleus

The symmetry properties of a system described by H_ω depend upon the symmetries determined by the single-particle Hamiltonian H. The intrinsic wavefunctions of reflection-symmetric systems are invariant with respect to space inversion, which is denoted by the operator $\mathcal{P}$. This defines parity, π, as a good quantum number, where the total parity of a multiquasiparticle configuration is given by,

$$\pi_{tot} = \prod_i \pi_i. \tag{1.48}$$

Degrees of freedom are reduced further as the intrinsic full cranking Hamiltonian is invariant with respect to a rotation by 180° (π radians), denoted by the operator $\mathcal{R}_x$, as in the case of prolate nuclei for example. The rotational invariance is represented by:

$$\mathcal{R}_x \psi_i = \exp(-i\pi I_x)\psi_i. \tag{1.49}$$

The eigenvalues of $\mathcal{R}_x$ are $\exp(-i\pi\alpha)$, where α is known as the signature exponent quantum number. The signature quantum number is defined as $r = \exp(-i\pi\alpha)$ and the intrinsic orbitals are classified by the values $\alpha_i = +\frac{1}{2}$ ($r_i = -i$) or $\alpha_i = -\frac{1}{2}$ ($r_i = +i$), leading to the total signature α_{tot} of a multiquasiparticle configuration,:

$$\alpha_{tot} = \sum_i \alpha_i, \tag{1.50}$$

and

$$r_{tot} = \prod_i r_i. \tag{1.51}$$

A rotation of the system by an angle 2π is equivalent to the square of the operator $\mathcal{R}_x$,

$$(\mathcal{R}_x)^2 = (-1)^A, \tag{1.52}$$

and therefore for even-A nuclei the wavefunction remains unchanged but for odd-A the result is a change in sign. This leads to the following connections between the total signature α_{tot} and the total angular momentum I.

For systems with an even number of nucleons

$$\begin{aligned} &\alpha_{tot} = 0 \ (r_{tot} = +1), \quad I = 0, 2, 4, ..., \\ &\alpha_{tot} = 1 \ (r_{tot} = -1), \quad I = 1, 3, 5, ..., \end{aligned} \tag{1.53}$$

for systems with an odd number of nucleons

$$\alpha_{tot} = +\tfrac{1}{2}\ (r_{tot} = -i), \quad I = \tfrac{1}{2}, \tfrac{5}{2}, \tfrac{9}{2}, ...,$$
$$\alpha_{tot} = -\tfrac{1}{2}\ (r_{tot} = +i), \quad I = \tfrac{3}{2}, \tfrac{7}{2}, \tfrac{11}{2}, ... \tag{1.54}$$

The parameters π and α are often used to label cranking Routhians within a rotating nucleus.

1.11 Signature Splitting

The signature quantum number labels two alternate sets of allowed rotational states. These two sets differ in spin by $1\hbar$ and are themselves comprised of $\Delta I = 2$ sequences of states, this much has been established from the preceding section. As all these states possess the same intrinsic wavefunction, in the absence of any signature-dependent mixing effects, they form a single rotational sequence with both signatures connected by strong $\Delta I = 1$ transitions. However, the term relating to the Coriolis force within the cranking model actuates the splitting of this sequence into opposite signature components, which are then experimentally identified as two distinct rotational sequences, known as *signature partners.* The energy difference between these two signatures, especially within an odd-odd nucleus, is an important characteristics of the band and is a key indicator of the underlying structure. The origin of the splitting is the admixture of $\Omega = 1/2$ components of a high-j shell in the total wavefunction. Therefore the splitting is particularly large in bands described by a small K value which are built on quasiparticles in high j orbitals, as shown in Fig. 1.8(a). With increasing K, the signature splitting tends to zero and the rotational band resorts back to a single $\Delta I = 1$ sequence with strong dipole transitions, as illustrated in Fig. 1.8(b). The splitting between the two signatures is experimentally defined as the difference in excitation energy at a given rotational frequency. A useful parameter to quantify this splitting is the staggering parameter:

$$S(I) = E(I) - E(I-1) - \frac{1}{2}[(E(I+1) - E(I)) + (E(I-1) - E(I-2))]. \tag{1.55}$$

1.11.1 Signature Inversion

Another signature effect which is more sensitive to the underlying nuclear structure is the inversion of signature splitting in a rotational band. Whenever two signature partners are

split, one sequence becomes energetically favoured while the other becomes unfavoured, effectively the former becomes more "yrast" than the latter. Which signature becomes favoured depends upon the single particle configuration upon which the band is built. For a particle in a j orbital, the favoured signature can be found from,

$$\alpha_f = j \mathrm{mod} 2. \tag{1.56}$$

Similarly, for a doubly-odd nucleus with a specific $j_\pi \otimes j_\nu$ configuration, the favoured signature is:

$$\alpha_f = [j_\pi + j_\nu] \mathrm{mod} 2. \tag{1.57}$$

As an example, the lowest energy $\pi h_{11/2} \otimes \nu h_{11/2}$ configuration should have:

$$\alpha_f = [11/2 + 11/2] \mathrm{mod} 2 = 1, \tag{1.58}$$

and therefore levels with odd spin (α_f) are favoured over levels with even spin (α_u). Bands are said to exhibit signature inversion when the situation is reversed and the 'favoured' signature is shifted higher in energy than the 'unfavoured' signature. This reversed situation is typically encountered at low spin, with a further inversion of the signatures occurring at a critical spin value I_c to restore the conventional arrangement.

Signature inversion is a phenomenon which is apparent in certain bands of odd-odd nuclei in many regions of the nuclear chart [Rie01] [Cha02] [Zhe01] [Liu96] [Tim02]. It has been predicted to be a fingerprint of triaxiality [Ben84], and a possible link to chirality [Rie01] has also being proposed. Semmes and Ragnarsson [Sem90] suggested that the proton-neutron interaction was a possible source of signature inversion, and recently Satula, Wyss and Xu [Xu00] have tried to explain this phenomenon with quadrupole pairing, stating that this can lead to signature inversion even in axially symmetric nuclei.

1.12 Electromagnetic Transitions

The atomic nucleus contains charged particles in the form of protons. If the nucleus were a static system whose charged components were not moving in different orbits, it would therefore possess a static electromagnetic field; the charge distribution could then be described in terms of a multipole expansion. However, the nucleus is a more complex system

of moving charges and currents which give rise instead to a radiation field. The transitions which occur between excited states of the nucleus are governed by its electromagnetic properties, and are associated with the emission of photons, the quanta of electromagnetic radiation. In the energy range of pertinence to nuclear structure, such photons come in the form of gamma rays which are associated with a multipole moment of a charge distribution such as a dipole, a quadrupole or an octupole. The probability of gamma-ray emission of a particular multipolarity depends upon the structure of the excited states, namely the initial and final angular momentum (I_i, I_f), and the parity (π_i, π_f) of the states involved. Gamma rays have an intrinsic spin of $1\hbar$ with negative parity and must conserve angular momentum, such that:

$$|I_i - I_f| \leq \lambda \leq I_i + I_f, \tag{1.59}$$

where λ is the angular momentum carried by the gamma ray. A $0^+ \rightarrow 0^+$ transition is subsequently forbidden via gamma-ray emission (such a transition may still proceed however by conversion electron decay, a mechanism of little relevance to the present study). This determines for example that a transition from a state with spin $2\hbar$ to a state with spin $0\hbar$, i.e $\Delta I = 2$, must have $\lambda = 2$, whereas a transition from a state with spin $3\hbar$ to a state with spin $2\hbar$, i.e $\Delta I = 1$, can possess $\lambda = 1, 2, 3, 4$ or 5. The gamma-ray is said to *stretched* if it carries the difference between the angular momentum of the initial and final states. Along with its multipolarity, λ, the radiation is also characterised by its electromagnetic nature σ, where E is used to denote electric transitions and M is used to denote magnetic transitions. The following conditions of parity apply:

$$\pi = \begin{cases} (-1)^{\lambda} & E\lambda \\ (-1)^{\lambda+1} & M\lambda \end{cases} \tag{1.60}$$

Therefore, a transition from $I^{\pi} = 3^+$ to $I^{\pi} = 2^-$ may proceed by $E1$, $M2$, $E3$, $M4$ or $E5$ radiation, all with competing probabilities and transition rates.

The mean lifetime τ and the partial width Γ_γ of the initial state can be related to the total transition probability $T(\sigma\lambda; I_i \rightarrow I_f)$ by,

$$T(\sigma\lambda; I_i \rightarrow I_f) = G_\lambda B(\sigma\lambda; I_i \rightarrow I_f) = \frac{1}{\tau} = \frac{\Gamma_\gamma}{\hbar}, \tag{1.61}$$

where the first term, G_λ can be regarded as a phase factor that is dependent on both the multipolarity of the transition and the energy of the gamma-ray. The second term,

$B(\sigma\lambda)$ is known as the reduced transition probability and contains all the nuclear structure information,

$$B(\sigma\lambda; I_i \rightarrow I_f) = \sum_{\mu,m_f} |\langle I_f m_f | \mathcal{M}(\sigma\lambda,\mu) | I_i m_i \rangle|^2, \tag{1.62}$$

where $m_f - m_i = \mu$ and $\mu = \lambda, \lambda-1, ..., -\lambda$. The moment associated with electric and magnetic multipoles is denoted by $\mathcal{M}(\sigma\lambda,\mu)$. The reduced transition probability can also be described using the reduced matrix elements $Q(\sigma\lambda)$,

$$B(\sigma\lambda) = \frac{1}{2I_i+1} |\langle I_f || Q(\sigma\lambda) || I_i \rangle|^2, \tag{1.63}$$

where the reduced matrix elements are often described in terms of *Weisskopf units*, which are estimates of transition strengths for a single proton from an initial orbital state to a final state of zero angular momentum. If a measured transition probability is much greater than the predicted Weisskopf estimate then the nuclear structure is said to be favourable for such a transition. This indicates similar wavefunctions for the initial and final states and a possible collective motion involving many nucleons. The Weisskopf estimates, when compared with experimental transition rates, are also a useful guide for the assignment of transitions with unknown multipolarity.

The transition probability for an electric transition is typically two orders of magnitude larger than that for a magnetic transition of the same multipolarity. Additionally, the probability is inversely proportional to the transition multipolarity. Therefore, an $E2$ transition may compete with an $M1$ transition but an $E1$ transition will dominate over an $M2$ transition where both are allowed. Competing transitions with $\lambda > 2$ can generally be neglected.

Measuring the lifetime of a transition is often difficult. However, $B(M1)/B(E2)$ ratios, which can be measured from the experimental branching ratios for competing $\Delta I = 1$ and $\Delta I = 2$ transitions, can be directly compared with Weisskopf estimates. The $B(M1)/B(E2)$ ratios are related to the measured transition probabilities by,

$$\frac{B(M1; I \rightarrow I-1)}{B(E2; I \rightarrow I-2)} = 0.697 \frac{[E_\gamma(I \rightarrow I-2)]^5}{[E_\gamma(I \rightarrow I-1)]^3} \times \frac{1}{\lambda} \frac{1}{[1+\delta^2]} \left[\frac{\mu_N^2}{e^2 b^2}\right], \tag{1.64}$$

where $\lambda = T_\gamma(I \rightarrow I-2)/T_\gamma(I \rightarrow I-1)$ and E_γ is measured in MeV. The multipole mixing ratio, δ, can be expressed in terms of the reduced matrix elements, which for $\Delta I = 1$

transitions yields,

$$\delta_{E2/M1} = 0.835 E_\gamma \frac{\langle I||E2||I-1\rangle}{\langle I||M1||I-1\rangle}, \tag{1.65}$$

for E_γ in MeV, or can be simply related to the $\Delta I = 1$ transition probabilities, giving:

$$\delta^2_{E2/M1} = \frac{T(E2; I \rightarrow I-1)}{T(M1; I \rightarrow I-1)}. \tag{1.66}$$

The multipole mixing ratios can also used to determine the ratio of $\Delta I = 1$ to $\Delta I = 2$ reduced $E2$ transition probabilities depopulating a state, such that:

$$\frac{B(E2; I \rightarrow I-1)}{B(E2; I \rightarrow I-2)} = \left[\frac{E_\gamma(I \rightarrow I-2)}{E_\gamma(I \rightarrow I-1)}\right]^5 \times \frac{1}{\lambda}\frac{\delta^2}{[1+\delta^2]}. \tag{1.67}$$

1.12.1 Theoretical electromagnetic transition strengths

Experimental transition strengths can be compared to theoretical estimates within the framework of the rotational model for odd-odd nuclei. The following expressions [Boh75],

$$\begin{aligned} B(M1; I \rightarrow I-1) &= \frac{3}{4\pi}\mu_N^2 G_{KK}^2 |\langle IK10|I-1K\rangle|^2 \\ B(E2; I \rightarrow I-2) &= \frac{5}{16\pi} e^2 Q_0^2 |\langle IK20|I-2K\rangle|^2, \end{aligned} \tag{1.68}$$

can be combined to yield a theoretical ratio,

$$\frac{B(M1; I \rightarrow I-1)}{B(E2; I \rightarrow I-2)} = \frac{8}{5}\frac{G_{KK}^2}{Q_0^2}\frac{(2I-1)}{(I-1+K)} \times \frac{(I-1)}{(I-1-K)}\left[\frac{\mu_N^2}{e^2 b^2}\right], \tag{1.69}$$

where Q_0 is the quadrupole moment and the parameter G_{KK} is defined as:

$$\begin{aligned} G_{KK} &= K(g_K - g_R) \\ &= \Omega_p(g_{\Omega_p} - g_R) + \Omega_n(g_{\Omega_n} - g_R), \end{aligned} \tag{1.70}$$

where g_K is the effective g-factor of the related two-quasiparticle configuration, g_R is the rotational g-factor, and g_{Ω_p} and g_{Ω_n} are the single-particle g-factors for protons and neutrons, respectively.

Chapter 2

Gamma-ray spectroscopy and analytical methods

Gamma-ray spectroscopy is a popular and widespread experimental technique employed to study the allowed quantum states through which a nucleus may be excited. The structure of these states can reveal much about the nucleus in question and, ultimately, the nature of the internucleon forces which govern its behaviour. Within this chapter a general overview of the methods used in high-spin gamma-ray spectroscopy will be given. A more detailed description of the specific equipment used for the present study will be presented in the following chapter.

2.1 Heavy-ion Fusion Evaporation Reaction

The fusion evaporation reaction [Mor63] has become a common mechanism with which to populate high-spin states in atomic nuclei. The process is here considered in two steps, (i) the formation of the compound nucleus, and (ii) the compound nuclear decay.

In the first stage a compound nucleus is formed from the fusion of an energetic projectile ion and a target nucleus. The success of compound nucleus formation is reliant on the projectile overcoming the Coulomb repulsion between itself and the target nucleus, as given:

$$E_{\text{Coulomb}}(MeV) = \frac{1.44 Z_p Z_t}{1.16(A_p^{1/3} + A_t^{1/3} + 2)}, \tag{2.1}$$

where the subscripts p and t refer to the projectile and target respectively. The reaction

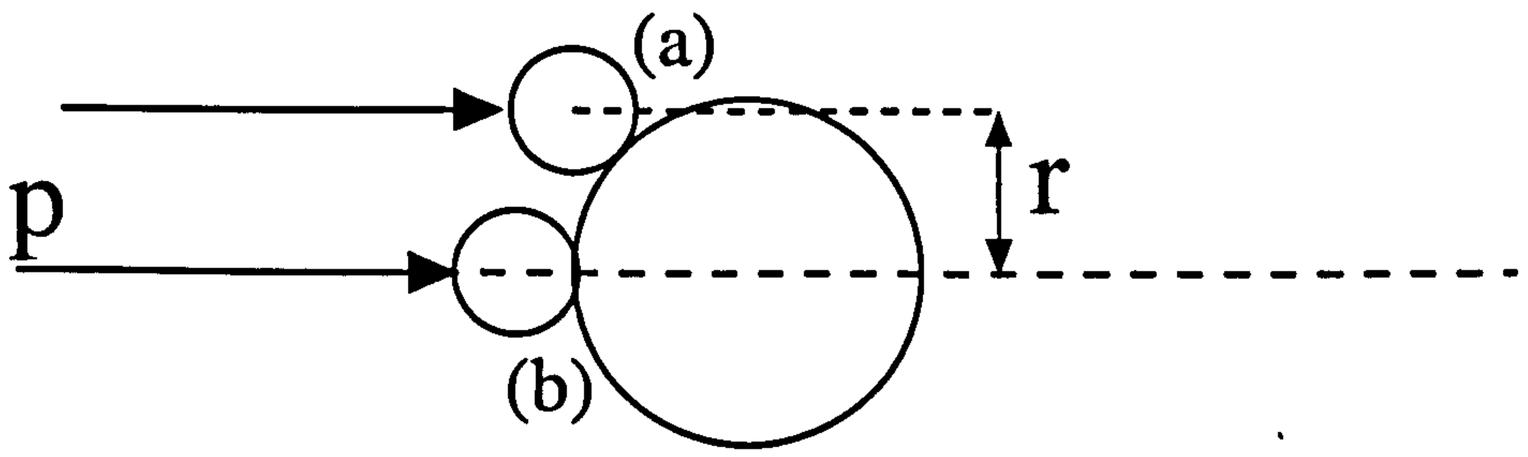

Figure 2.1: Schematic representation of the fusion-evaporation reaction. (a) shows a peripheral interaction between the projectile and target nucleus and (b) shows the projectile hitting the target head on, giving no angular momentum to the compound nucleus.

also imparts angular momentum to the compound nucleus given by:

$$\mathbf{l} = \mathbf{r} \times \mathbf{p}, \tag{2.2}$$

where **r** is the impact parameter and **p** is the linear momentum of the beam as shown schematically in Fig. 2.1. The most peripheral collisions, providing a compound nucleus is successfully formed in the process, correspond to largest **r** and will lead to compound nuclei with the most angular momentum, that is, such nuclei are populated in the highest-spin states. Additionally, heavier projectiles have larger **p** and are therefore typically used to study high-spin structure.

The second stage of the fusion-evaporation reaction can itself be divided into two stages, (i) particle evaporation, and (ii) subsequent gamma-ray emission from the residual nucleus. The use of stable (or long-lived) beams and targets leads to the formation of compound nuclei from which particle emission subsequently occurs. Initial particle evaporation occurs within 10^{-15} s of compound nucleus formation, with each successive emitted particle reducing the excitation energy by approximately 8 MeV. The excitation energy is therefore reduced until it lies below the particle separation energy relative to the yrast line, at which point particle emission is no longer allowed. The highly excited *residual* nucleus then de-excites by the emission of a cascade of gamma radiation. Initially these transitions are of dipole character and may remove much energy (several MeV) but only a few units of angular momentum. Such gamma rays, whose energies form a continuum due to the large density of states in the excited system, are referred to as *statistical*. These statistical gamma ray

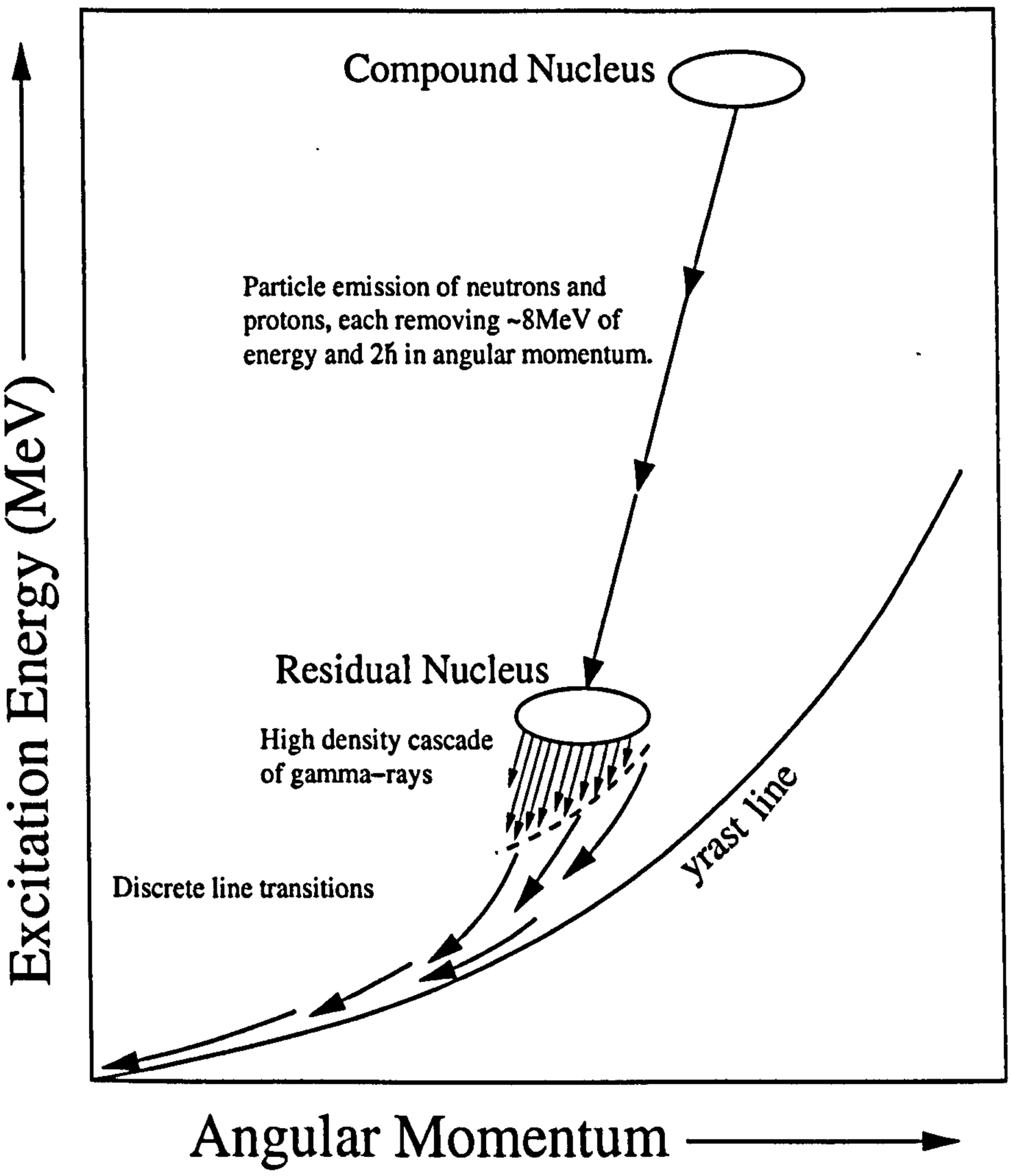

Figure 2.2: Schematic representation of the de-excitation of a compound nucleus.

cascades approach the yrast line as illustrated in Fig. 2.2, the yrast line being the locus of points which describe the lowest allowed excitation energy at a given angular momentum. After 10^{-12} s the excitation energy has reduced significantly as has the density of excited states. Subsequent gamma-ray emission therefore typically involves discrete transitions with energies of typically less than 1.5 MeV. These discrete transitions, which are quadrupole in character, form cascades of gamma rays which eventually leave the residual nucleus in its ground state.

2.2 Interactions of gamma rays with matter

Gamma rays interact within matter through either a partial or complete transfer of gamma-ray energy to electron kinetic energy. The three major processes by which gamma rays interact are: (i) the photoelectric effect, (ii) Compton scattering and (iii) pair production. These gamma-ray interaction mechanisms are described below and are shown schematically in Fig. 2.3.

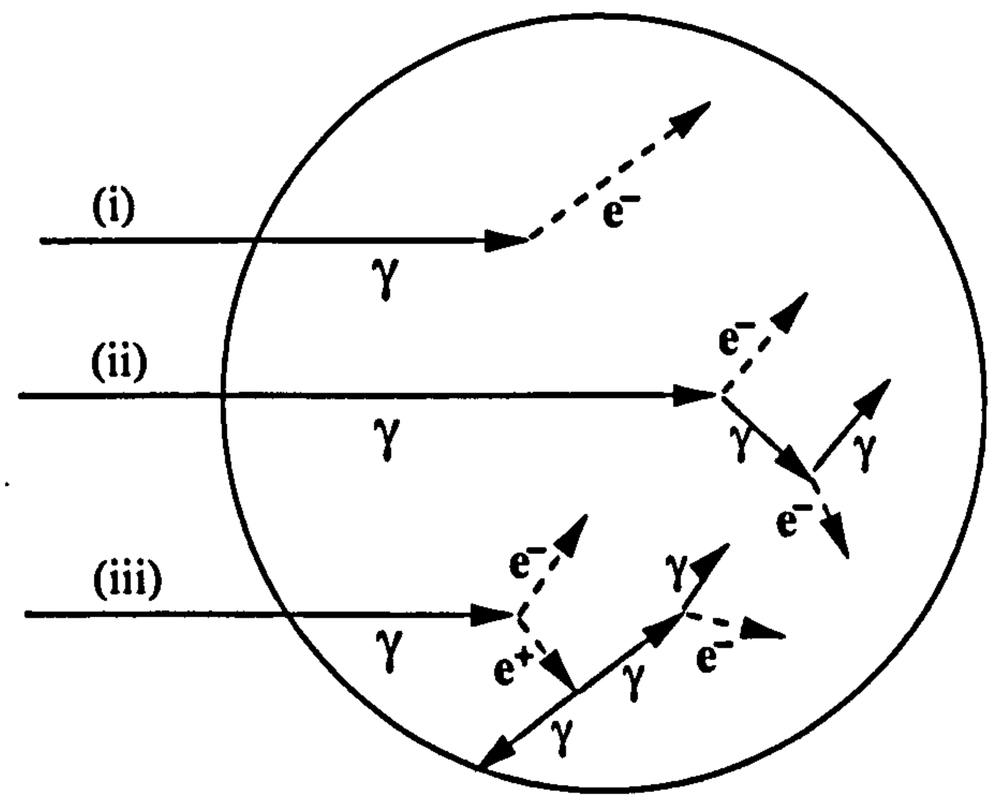

Figure 2.3: Schematic illustration of the main interactions of a gamma ray within a detector. (i) shows the photoelectric effect, (ii) the Compton scattering interaction and (iii) the pair production interaction.

- During photoelectric absorption, an incoming gamma ray is completely absorbed by an atomic electron. This *photoelectron* is ejected from the atom with an energy equal to that of the initial gamma ray E_γ, minus the binding energy E_b of the atomic electron, as given by,

$$E_e = E_\gamma - E_b. \tag{2.3}$$

The interaction leaves a vacancy within one of the bound shells which is filled through either the capture of a free electron from the medium or from a rearrangement of electrons in the surrounding shells. This generates one or more characteristic X-ray photons. Photoelectric absorption is the dominant interaction at low energies (< 250 keV). The relationship between the atomic number of the absorbing material and

the probability of absorption, τ, is given by Eq. 2.4, where n varies between 4 and 5 for the gamma-ray energies of interest,

$$\tau \approx constant \times \frac{Z^n}{E_\gamma^{3.5}}. \tag{2.4}$$

- Compton scattering involves an interaction between a gamma-ray photon and a weakly-bound atomic electron. The gamma ray transfers a fraction of its energy and is deflected through an angle θ from its original path. The energy transferred to the recoil electron is:

$$E_e = E_\gamma \left\{ 1 - \frac{1}{1 + E_\gamma[1 - \cos\theta]/mc^2} \right\}. \tag{2.5}$$

This interaction dominates at energies between approximately 0.25 and 8 MeV. The Compton scattering cross section depends purely upon the number of electrons available as scattering targets and therefore has a linear dependence on the atomic number of the absorber material.

- Pair production consists of the conversion of a gamma-ray photon into an electron-positron pair within the Coulomb field of the nucleus. This process is only possible if the incident gamma-ray energy exceeds the combined rest mass energy of the electron-positron pair (1022 keV). The kinetic energy of the electron E_e and positron E_p is therefore given by:

$$E_e = E_p = \frac{E_\gamma - 1022\text{keV}}{2}. \tag{2.6}$$

The ejected positron subsequently annihilates with a free electron, releasing two 511 keV gamma rays. An approximate relationship holds between the square of the absorber atomic number and the probability of pair production per nucleus.

2.3 Germanium detectors

For the detection of gamma radiation two major detector types are typically used: inorganic scintillator detectors and germanium semiconductor detectors. The former possess a high detection efficiency while the latter provide better energy resolution. As high-spin discrete gamma-ray spectroscopy requires the separation of closely-spaced gamma-ray energies, germanium detectors are used for this application. The operation of a germanium semiconductor can best be understood by first considering the electronic band structure

of the material. A semiconductor possesses a band structure intermediate between that of an insulator and that of a conductor. Here the band gap between the *valence* (electrons are bound to specific lattice sites within the crystal) and *conduction* (electrons are free to migrate through the crystal) bands is sufficiently large to require the introduction of some thermal energy to excite electrons from occupied valence bands into energy levels above the conduction band base. In the case of an insulator this band gap is of the order of 5 eV or more, whereas for the semiconductor this is reduced to approximately 1 eV, allowing an increased migration of electrons into the conduction band. The electronic properties of the semiconductor material can be influenced by the addition of small amounts of impurities, creating n-type (donor) and p-type (acceptor) materials. A *depletion region* can then be constructed by bringing the two types of material together to form a junction in good thermodynamic contact, the *p-n junction* [Kno89]. The n-type region will have a higher density of electrons than the p-type region and so a diffusion of electrons from the high concentration to the lower concentration will take place. A build up of negative charge on the p-type side is produced with a corresponding opposite positive net charge on the n-type side of the junction. An equilibrium is achieved when the field is just adequate to prevent further diffusion across the junction and a steady state of charge distribution is created. Any electron-hole pairs then generated within this depletion region by the passage of radiation will be swept out by the electric field, acting like a high-sensitivity parallel-plate ionisation chamber, and the motion will constitute a basic electrical signal. The application of a reversed bias across this junction will result in an enhancement of the potential difference, increasing the width of the depletion region, and subsequently increasing the efficiency of radiation detection. Germanium detectors are produced to a very high purity, where refining techniques are now capable of reducing the impurity concentration to approximately 10^{10} atoms/cm^3. As described by Eq. 2.7, a decrease in the net impurity concentration N, yields an increase in the depletion region of the crystal:

$$d = \left(\frac{2\epsilon V}{eN}\right)^{1/2}, \tag{2.7}$$

where d is the depletion region thickness, ϵ is the ionisation energy and V is the reversed bias. An increase in depletion region improves the energy resolution of the detector.

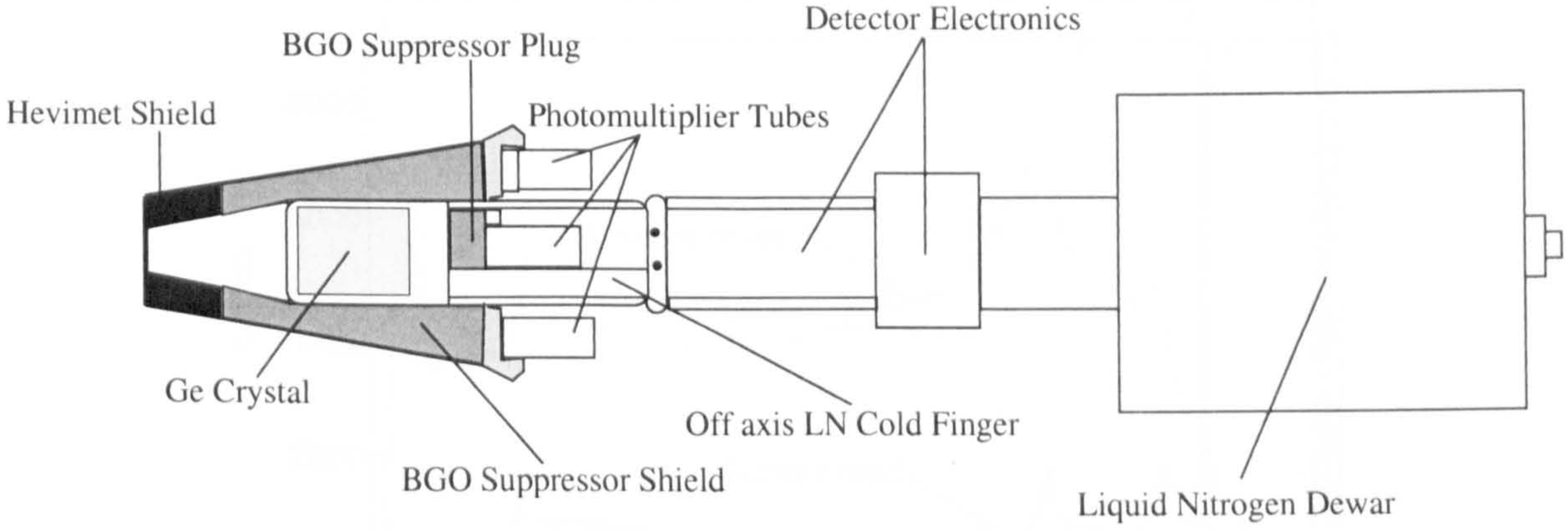

Figure 2.4: Schematic of a high purity germanium detector with BGO Compton suppression shields and cooling apparatus.

2.4 Compton suppression

Due to limited detector size, a significant number of incident γ-rays will not be fully absorbed and will be scattered out of the detector material after one or more interactions. The result of this scattering is the *Compton continuum* and leads to a reduced *peak-to-total ratio* in a histogram of measured gamma-ray energies. The peak-to-total ratio r is defined as:

$$r = \frac{\epsilon_{\text{peak}}}{\epsilon_{\text{total}}}, \tag{2.8}$$

where ϵ_{peak} and ϵ_{total} are the efficiencies of the peak and total spectrum, respectively. To identify Compton events, a shield can be placed around the detector, as shown in the schematic diagram Fig. 2.4. Any gamma ray scattering out of the detector can then be detected in the surrounding shield, consequently identified as a Compton-scattered photon, and rejected. Such a suppression shield should ideally be composed of a material with a high efficiency for absorbing gamma-ray photons. In practice this criterion is fulfilled by an inorganic scintillator, bismuth germanate (BGO). BGO has a high density, Bi having an atomic number of 83, which has an extremely good detection efficiency when compared with other materials. The addition of a BGO shield around a Ge detector yields a significant reduction of the Compton background observed in a gamma-ray energy spectrum. This is evident in Fig. 2.5 where spectra are presented which have been obtained from a Ge detector

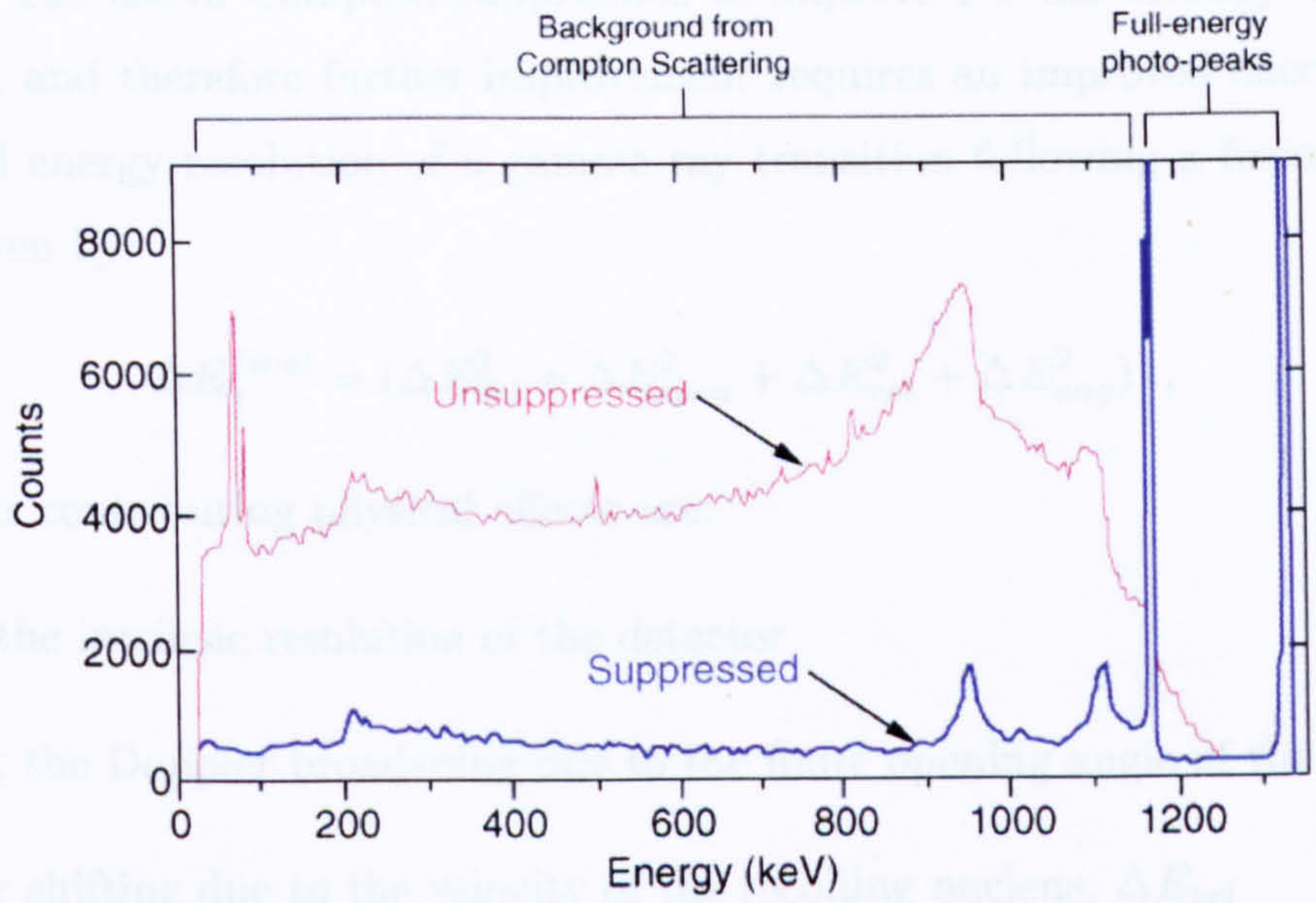

Figure 2.5: Spectra taken using a ^{60}Co source to illustrate the improvement possible in the peak-to-total ratio with the introduction of suppression shields surrounding the detector.

both with and without the aid of a Compton suppression shield.

2.5 Correction of Doppler broadening

The targets used in fusion-evaporation reactions are often chosen to be very thin. The predominant reason for this is to allow the study of high-spin transitions with a minimum effect of Doppler broadening from the spread in recoil velocities emitted from the target. However, Doppler effects are still apparent and to evaluate the consequences of Doppler effects in gamma-ray spectroscopy, it is convenient to consider how effectively a gamma-ray spectrometer (either a singular detector or a group of detectors employed together) can resolve individual transitions. A measure of this quantity is provided by the *resolving power*, R, of the spectrometer. A convenient way to quantify this is:

$$R = \left(\frac{SE_\gamma}{\Delta E_\gamma^{final}} \right) PT, \tag{2.9}$$

where SE_γ is the average energy spacing of consecutive gamma-ray transitions in a cascade, ΔE_γ^{final} is the energy resolution and PT is the peak-to-total ratio. As SE_γ is reaction dependent, to increase the resolving power of a spectrometer either PT or ΔE_γ^{final} must

be improved. The use of Compton suppression to improve PT has already been discussed in section 2.4, and therefore further improvement requires an improved energy resolution. The measured energy resolution of a gamma-ray transition following a fusion evaporation reaction is given by:

$$\Delta E_{\gamma}^{final} = (\Delta E_{int}^2 + \Delta E_{open}^2 + \Delta E_{vel}^2 + \Delta E_{ang}^2)^{\frac{1}{2}}, \tag{2.10}$$

where the four contributing physical effects are:

- ΔE_{int}, the intrinsic resolution of the detector
- ΔE_{open}, the Doppler broadening due to the finite opening angle of the detector
- Doppler shifting due to the velocity of the recoiling nucleus, ΔE_{vel}
- the deflection of the recoil path due to particle emission, ΔE_{ang}.

The intrinsic resolution of the detector is optimised during manufacture and should ideally be the limiting factor in the resolution. Doppler effects arise because the gamma rays are emitted from a system which is moving with respect to the laboratory frame of reference. The measured energy in the laboratory frame, E_{γ}, is given relativistically, to first order in β, by

$$E_{\gamma} = E_0(1 + \beta\cos\theta), \tag{2.11}$$

where E_0 is the intrinsic gamma-ray energy, θ is the angle of the gamma-ray path in relation to the trajectory of the recoiling nucleus, and β is v/c where c is the speed of light and v is the velocity of the nucleus in the laboratory frame. The velocity can be calculated from the kinematics of the reaction but will contain some uncertainty as the recoiling nuclei actually form a distribution of velocities due to the finite width of the target material. This is the origin of the ΔE_{vel}^2 term in Eq. 2.10. Similarly, the gamma-ray path is inferred through an accurate knowledge of the detector position but this too possesses an uncertainty due to the finite opening angle of the detector and gives rise to the ΔE_{open}^2 term in Eq. 2.10. The uncertainty in the energy measurement ΔE_{γ}, to the uncertainty in angle $\Delta\theta$ is:

$$\begin{aligned} \Delta E_{\gamma} &= \frac{\delta E_{\gamma}}{\delta\theta}\Delta\theta \\ &= -E_0\beta\sin\theta\Delta\theta, \end{aligned} \tag{2.12}$$

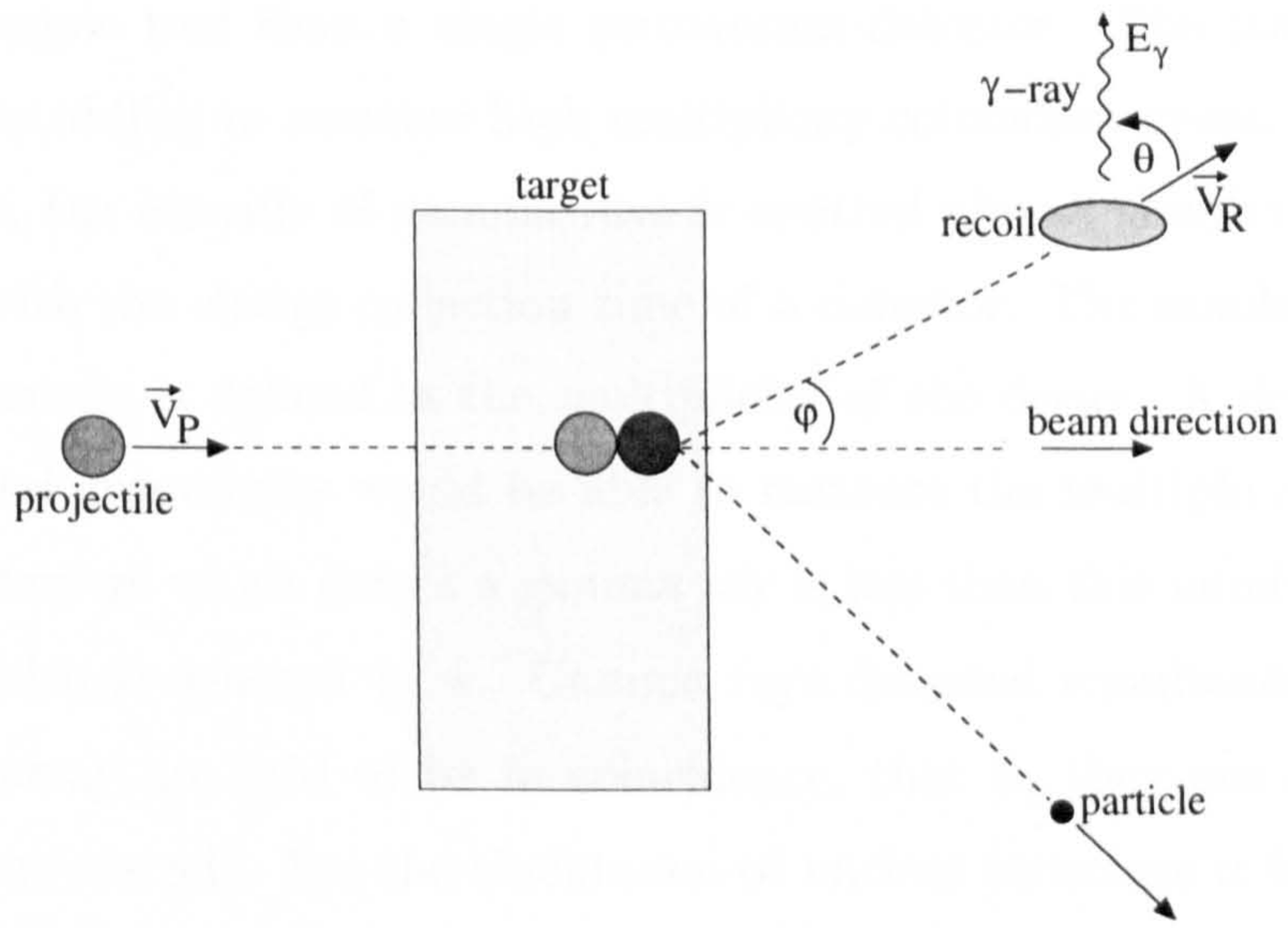

Figure 2.6: Schematic of heavy-ion induced fusion-evaporation reaction. The recoil nucleus is emitted at an angle relative to the beam direction thus introducing the kinematic recoil effect.

illustrating that a reduction in the detector opening angle $\Delta\theta$, leads to a reduction in the Doppler broadening, subsequently improving the resolution. The particle emission which follows compound nucleus formation will deflect the recoiling nucleus from the beam direction shown in Fig. 2.6. Therefore the angle θ cannot be taken solely from the detector position, as this assumes that the recoiling nucleus travels along the beam direction; instead of forming a straight line, the distribution of trajectories will form a *recoil cone*. It is this kinematic recoil effect which contributes the ΔE^2_{ang} term to Eq. 2.10. A correction can be performed to account for this effect; if the trajectories and momentum of the emitted particles are detected, the trajectory of the recoiling nucleus can be deduced from the kinematics of the system [Sew94].

2.6 Arrays of germanium detectors

In the previous section it was shown that a reduction in the opening angle of a detector leads to an improved resolution and an increased resolving power. To achieve this, detectors may either be made physically smaller or positioned further from the target position. In either case, to improve overall efficiency by maintaining a good solid angle coverage,

many detectors must be combined to form an array. An array of detectors is a far more powerful spectroscopic tool than a single germanium detector. The major advantage to such systems is the ability to measure high multiplicity coincident events [Bea96]. When a nucleus de-excites, the cascade of gamma rays is emitted almost simultaneously, certainly when compared with the charge collection time of a detector. The number of gamma rays emitted in the cascade is defined as the multiplicity of the decay. A detector array with 100% efficiency and granularity would be able to measure the multiplicity but in practice the number of detectors which detect a gamma ray is less than this number and is referred to as the fold, which is denoted by k. Gamma rays detected simultaneously by separate detectors in the array are said to be in coincidence, that is, they are assumed to originate from the same cascade. For the elucidation of nuclear structure it is advantageous to measure coincidence between gamma rays and therefore a system which can measure high fold is desirable. In addition, if the array covers a large solid angle it can also function as a calorimeter by adding the energies of all gamma rays measured in coincidence. This measurement gives the *sum-energy*, which is denoted by H. As will be shown in chapter 4, both the sum energy and fold are reaction dependent and can therefore be used to select gamma rays from a particular reaction product.

2.7 Coincidence matrices

The $\gamma - \gamma$ correlation matrix is an extremely powerful analytical technique for examining the measured coincidences between gamma rays. The procedure for the creation of a two-dimensional matrix is as follows. All the gamma rays detected simultaneously by the array of germanium detectors are assigned to the same *event*, which has an associated fold k. These coincident gamma rays are then *unfolded* into the ${}_{k}C_{n}$ n-fold coincidences which comprise all the permutations of the original event. For example, with $n = 2$, for each 2-fold coincidence γ_1-γ_2, a matrix is then incremented at points $x = \gamma_1$, $y = \gamma_2$ and $x = \gamma_2$, $y = \gamma_1$, where the latter ensures that the matrix is symmetric with respect to $x = y$. With this procedure completed for each detected event, a projection of the matrix for a chosen value of x increments a histogram of all values of y measured in coincidence with x. The versatility of this method lies in the speed at which different projections may be obtained.

Thus gamma-ray coincidences can be explored in detail and the decay scheme of the nucleus reconstructed. The principle behind the two-dimensional matrix can be extended to higher dimensions, e.g cubes ($\gamma - \gamma - \gamma$) or hypercubes ($\gamma - \gamma - \gamma - \gamma$).

Chapter 3

Experimental techniques and apparatus

A more detailed discussion of the techniques and apparatus applied to the high-spin study of ^{124}La will be described in this chapter.

3.1 Experimental Details

An experiment has been performed to populate high-spin states of ^{124}La using the fusion evaporation reaction, ^{64}Zn (^{64}Zn, 3p1n). The experiment was conducted at the Argonne National Laboratory, using a 260 MeV ^{64}Zn beam supplied by ATLAS (Argonne Tandem Linac Accelerator System) [AtlURL]. The beam was incident on a thin, isotopically enriched, self-supporting ^{64}Zn target of nominal thickness 500μg/cm^2 for a period of approximately 120 hours. The Gammasphere [Lee90] gamma-ray spectrometer [Nol94] was employed in conjunction with the Microball charged particle detector [Sar96] [Mic], the Neutron Shell of liquid scintillation detectors [Neu] and the Fragment Mass Analyser [Dav89] [Dav92]. Cross-sections have been estimated for the production of ^{124}La, and for the nuclei formed through competing evaporation channels, using the evaporation code ALICE [Bla91]. The calculated excitation function is displayed in Fig. 3.1.

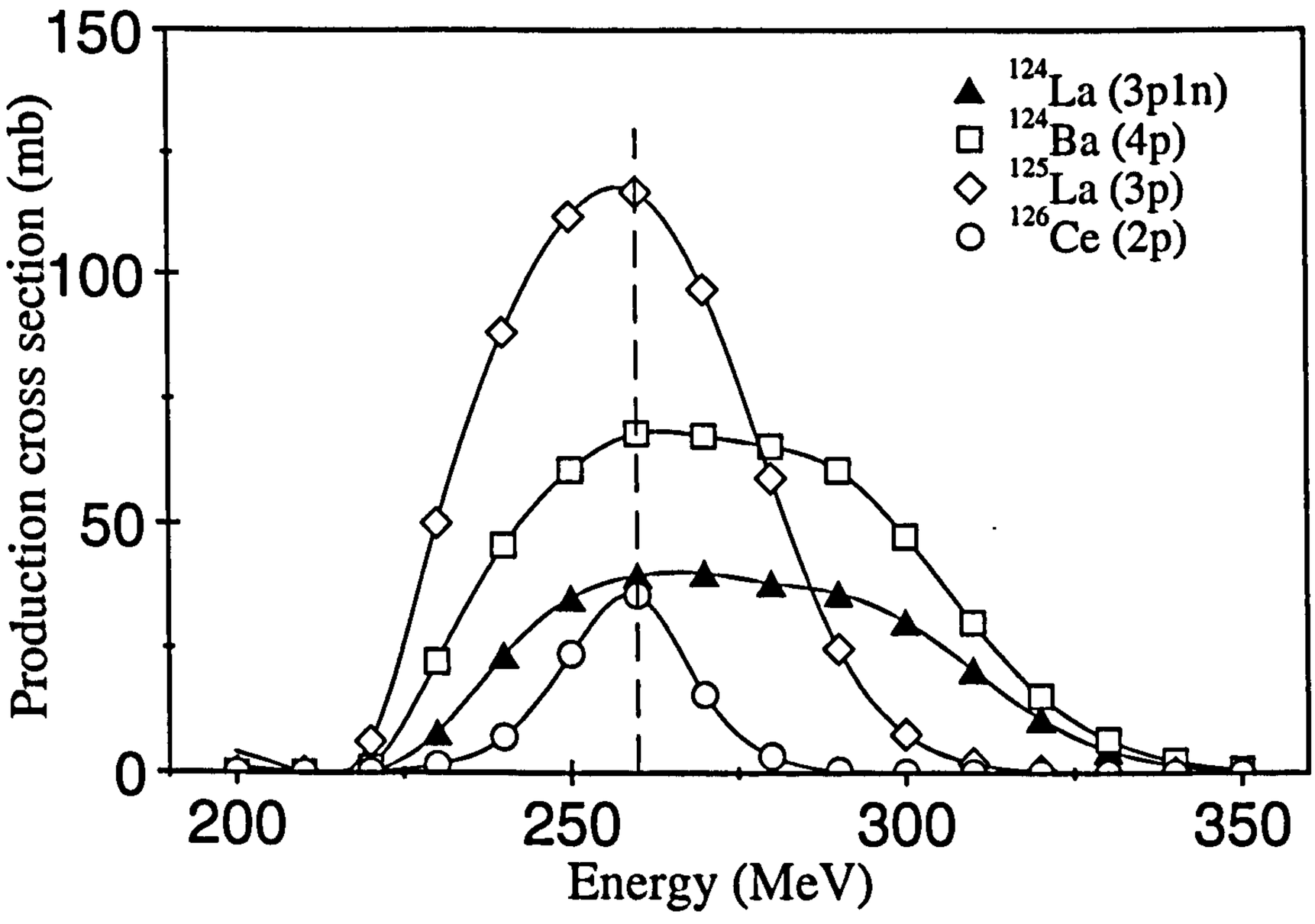

Figure 3.1: Plots of the calculated excitation functions for the ^{64}Zn+^{64}Zn reaction using ALICE code. The evaporation channels are given in brackets along with the residual nucleus that is populated. ^{125}La and ^{124}Ba can clearly be seen to be the main contaminants.

3.2 The Gammasphere Array

Gammasphere comprises a spherical arrangement of 110 closely packed n-type high-purity germanium detectors (HPGe), arranged in 17 rings around the target. For the present study only 78 of the germanium detectors were employed as the five most forward rings of detectors were replaced with the Neutron Shell. The HPGe detectors are coaxial in orientation with bulletised closed ends to allow as large an active volume as possible and tapered in geometry for better stacking into the spherical array. A reverse bias voltage of approximately 2500–3000 V is applied to each detector to completely deplete the crystal volume. Each germanium detector is surrounded by a BGO Compton-suppression shield which comprises six BGO elements situated longitudinally around the Ge crystal and one placed behind as shown in Fig. 2.4. Only the front of the Ge crystal is therefore unshielded and only backscattered photons may escape Compton suppression. In Fig. 3.2 the arrange-

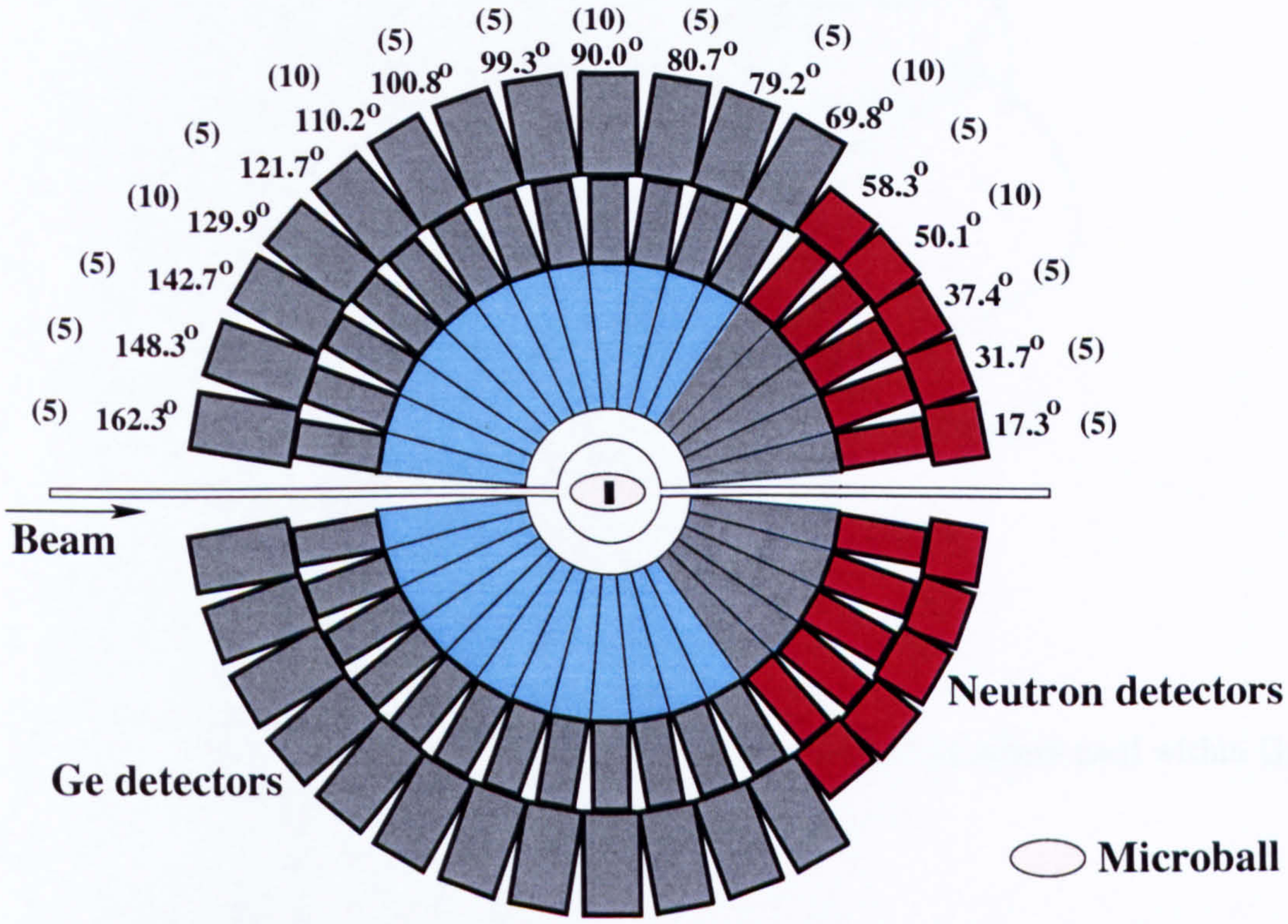

Figure 3.2: A schematic diagram of the Gammasphere array, with the forward five rings replaced by neutron detectors. The position of the Microball within Gammasphere is also shown, inside the target chamber.

ment of the array is shown along with the positions of the Microball and Neutron Shell, which will be discussed shortly. Detectors between the angles 69.8° and 129.9° were electrically segmented into two D-shaped halves as shown in Fig. 3.3. The segmentation of the Ge detector is accomplished by means of a segmented outer contact rather than a physical segmentation of the crystal. The signals which are read out by associated electronics are a high resolution (0.33–0.66 keV/channel) 'full-energy' signal from the inner contact, which represents the total energy deposited on both sides of the detector, and a low resolution (2.5 keV/channel) 'side-energy' signal from one of the segmented outer contacts, which represents the energy deposited on one side of the detector. By examining the ratio of the side channel energy to the high resolution energy, a crude position sensitivity is achieved which leads to a reduction in the effective detector opening angle. In total, the array provides a total photopeak efficiency of approximately 7.5%.

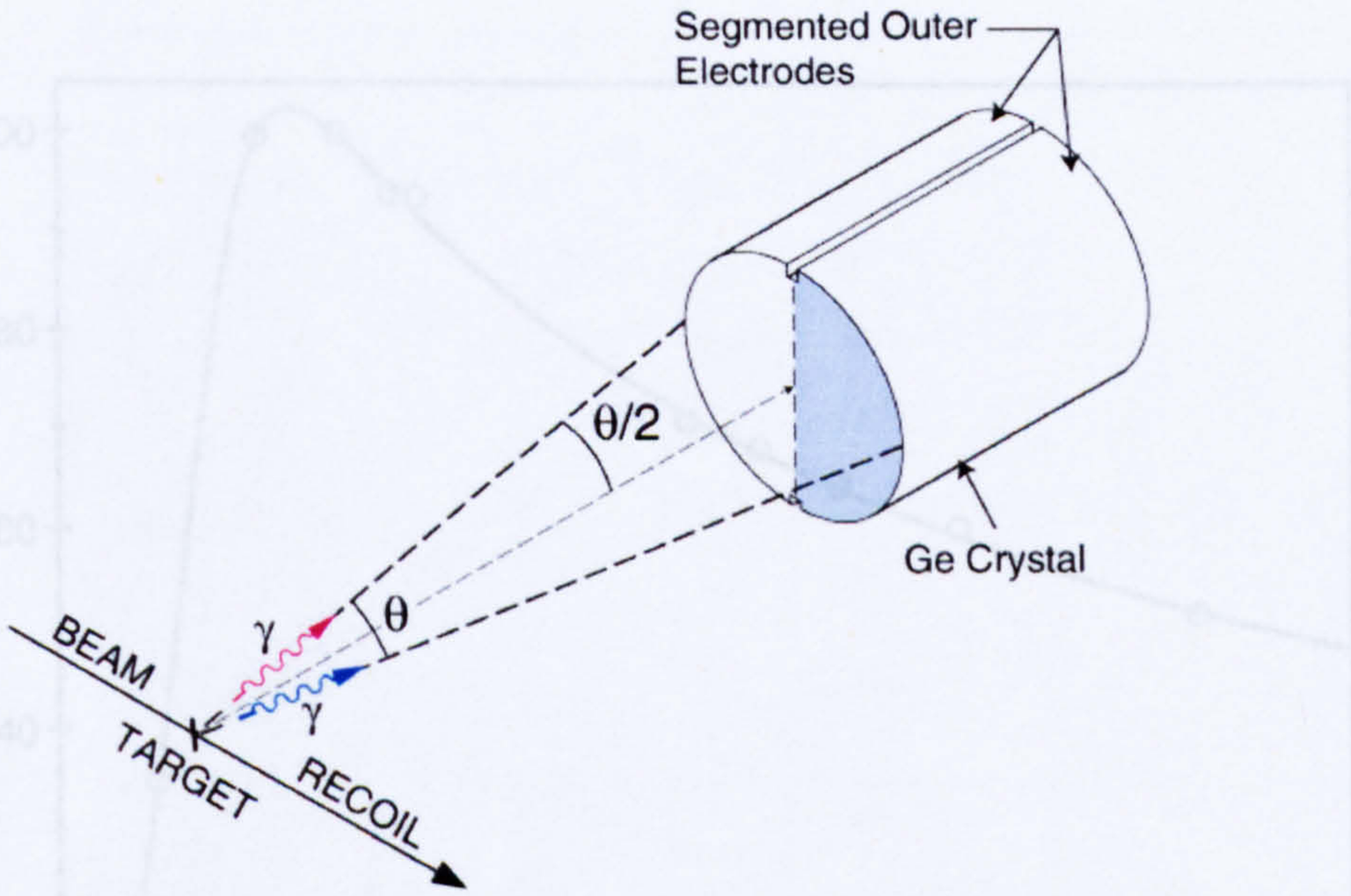

Figure 3.3: A schematic diagram of the electrically segmented detectors used within Gammasphere.

3.2.1 Efficiency calibration

The relative efficiency response of Gammasphere for the current study has been calibrated using a ^{152}Eu radioactive source which emits gamma rays of known energy and intensity. Using this source the efficiency has been determined as a function of gamma-ray energy over a range of energies from 120 keV to 1.4 MeV. This is plotted in Fig. 3.4 where the data points are shown alongside a smooth fitted curve which has been obtained using the fitting routine Effit [Rad00]. Fig. 3.4 reveals a maximum efficiency for gamma rays at approximately 250 keV. Below this energy the efficiency of the array decreases dramatically due to the absorption of gamma rays in the material between the target and the germanium detectors. This material consists of the aluminium casing of the detector, the walls of the target chamber and particularly the Microball charged particle detector which is positioned around the target position and within Gammasphere.

3.2.2 Measured recoil velocity

From the discussion of Doppler effects in Section 2.5, it is apparent that an accurate measurement of the recoil velocity is necessary to obtain a good energy resolution. The Gamma-

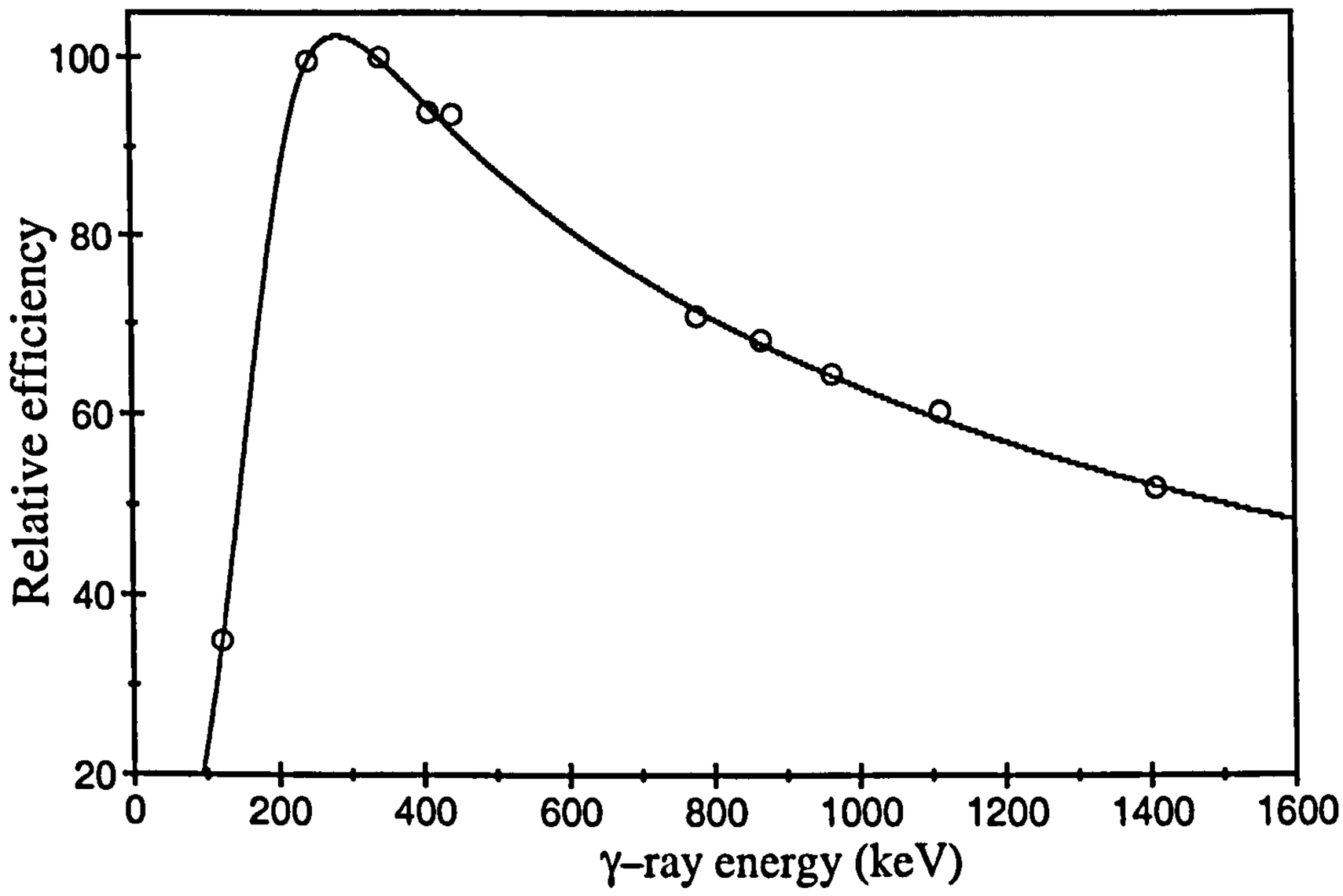

Figure 3.4: Relative detection efficiencies of the Gammasphere array as a function of gamma-ray energies. The data was constructed using a ^{152}Eu radioactive source. The solid line corresponds to a fit of the data points performed using the Effit fitting routine [Rad00].

sphere array, in the configuration employed in the present study, comprises twelve rings of detectors where each ring denotes a group of detectors which subtend the same radial angle θ to the beam direction. Therefore, by considering individual rings, the energy response of the detectors can be obtained as a function of θ. To evaluate the velocity of the recoiling nuclei, the measured energy of the 241 keV gamma ray originating from ^{125}La was found as a function of $\cos(\theta)$, the resulting plot is shown in Fig. 3.5; these particular gamma rays, which arise from a $I^{\pi} = 15/2^{-} \rightarrow 11/2^{-}$ transition, were chosen as they are among the most intense observed in the present study. From Eq. 2.11, the gradient of this plot is given by $E_0\beta$, which yields a $\beta = (v/c)$ value of $4.02 \pm 0.04\%$. However, a more appropriate measure of β, for the ^{124}La nuclei evaporation channel, has been found by measuring the FWHM of the 225 keV gamma ray assuming several β values close to 4.02%, as predicted from the previous measurements. This approach yields a value of $\beta = 4.15\%$ (as shown in Fig. 3.6), and hence this value has been used in the present analysis of ^{124}La.

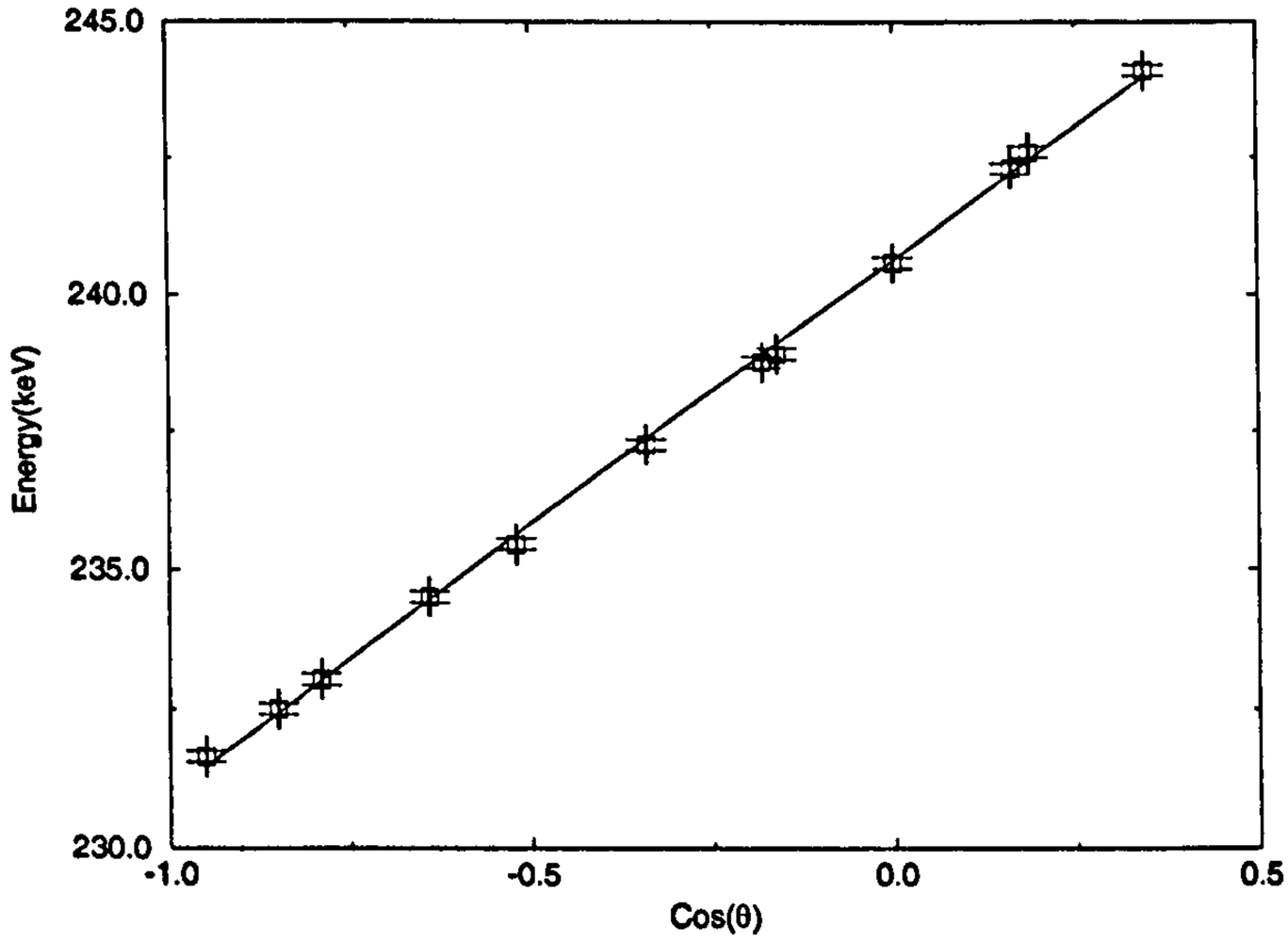

Figure 3.5: A plot of the measured energy of the 241 keV gamma ray transition against $\cos(\theta)$ of the detector angle.

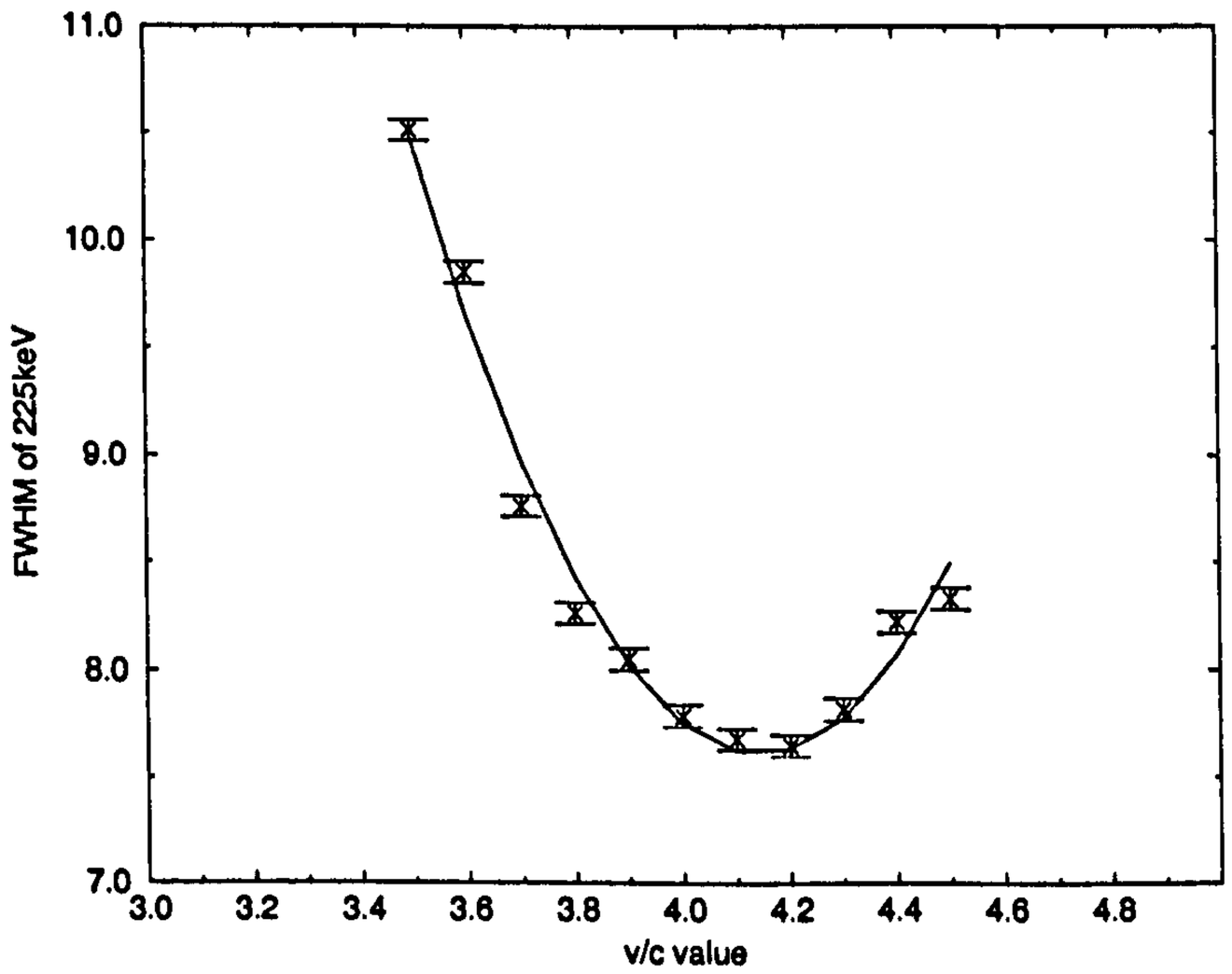

Figure 3.6: A plot of the FWHM of the 225 keV gamma ray transition for values of β, yielding a value of $\beta = 4.15\%$ for ^{124}La.

3.2.3 Angular distributions

Gamma rays of a given multipolarity exhibit an angular dependence relative to the axis of alignment defined by the total angular momentum, **I**, of the nucleus. In the case of a heavy-ion fusion evaporation reaction, the angular momentum of the compound nucleus, and to a good approximation that of the residual nucleus, will be aligned perpendicular to the beam direction. The population of substates of the residual nucleus will therefore produce a cylindrical symmetry relative to the beam direction. The general formula for the gamma-ray intensity as a function of radial angle (θ), where θ is defined relative to the beam direction, is given by,

$$W(\theta) = \sum_{k=0}^{k=2l} A_k P_k(\cos\theta). \tag{3.1}$$

Here, the summation is taken up to $2l$ where l is the highest multipole order of the radiation, P_k is a standard Legendre polynomial, and A_k is the angular distribution coefficient which depends upon the initial and final spins as well as the angular momentum taken by the gamma-ray. If there is any mixing of different multipolarities then A_k also depends upon the mixing ratio δ. Empirical values of A_k are obtained from fitting Eq. 3.1 to measured angular intensities and can subsequently be compared with values obtained from a theoretical approach [Yam67], to yield a determination of transition multipolarity. In the case of a pure dipole transition, only the first term (A_2) is required, whereas to fit the intensity of a quadrupole, or mixed dipole the first two terms (A_2 and A_4) should be applied. As an example of model values, the first angular distribution coefficient expected for a stretched quadrupole transition is $A_2 \sim +0.3$, and for a stretched dipole transition it is expected to be $A_2 \sim -0.3$. Due to its high level of symmetry, Gammasphere is an excellent device for measuring the angular distributions of gamma rays.

3.3 The Microball

The Microball is an array of inorganic-scintillator detectors, employed in conjunction with Gammasphere for the detection of charged particles. Caesium iodide (CsI) is the primary scintillator material used in the detectors while thallium (Tl) is employed as an *activator*. The role of an activator is to modify the crystal lattice of the scintillator such that available states are introduced into the gap between the conduction and valence bands.

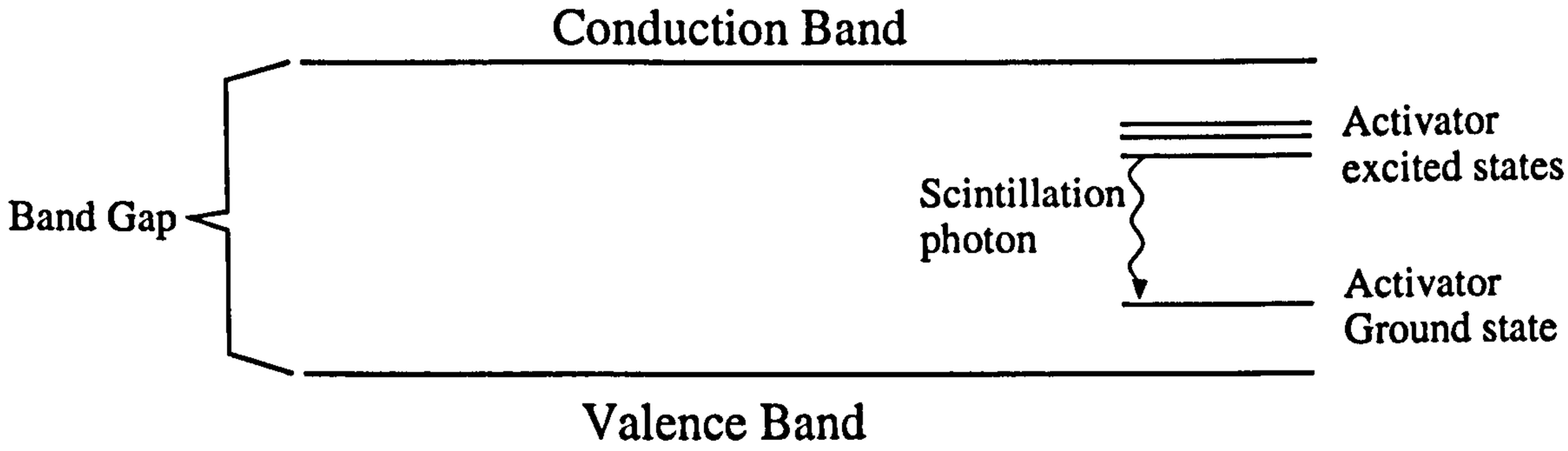

Figure 3.7: Energy band structure of an activated crystalline scintillator.

This modification of the scintillator band structure is displayed schematically in Fig. 3.7. When a charged particle interacts within the scintillator material and excites an electron above the band gap, the electron de-excites not to the valence band, but instead to one of the introduced activator states within the band gap. A careful choice of the activator material ensures that subsequent transitions from these states emit photons in the visible region which can consequently be collected in a photomultiplier tube [Kno89] [RCA70] and converted into an electrical current. The Microball employs silicon photodiodes to perform the latter operation.

In total, 95 CsI(Tl) detectors comprise the array and are arranged such that they cover 98% of the 4π solid angle. The detectors are positioned in 9 rings with increased segmentation at forward angles as shown in Fig. 3.8. This arrangement accommodates the tendency for emitted particles to be forward focussed and is designed to allow an approximately equal count rate in each element. In the current study the purpose of the Microball was to assist in evaporation channel selection. This requires the successful identification of the charged particles emitted during compound nuclear decay.

3.3.1 Particle Identification in the Microball

The signal originating from a CsI(Tl) detector has two decay components. The fast component has an amplitude, and decay time $\tau = 0.4$–1.0μs, which are dependent upon the interacting particle type. The slower component has a mean decay time of $\tau = 7\mu$s and

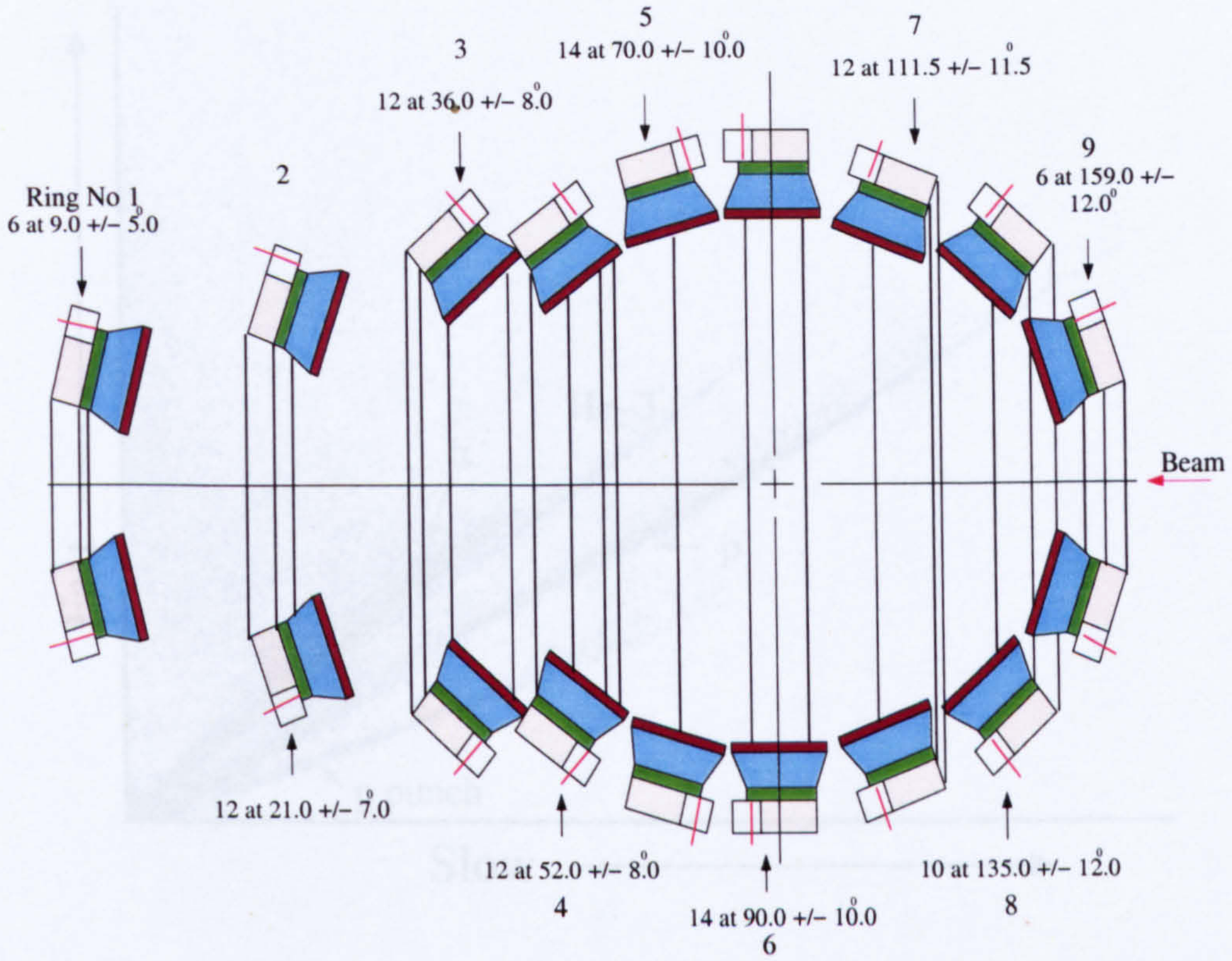

Figure 3.8: Schematic diagram of the Microball charged particle detector arrangement. The detectors are positioned in 9 rings with increased segmentation at forward angles.

is particle-type independent. Excellent particle identification (PID) is achieved using pulse shape discrimination (PSD) to separate these two decay components. By performing separate integration over the two components of the photodiode output signal, Fast and Slow signals can be obtained. The ratio of Slow/Fast is dependent upon the incident particle type and can therefore be used as a means of particle identification. A plot of Fast versus Slow is illustrated in Fig. 3.9 for one of the CsI(Tl) detectors. The result displays a significant discrimination between protons, alpha particles and the small amounts of ^{3}He. The p punch that is indicated in Fig. 3.9 is a result of the proton energy exceeding the ranges in the 1.9mm CsI(Tl), and so appears as punch-through. This pulse shape discrimination is notably effective at high energies. At low energies a complementary discrimination technique is used: zero crossover timing.

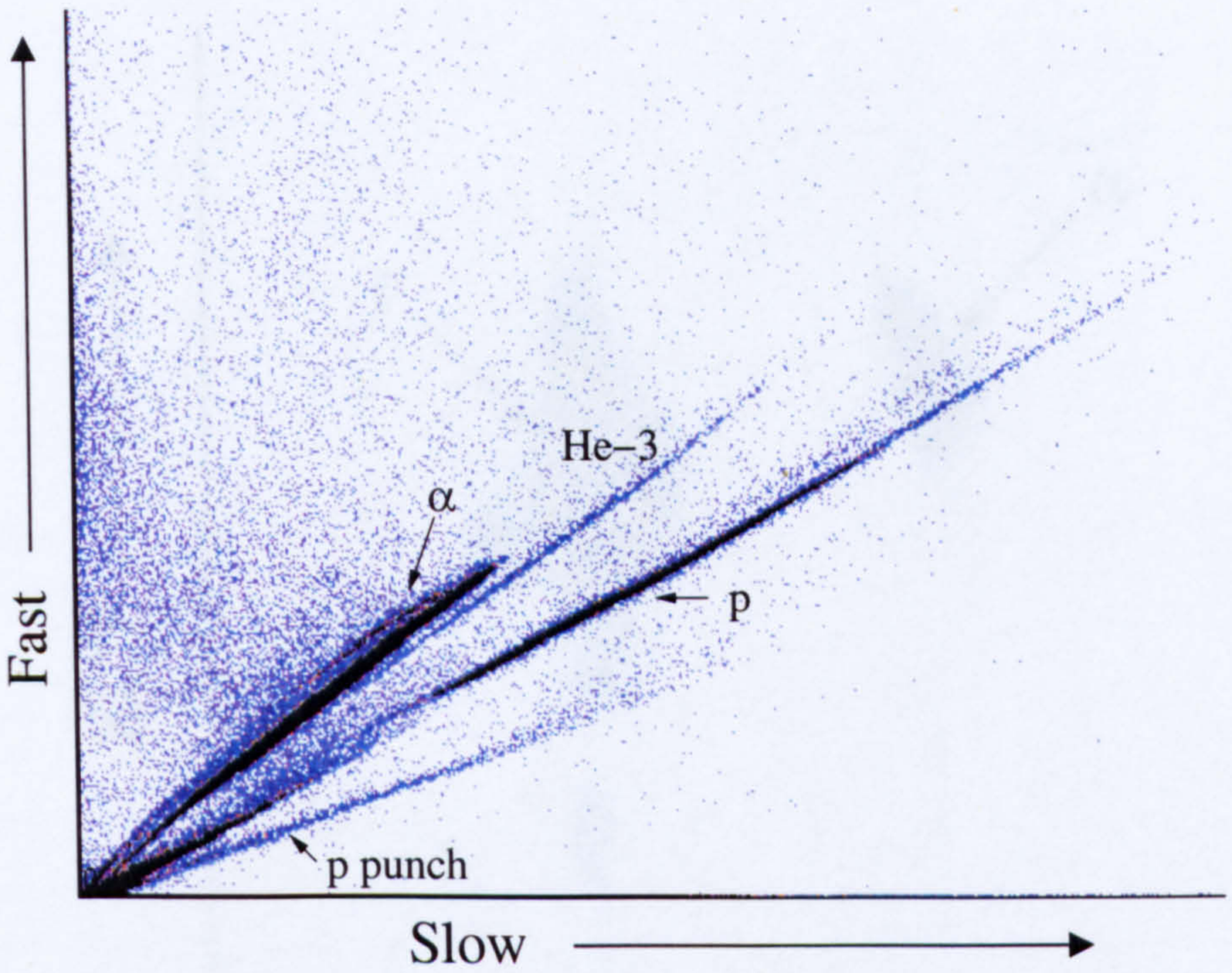

Figure 3.9: A plot of E versus ΔE for one of the CsI(Tl) detectors, displaying significant discrimination between protons and alpha particles. The pulse shape discrimination is notable effective at high energies. Notice the proton punch-through as described in the text.

Zero crossover timing (ZCT) extracts particle identification from the crossover time of the differentiated fast signal of a constant fraction discriminator. This crossover time, with reference timing provided by the ATLAS accelerator, is essentially a measure of the time of flight and as such is different for protons and alpha particles. As the time of flight differs the most at low energies, this technique can be effectively combined with the pulse shape discrimination discussed above. Such a combination is displayed in Fig. 3.10 where the ratio Slow/Fast (denoted R) is plotted against ZCT. In the current study, the evaporation channel of interest is the 3pn channel. The efficiency of the Microball for this experiment was calculated to be 63% for the detection of protons.

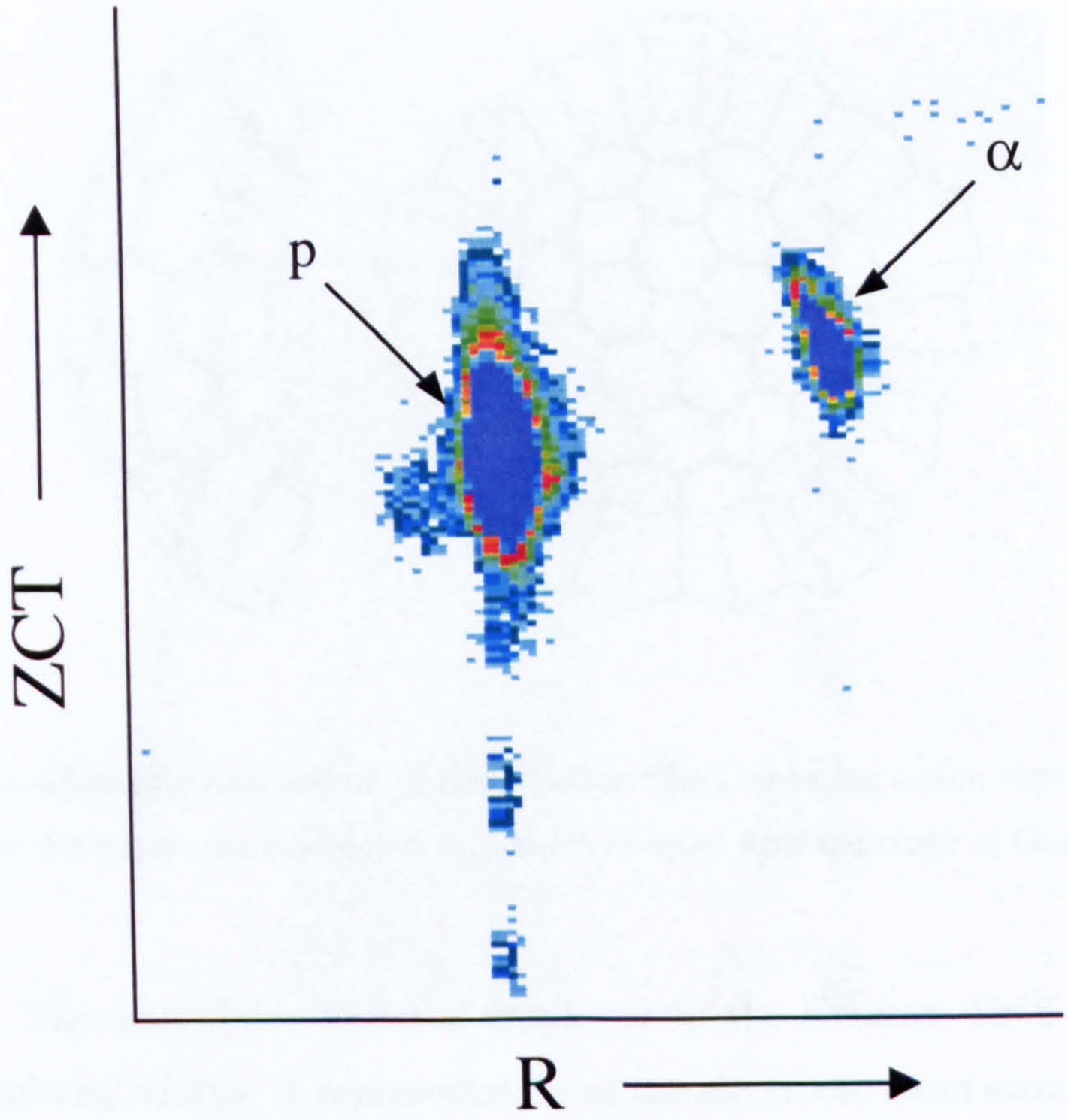

Figure 3.10: A plot of ratio R versus ZCT, with protons and alpha particles labelled.

3.4 The Gammasphere Neutron Shell

The Neutron Shell is an array of organic liquid proton-recoil scintillator detectors which can be substituted for germanium detectors in the Gammasphere array. For the present study the Neutron Shell replaced the five most forward rings of the Gammasphere. This provided an excellent coverage of the neutron emission cone from the target. Illustrations of the Neutron Shell and its position in the Gammasphere are shown in Fig. 3.11 and Fig. 3.2 respectively.

In contrast to inorganic scintillators, organic scintillators do not require a crystal lattice as a basis for the scintillation process. Rather, fluorescence arises from the de-excitation of a single molecule and is observed from a particular molecular species independent of its

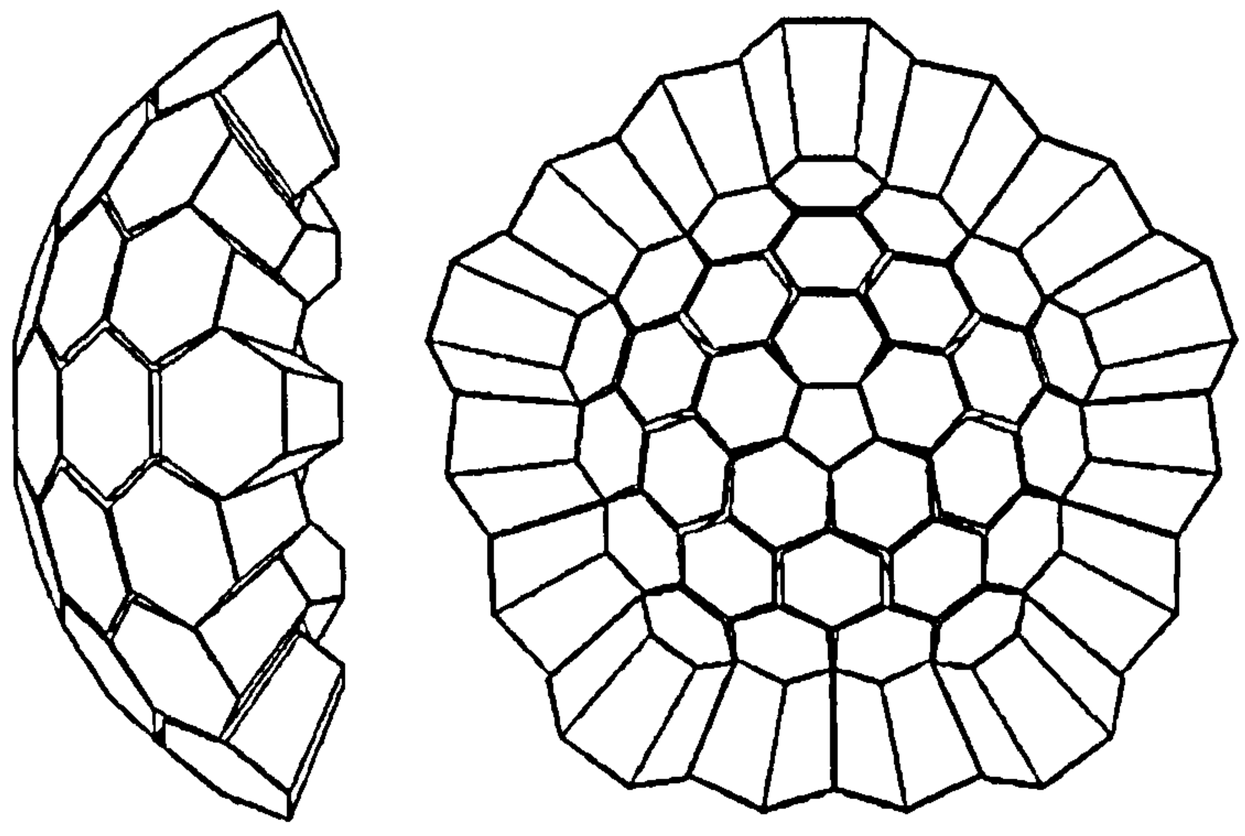

Figure 3.11: A schematic illustration of the Neutron Shell, showing a side view as well a front view of how the detectors are assembled into the five most forward rings of Gammasphere.

physical state. The scintillator material employed in the Neutron Shell detectors is the hydrogen-rich solvent NE213. A representation of the electronic band structure of a NE213 molecule is shown in Fig. 3.12. Spacing between vibrational states is large compared with average thermal energies (0.025 eV), and therefore most molecules are in the ground state at room temperature. The absorption of kinetic energy from a passing charged particle leaves the molecule in an excited state. The system then quickly de-excites from one of the higher singlet states to an S_1 state via radiationless internal conversion. Any molecule left with excess vibrational energy, i.e in an S_{11} or S_{12} state, is not in thermal equilibrium with its neighbours and so quickly loses the excess vibrational energy. The net result of this procedure is a molecule in the excited S_{10} state. It is the subsequent decay from this S_{10} state to an S_0 vibrational state which produces the scintillation photons. As the incident neutron interacts with the material through the scattering of protons, the energy deposited in each individual scattering event may be anywhere between zero and the full kinetic energy of the neutron, leading to poor energy resolution. This is not, in principle, a serious concern for channel selection since it is not the energy of the neutron but merely its presence which is to be measured. However, gamma rays passing through a neutron

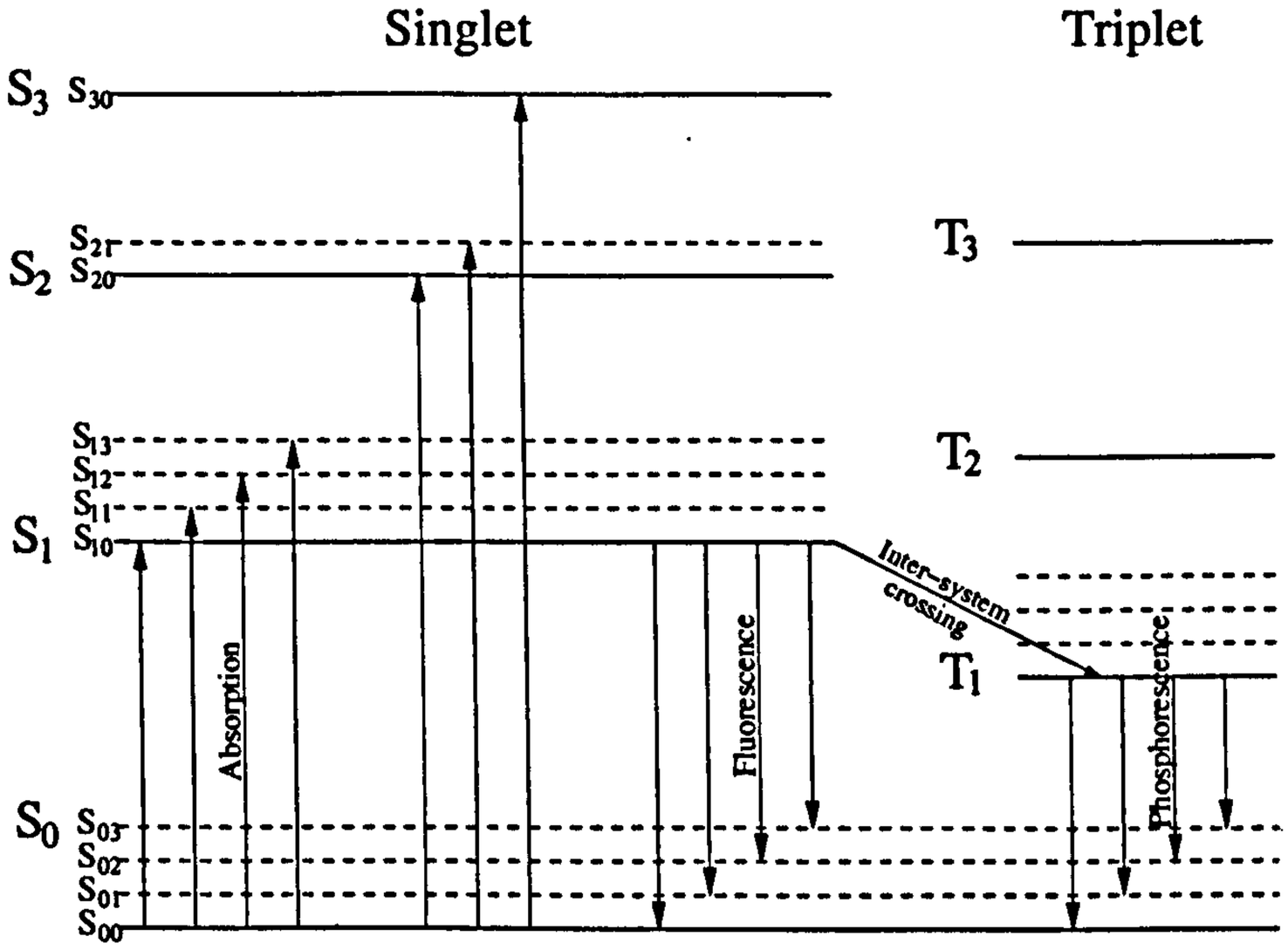

Figure 3.12: Energy levels of an organic molecule. Fluorescence arises from the de-excitation of a single molecule and is observed from a particluar molecular species independent of its physical state.

detector can also interact with the material via Compton scattering. Compton scattered electrons can produce scintillation in the same way as protons and therefore many signals generated by the Neutron Shell may not originate from neutrons but gamma-rays. To perform channel selection some form of particle identification must therefore be applied to discriminate between neutrons and gamma rays.

3.4.1 Particle Identification in the Neutron Shell

The methods employed to perform particle identification in the Neutron Shell are the same as those used in the Microball, namely, pulse shape discrimination and zero crossover timing. Though some of the details differ, in general the two systems are treated in a similar manner. Like the Microball, the Neutron Shell produces signals which have a fast and slow component. The description given in the previous section is the origin of the fast component which is the dominant mode. The details of how the slow component arises will not be described here but in general terms it is created from an aggregation of triplet states

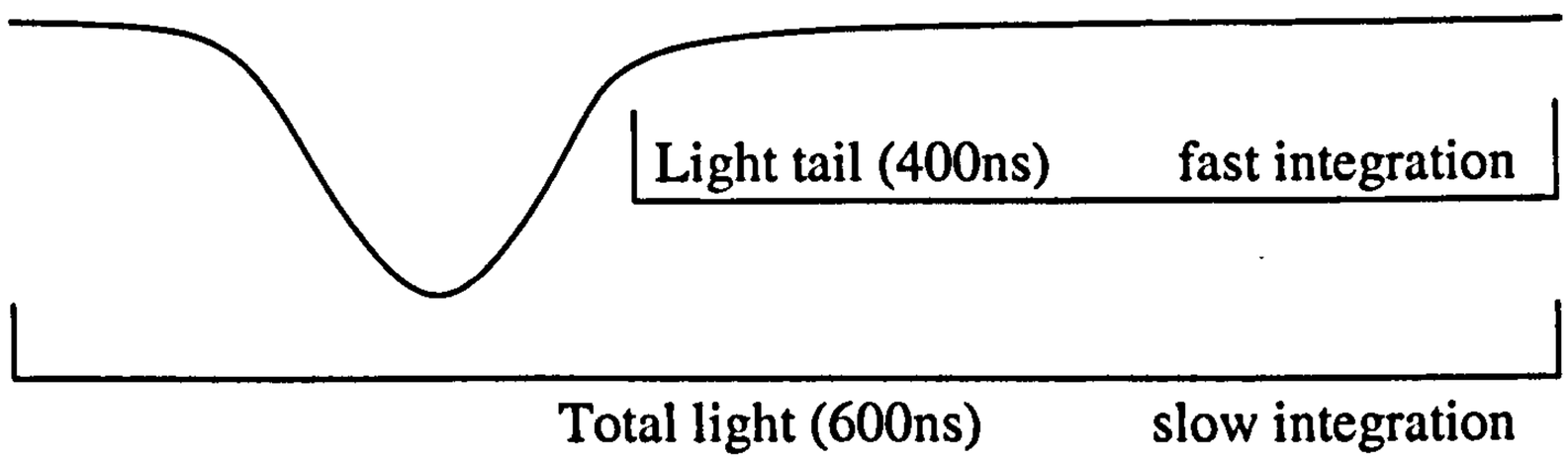

Figure 3.13: An illustration of the anode signal from the liquid scintillator neutron detectors, indicating how the pulse is integrated in order to achieve pulse shape discrimination.

which may couple to form excited singlet states and therefore generate delayed fluorescence. The number of such states, and by association the number of delayed scintillations, is related to the density of the energy deposition caused by the charged particle. This density is higher for recoil protons than electrons, and it is consequently the scattering of neutrons which make the largest contribution to the slow component of the photomultiplier signal. An illustration of the fast component compared to the slow component is shown in Fig. 3.13; the anode signal is integrated in order to achieve pulse shape discrimination.

Zero crossover timing, which is particularly useful in this case due to the dramatic difference in velocity between neutrons and gamma rays, is used in combination with the pulse shape discrimination discussed. This synergy is displayed in Fig. 3.14, where a plot of Slow/Fast (denoted as R) against ZCT is given for a single detector. The neutron-gamma ray discrimination is excellent and polygonal software gates can consequently be set around the neutron region to reject random coincidences and contamination from scattered gamma rays. Employing these techniques, the efficiency of the Neutron Shell was calculated to be 36.5% for the detection of neutrons in the present study.

3.5 The Fragment Mass Analyser

The function of the Fragment Mass Analyser (FMA), or indeed any recoil mass spectrometer, is to separate recoils spatially according to their mass to charge ratio, A/Q. This is achieved by a series of ion-optical bending and focussing elements which separate the

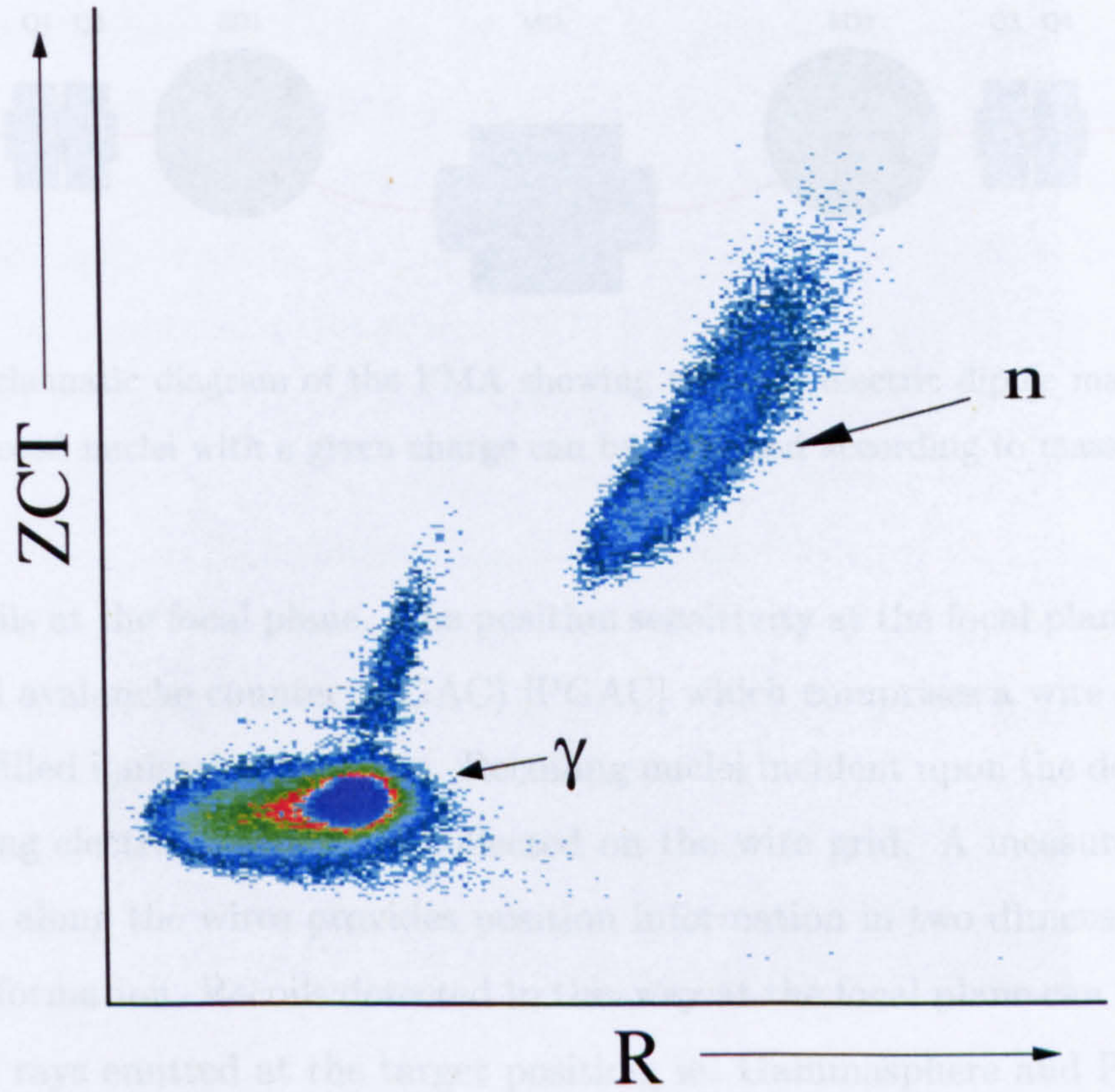

Figure 3.14: A plot of the fast/slow component against the ZCT for the neutron detectors.

recoiling nuclei according to mass and charge and subsequently focus them onto a position sensitive detector. The primary ion-optical elements of the FMA, which are displayed schematically in Fig. 3.15, comprise two electric dipoles (ED1 and ED2) placed either side of a magnetic dipole (MD). The electric dipoles disperse the recoils with a given charge state according to energy, and the magnetic dipole disperses the recoils according to momentum. The magnetic and electric dipoles are matched in such a way that the energy dispersion produced by the magnetic dipole exactly counteracts the energy dispersion produced by the electric dipoles. This has the net effect of dispersing the recoils with a given charge state according to mass alone. Recoils of the same mass, despite possessing significantly different energies, will therefore be transported to the same position at the focal plane. This arrangement, which is commonly used to achieve A/Q dispersion is called the *split electric dipole mass separator*. Additional magnetic quadrupoles are positioned before (Q_1 and Q_2) and after (Q_3 and Q_4) the primary elements to enhance the angular acceptance of the FMA

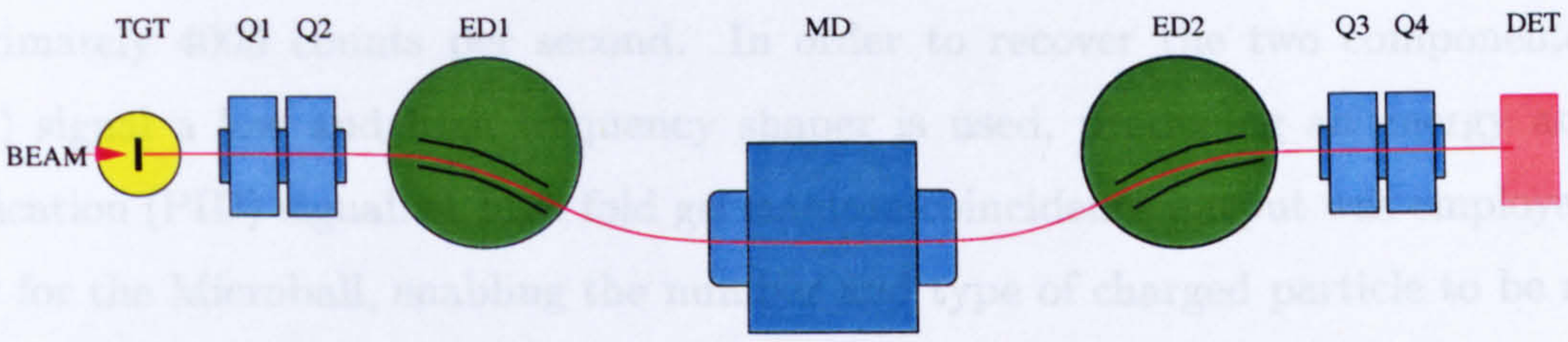

Figure 3.15: Schematic diagram of the FMA showing the split electric dipole mass sparator arrangement. Recoil nuclei with a given charge can be dispersed according to mass alone.

and to focus recoils at the focal plane. The position sensitivity at the focal plane is provided by a parallel grid avalanche counter (PGAC) [PGAC] which comprises a wire grid situated in front of a gas-filled ionisation chamber. Recoiling nuclei incident upon the detector ionise the gas, producing electrons which are collected on the wire grid. A measurement of the charge deposited along the wires provides position information in two dimensions (x, y) as well as timing information. Recoils detected in this way at the focal plane can be correlated with the gamma rays emitted at the target position, ie. Gammasphere and PGAC signals can be correlated. This allows the selection of gamma rays associated with a particular recoil mass and is an extremely powerful technique for studying weak evaporation channels or for suppressing much stronger channels. The FMA provides very clean mass separation and is therefore a very effective tool for channel selection. The efficiency of the device was measured to be approximately 4% for the reaction used in the current study.

3.6 Signal Processing

Each HPGe detector within the Gammasphere array provides three major signals. Two of the three are energy signals, one for a high resolution readout and the other for a low resolution output. A third signal is a timing logic pulse employed in the determination of gamma-ray coincidences. The seven elements of the HPGe BGO shield each give a sum energy output, and a logic pulse that is associated with a discriminator used for Compton suppression when analysed with the germanium timing signal. The preamplifiers associated with the Microball are charge sensitive, producing integrated pulses with a 600 ns rise time

and a 300 μs decay time and thus limiting the counting rate of each of the detectors to approximately 4000 counts per second. In order to recover the two components of the CsI(Tl) signal a low and high frequency shaper is used, producing an energy and pulse identification (PID) signal. A high fold germanium coincidence output was employed as the trigger for the Microball, enabling the number and type of charged particle to be recorded in coincidence with a gamma-ray cascade. FERA (Fast Encoding and Readout ADCs) modules were used to digitise the signals resulting in outputs for detector number, energy, zero crossover time, and PID. The Neutron Shell signal processing begins with the anode signal produced from a photomultiplier tube; it is fed into two separate units, one for pulse shape discrimination and one for time-of-flight from which the ZCT signal is produced. The five outputs from the neutron shell electronics are composed of two time-of-flight signals, two pulse shape discrimination outputs, one fast and one slow, and a fifth giving the number of detectors that fired in a given event. As with the Microball, the trigger is a high-fold germanium signal from Gammasphere. The FMA is triggered likewise, and produces two signals, a position signal for the A/Q ratio and a time-of-flight signal.

Chapter 4

Results and Data Analysis

The results of the investigation of ^{124}La are presented within this chapter. A description is given of the various methods employed to select the events of interest. The energy level scheme constructed from this study is presented and the observed rotational bands are subsequently described. The chapter begins with a summary of previous investigations of doubly odd ^{124}La.

4.1 Previous studies

The first observation of ^{124}La was from the study of the radioactive decay of ^{124}La into ^{124}Ba by Idrissi *et al* [Idr92] in 1992. Two isomeric states in ^{124}La were proposed, a low-spin isomer and a high-spin ($I^{\pi} = 7^{-}$ or 8^{-}) isomer with a half life of 29 s. The first high-spin study of ^{124}La was performed by Komatsubara *et al.* [Kom93] in 1993, using gamma-ray spectroscopy. From this experiment, high-spin states in ^{124}La were identified, but spin assignments were not made; the energy level scheme constructed is shown in Fig. 4.1. Subsequently, Liu *et al* [Liu96] performed a systematic study of ^{124}La along with neighbouring isotopes in 1996, and were able to tentatively assign spins and parities to the previously observed bands. The bandhead of the yrast configuration ($\pi h_{11/2} \otimes \nu h_{11/2}$) was proposed to have $I^{\pi} = 7^{+}$ and signature staggering was investigated.

The present investigation into ^{124}La was performed to increase the knowledge of high-spin states in this nucleus and further study its energy staggering. However, to obtain this information it was essential to assign spins and parities to the observed bands. For

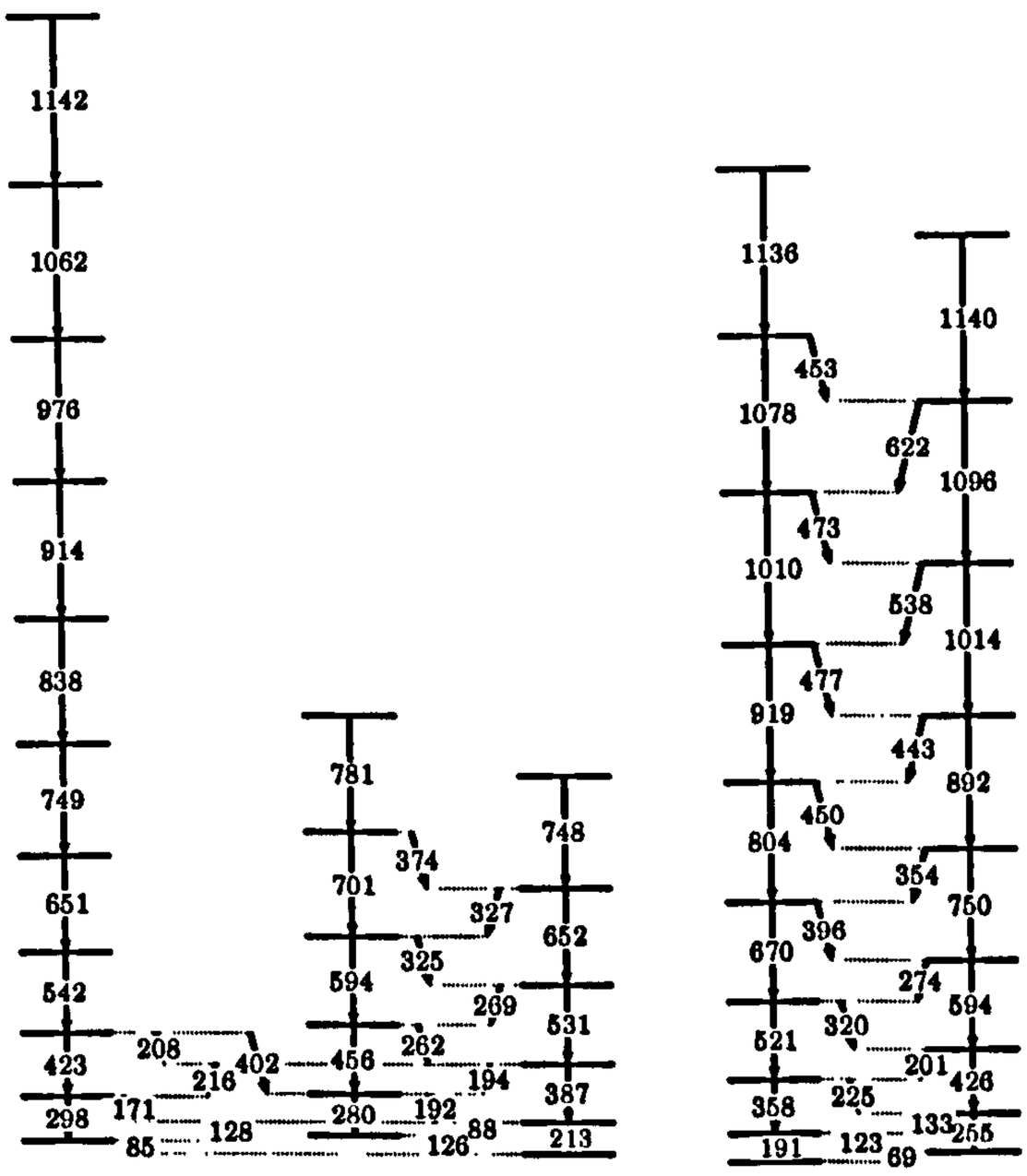

Figure 4.1: The energy level scheme constructed for ^{124}La prior to this work [Kom93].

this reason, it was particularly important to identify inter-band linking transitions so that relative assignments could be determined.

4.2 Channel selection

In total, 1.06×10^9 events meeting the master trigger conditions were recorded to magnetic tape for post-experiment analysis. The master trigger for this experiment required the detection of either three gamma rays in coincidence, two gamma rays plus an event recorded in the Neutron Shell, or two gamma rays plus an event recorded by the FMA. Recalling Fig. 3.1, it is apparent that to study ^{124}La using the ^{64}Zn + ^{64}Zn reaction at 260 MeV requires significant suppression of those channels which compete with 3pn evaporation and that channel selection is required; the combination of the ancillary detectors described in Chapter 2 plus the Gammasphere array has been used for this purpose. The first stage of selection is provided by the Microball. The Microball can effectively identify protons which

are emitted from a compound nucleus during particle evaporation. The number of protons detected simultaneously therefore gives an indication of the evaporation channel through which a given compound nucleus has decayed. Gamma rays emitted in an individual event can be correlated with the Microball signal and subsequently, by demanding gamma rays detected in correlation with a certain number of protons, significant evaporation-channel selection can be achieved. The signal originating from the Neutron Shell can be treated similarly, yielding information regarding the neutrons emitted during particle evaporation. A combination of Microball and Neutron-Shell gating has been performed to produce the gamma-ray spectra shown in Fig. 4.2. The second spectrum is incremented only for gamma rays detected in coincidence with a 3p signal from the Microball and a 1n signal from the Neutron Shell. The spectrum consists predominantly of gamma rays originating from ^{124}La and displays the clear advantage of such selection techniques.

4.2.1 Fold and sum energy

It has already been suggested, in Section. 2.6, that a measurement of the fold (k_γ) and sum-energy (H_γ) can be used to enhance particular evaporation channels. The principle here is simple: if a large number of particles are evaporated from a compound nucleus, then the residual nucleus has less excitation energy and will emit fewer gamma rays than a corresponding system formed via fewer-particle evaporation. In the present study, the BGO Compton-suppression shields of the Gammasphere array were employed, together with the HPGe detectors, to obtain H_γ and k_γ. To facilitate this measurement, the Hevimet collimators, which are usually positioned in front of the shields, were removed. Plots of the sum energy and fold distributions are shown in Figs. 4.3 and 4.4, respectively for all the events. A two dimensional plot of fold against sum-energy is displayed in Fig. 4.5. The matrix can be crudely divided into high and low fold-sum energy regions. Taking a cut of this distribution therefore enables gamma rays to be projected which originate from high fold-sum energy or low fold-sum energy events respectively. These alternate projections are displayed in Fig. 4.6. A marked increase in the gamma ray intensity from ^{124}La relative to that from competing channels is observed in the low $H_\gamma - k_\gamma$ cut spectrum.

To enhance the 3p1n evaporation channel, gamma-ray events correlated with a 3p and 0α signal from the Microball, n $\leq$ 1 signal from the Neutron Shell, and with low $H_\gamma - k_\gamma$ were

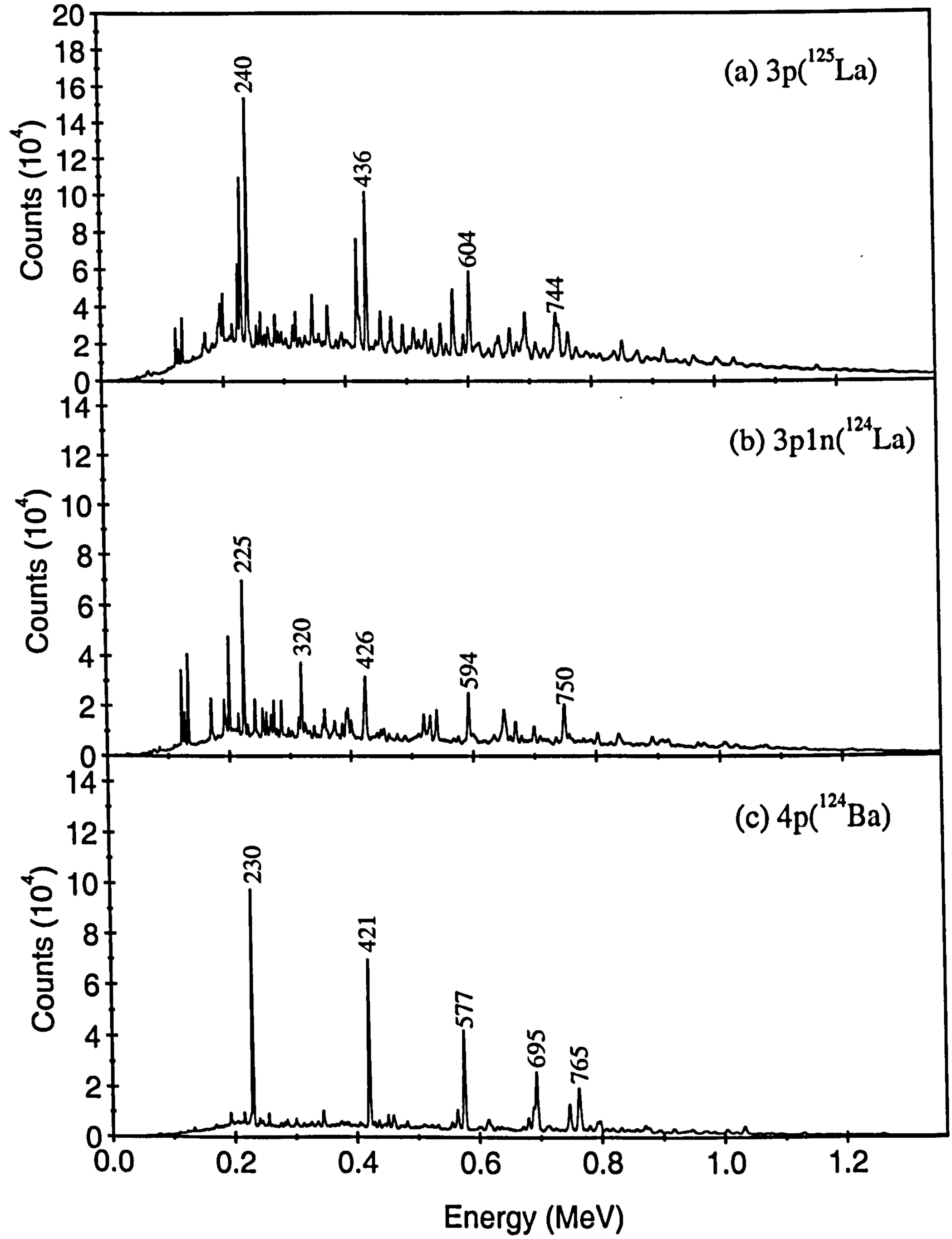

Figure 4.2: Gamma ray spectra produced using a combination of Microball and Neutron-Shell gating. (b) shows the spectrum incremented only for gamma rays detected in coincidence with a 3p signal from the Microball and a 1n signal from the Neutron Shell.

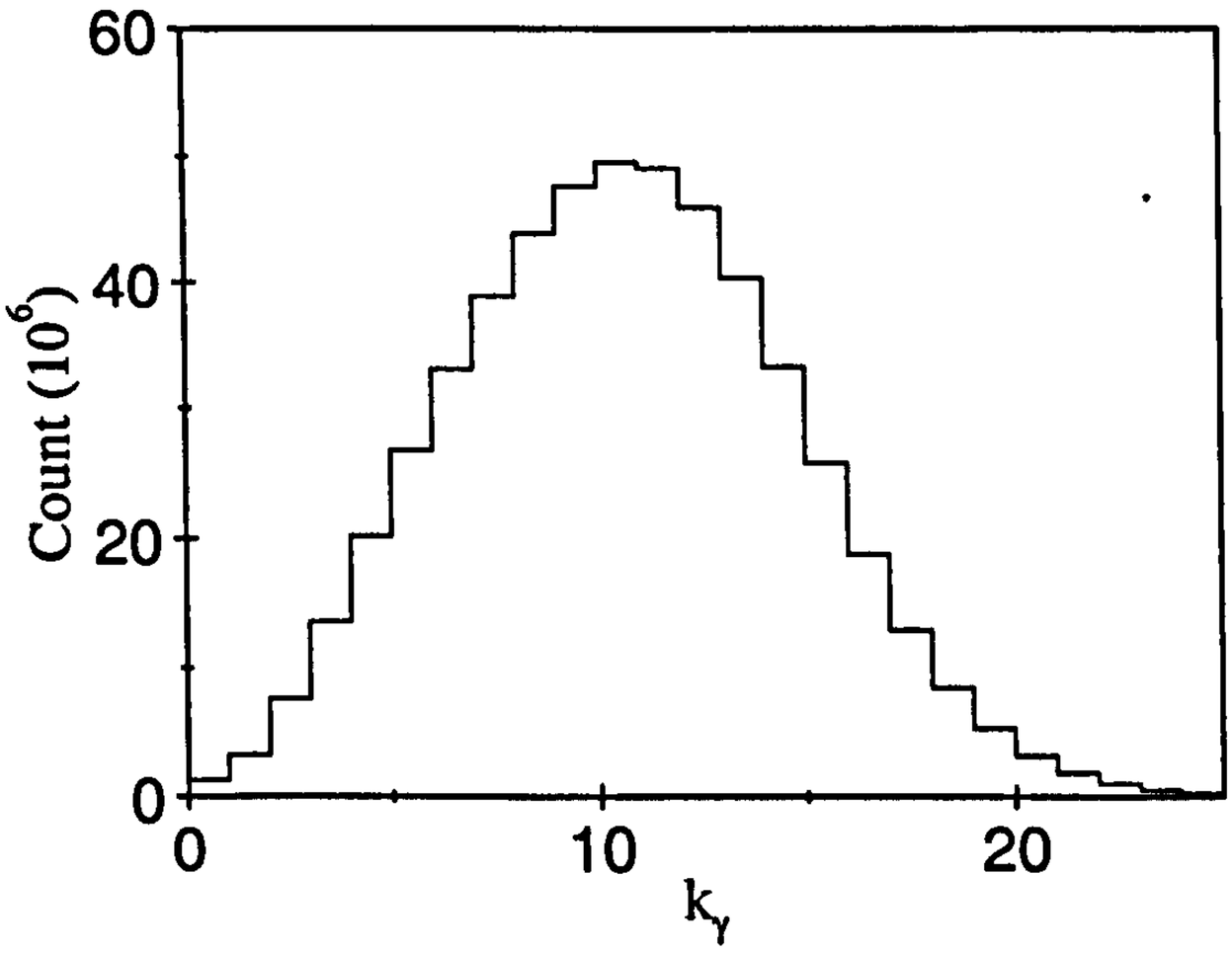

Figure 4.3: A plot of the gamma-ray fold for the total data set, using both the germanium detectors and the BGO detectors.

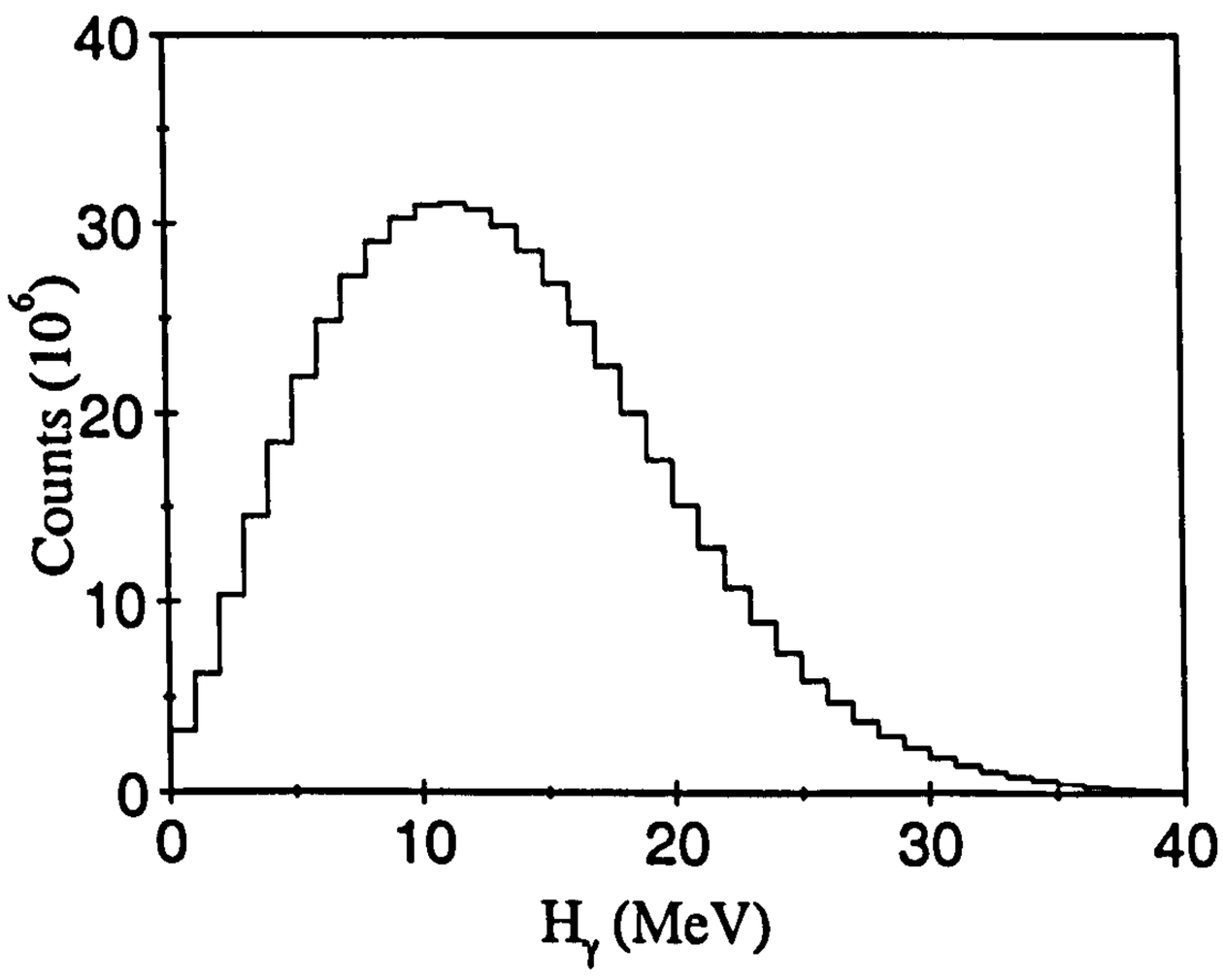

Figure 4.4: A plot of the gamma-ray sum-energy measured with the germanium detectors and the BGO elements, for the total data set.

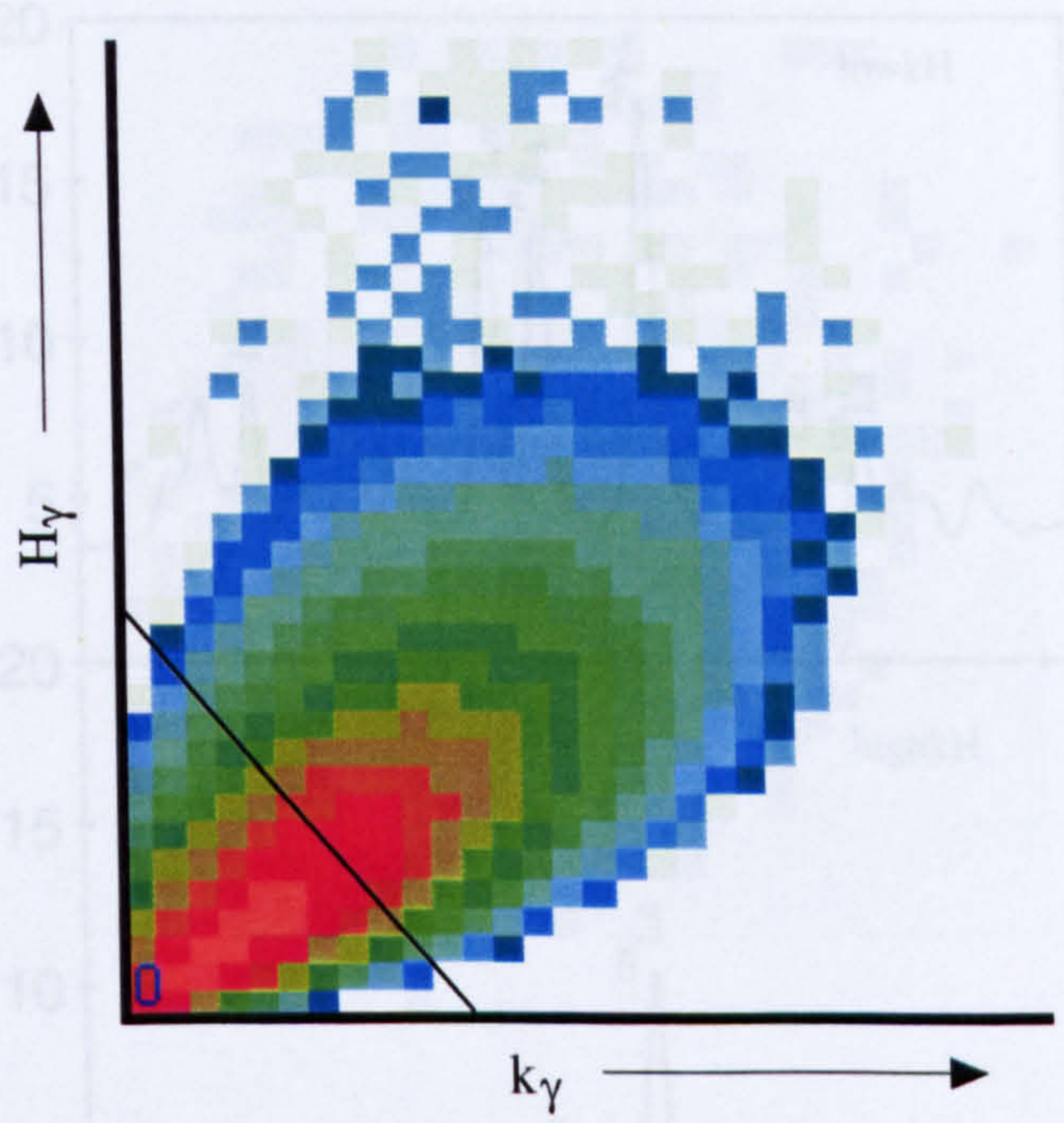

Figure 4.5: A 2-dimensional gamma-ray fold and sum-energy plot for the total data set. An approximate indication of the high and low *cut* is illustrated on the plot.

selected from the measured data. A total of 5.32×10^8 events satisfied such gating conditions. These selected data, of mean gamma-ray fold 3.07, were unfolded into 1.3×10^9 constituent triple gamma-ray coincidence events (γ^3) using the software package incub8r [Rad97]. The unfolded events were subsequently used to increment a Radware-format cube.

4.2.2 Total Energy Plane gating

The methods described thus far were partially successful at providing the desired evaporation channel separation. However, much still relies upon the successful discrimination between the 3p1n and 3p channels, the latter providing much contamination due to its much larger cross-section. Though this discrimination is achievable in principle by demanding a signal from the Neutron Shell, the efficiency of the device is such that a complementary channel selection method is desirable. Such a method, known as Total Energy Plane (TEP) gating has been proposed by Svensson *et al.* [Sve97]. The technique aims to differentiate between events for which the evaporation channels are different but the number of detected

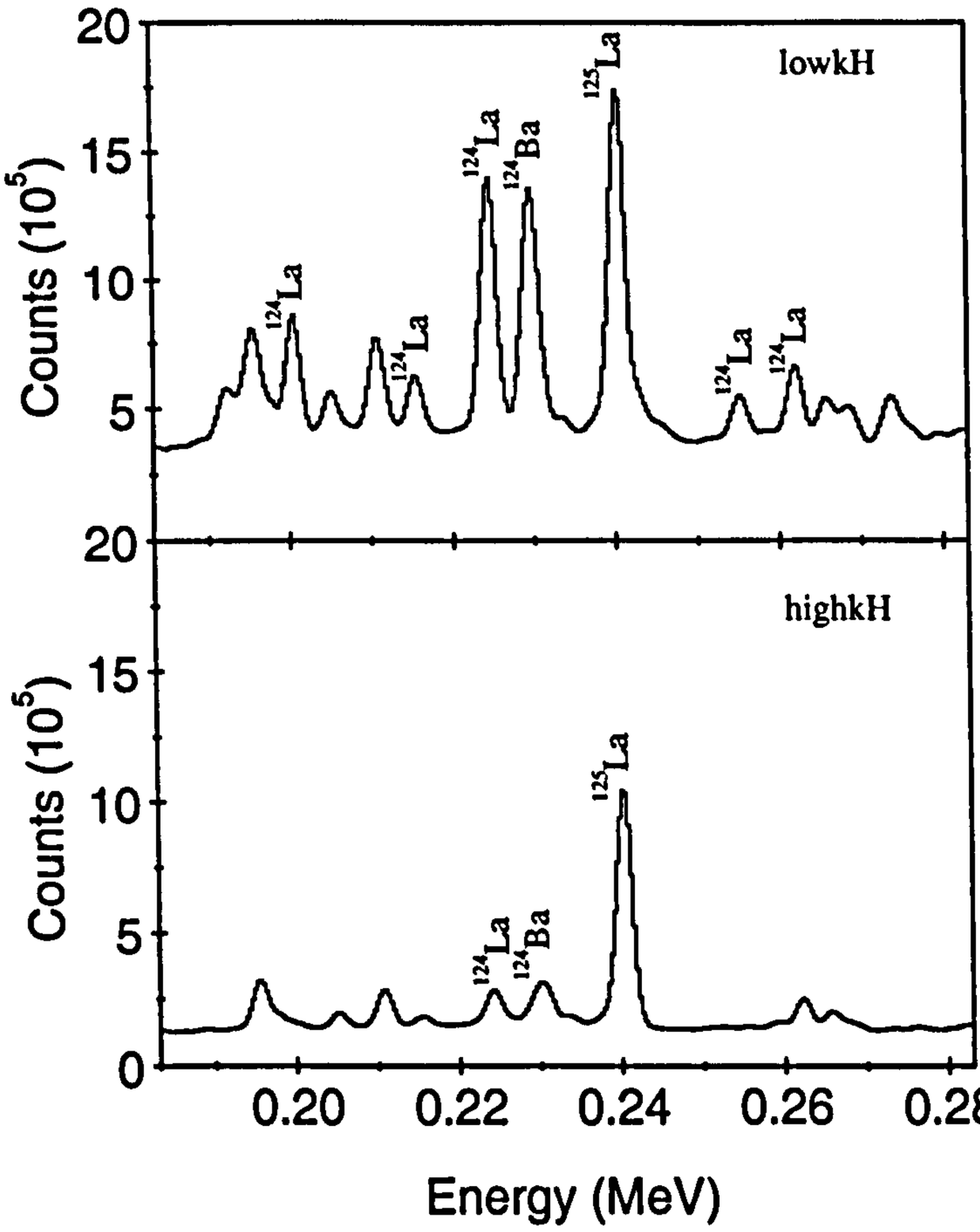

Figure 4.6: Raw spectra gated by (a) low and (b) high fold and sum energy cuts. It can be seen that a low fold and sum energy cut enhances the ^{124}La gamma ray transitions compared with those from the ^{124}Ba and ^{125}La contaminants, improving the ^{124}La channel selection.

charged particles are the same. A fusion-evaporation reaction gives a total energy in the centre of mass frame, E_{CM}, given by:

$$E_{CM} = T_{CM} + Q, \tag{4.1}$$

where T_{CM} is the kinetic energy in the centre of mass frame due to the collision between the projectile and target, and Q is the reaction Q-value for the desired exit channel. This energy is subsequently expended through the emission of particles and gamma rays, giving:

$$E_{CM} = H_\gamma + T_{part}, \tag{4.2}$$

where H_γ is the total gamma-ray energy and T_{part} is the sum of the charged particle kinetic energies in the centre of mass frame. As the 3p evaporation channel has a larger Q-value

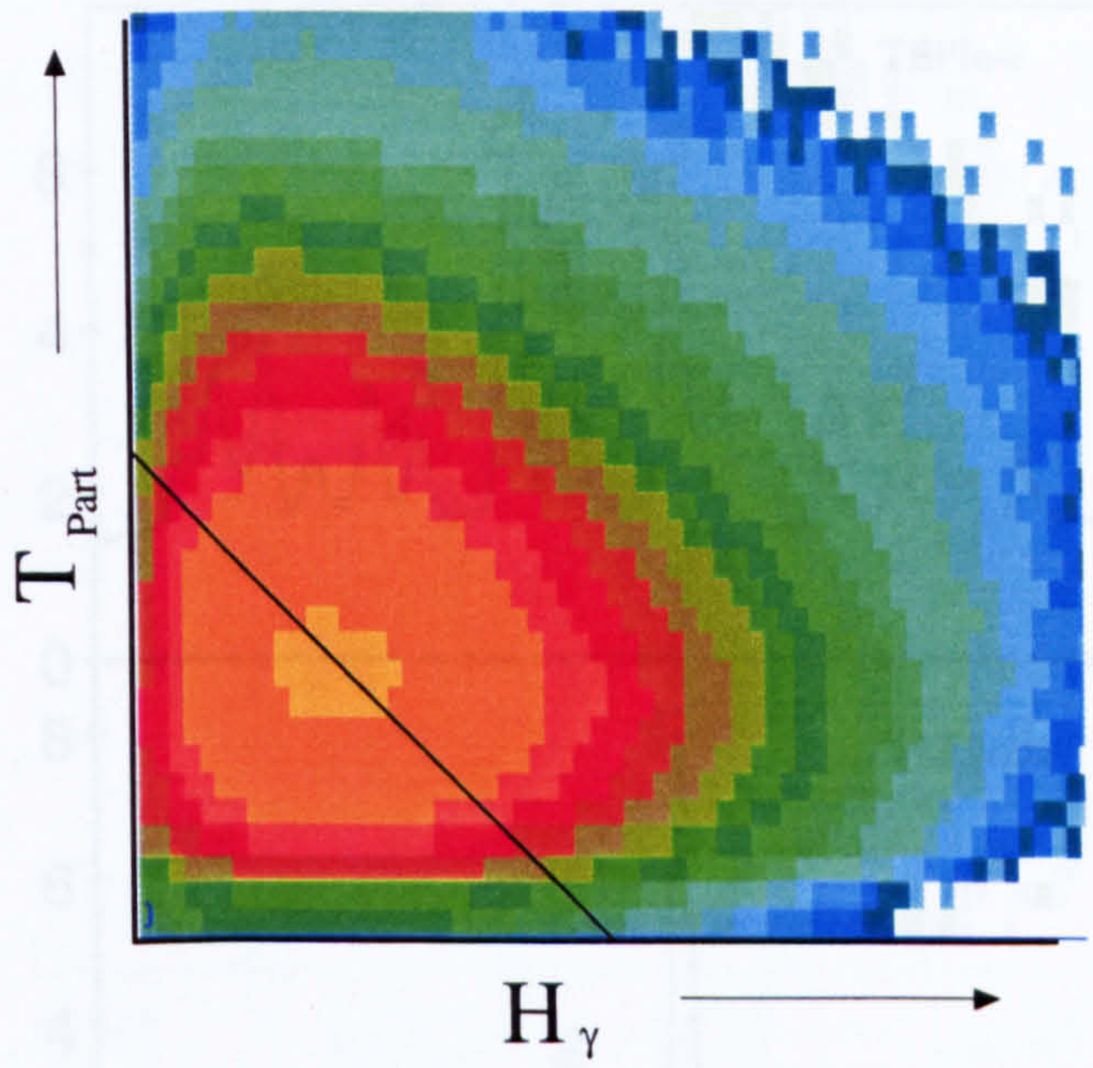

Figure 4.7: A plot of the total γ-ray energy against the sum of the charged particle kinetic energies in the centre of mass frame, i.e a TEP plot. An approximate indication of the position of the cut shown on the plot.

than the 3p1n channel, $H_\gamma + T_{part}$ should be larger for events corresponding to the former case. In addition, if the neutron from the 3p1n evaporation is not detected, then the full T_{part} is not measured and a lower value is assigned. This yields an even greater difference between the measured value of $H_\gamma + T_{part}$ for 3p and 3p1n evaporation channels. By plotting H_γ against T_{part} as shown in Fig. 4.7, the total energy plane is created from which cuts can be taken corresponding to a large $H_\gamma + T_{part}$ and a small $H_\gamma + T_{part}$, denoted here as TEPhigh and TEPlow respectively. The gamma rays gated by these requirements are shown in the two spectra of Fig. 4.8. As expected, gamma rays originating from excited states in ^{124}La are observed in greater relative intensity in the TEPlow-gated spectrum.

A total of 9.8×10^6 events met the low-TEP requirement in addition to Microball, Neutron Shell and $H_\gamma - k_\gamma$ criteria. These events were unfolded to give approximately 10^8 triple gamma-ray coincidences which were used to increment a second cube.

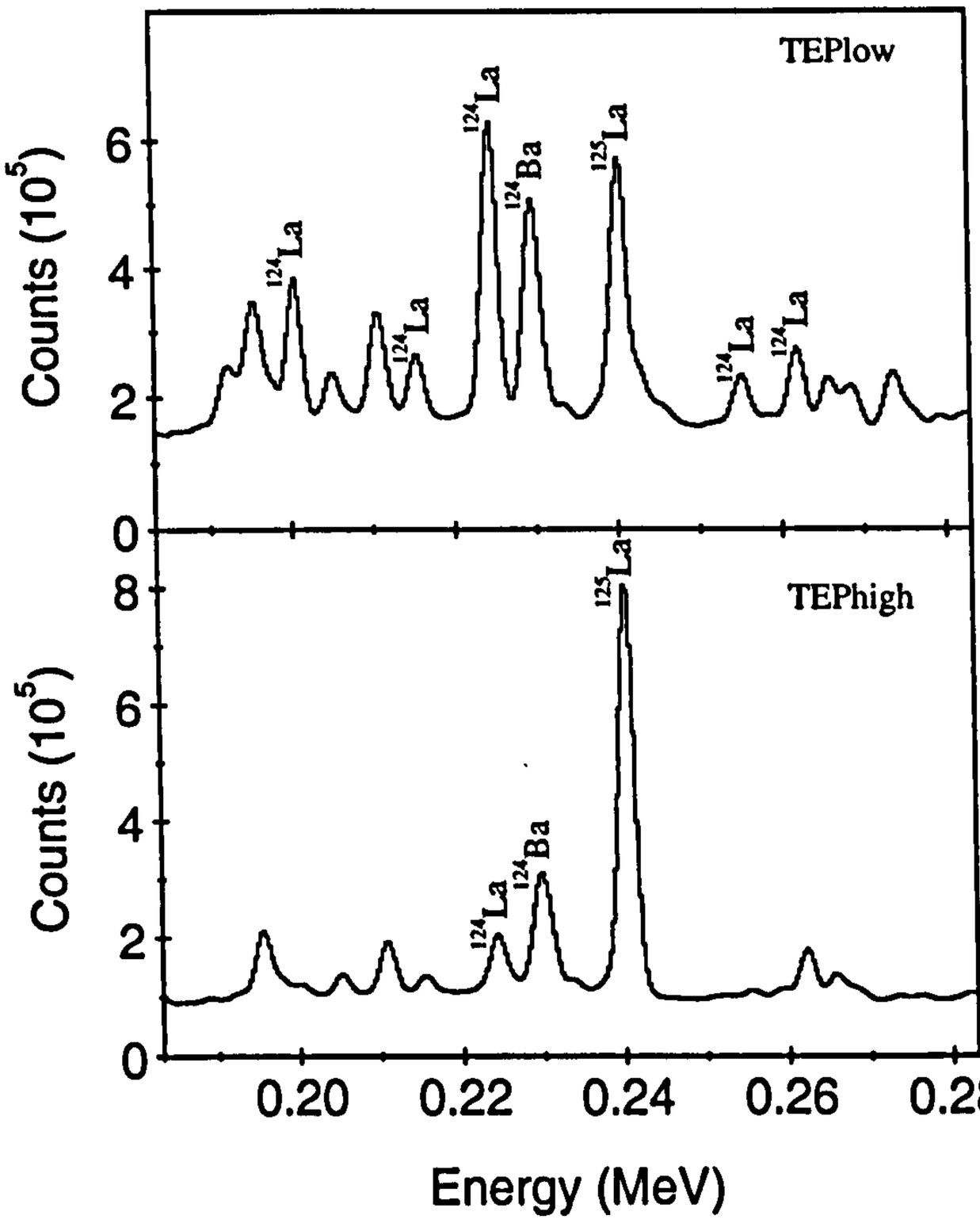

Figure 4.8: Gamma-ray spectra gated upon by (a) low and (b) high TEP cuts. It can be seen that a low TEP cut enhances the ^{124}La gamma ray transitions compared with those from ^{124}Ba and ^{125}La, improving the ^{124}La channel selection.

4.2.3 FMA gating

The FMA provides an extremely clean form of channel selection. However, only a small fraction of the desired events arrive at the focal plane where the A/Q identification is achieved. FMA-gated data were therefore not used directly to construct an energy level scheme for ^{124}La. Nevertheless, FMA-gated spectra have been employed to verify that identified transitions originate from ^{124}La and not contaminant nuclei such as ^{125}La. This was achieved by examining the focal-plane mass spectra correlated with gamma rays of a particular energy. An example of a total mass spectrum is shown in Fig. 4.9. To examine the transitions related to ^{124}La, four gamma ray transitions were used (133 keV, 225 keV,

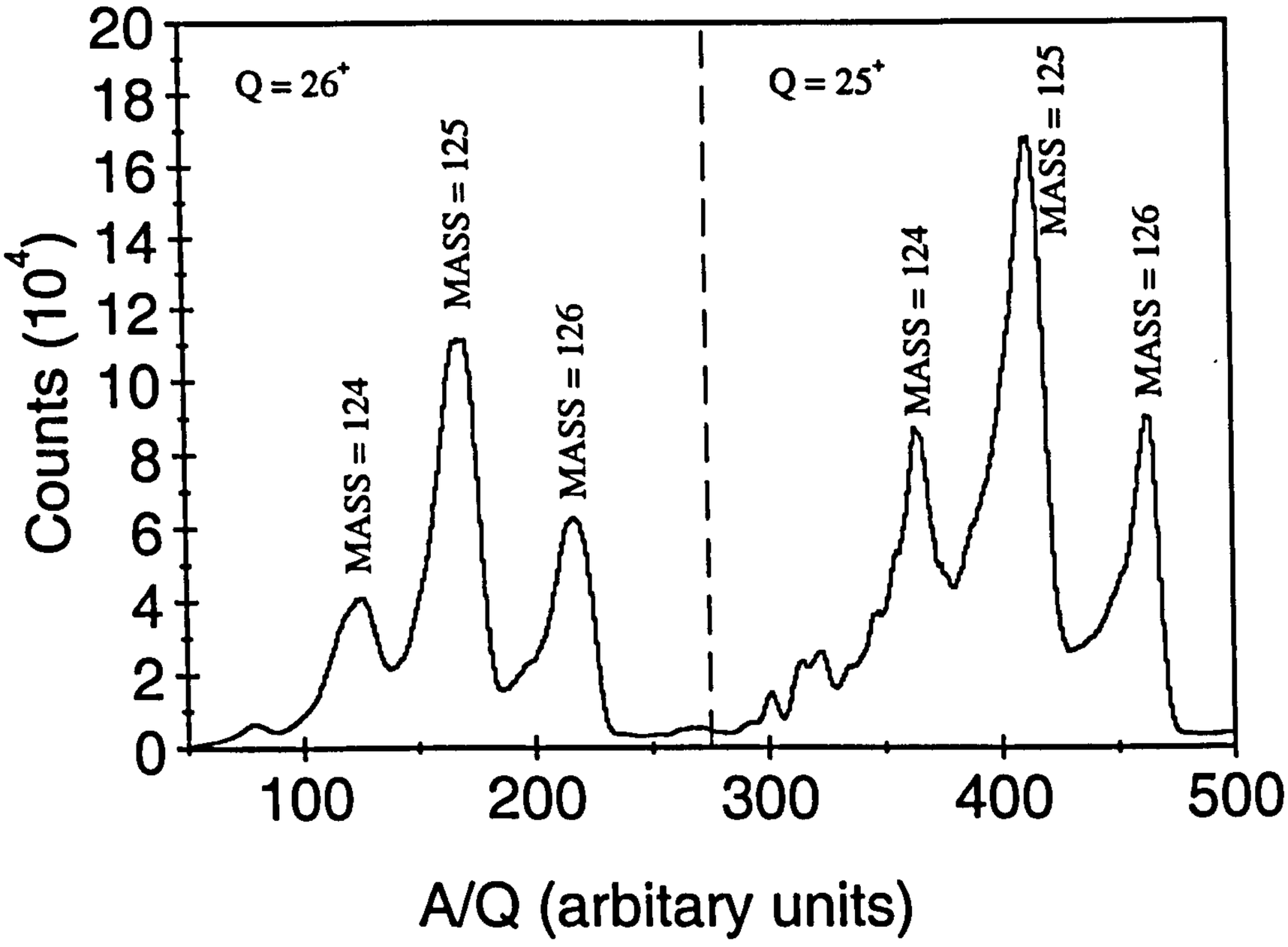

Figure 4.9: A total projection of the A/q data produced from all events. Two charge states, 26^+ and 25^+, are apparent.

320 keV and 594 keV) to create a single correlated mass spectrum. In turn, the mass spectrum was gated upon to produce a gamma ray spectrum consisting of essentially only ^{124}La. Such an approach has proven particularly useful in the case where new transitions have been observed which cannot be linked to the primary band structure, as in this case for band 5.

The comparison between the original raw spectrum and the final one-dimensional gamma-ray spectrum with all gating conditions applied, is shown in Fig. 4.10; Fig. 4.10(b) contains essentially only ^{124}La transitions.

4.3 Rotational band structure of ^{124}La.

The decay scheme of ^{124}La deduced from the present study is shown in Figs. 4.11, and 4.12. The construction of this level scheme was facilitated by the triple (γ^3) coincidence relation-

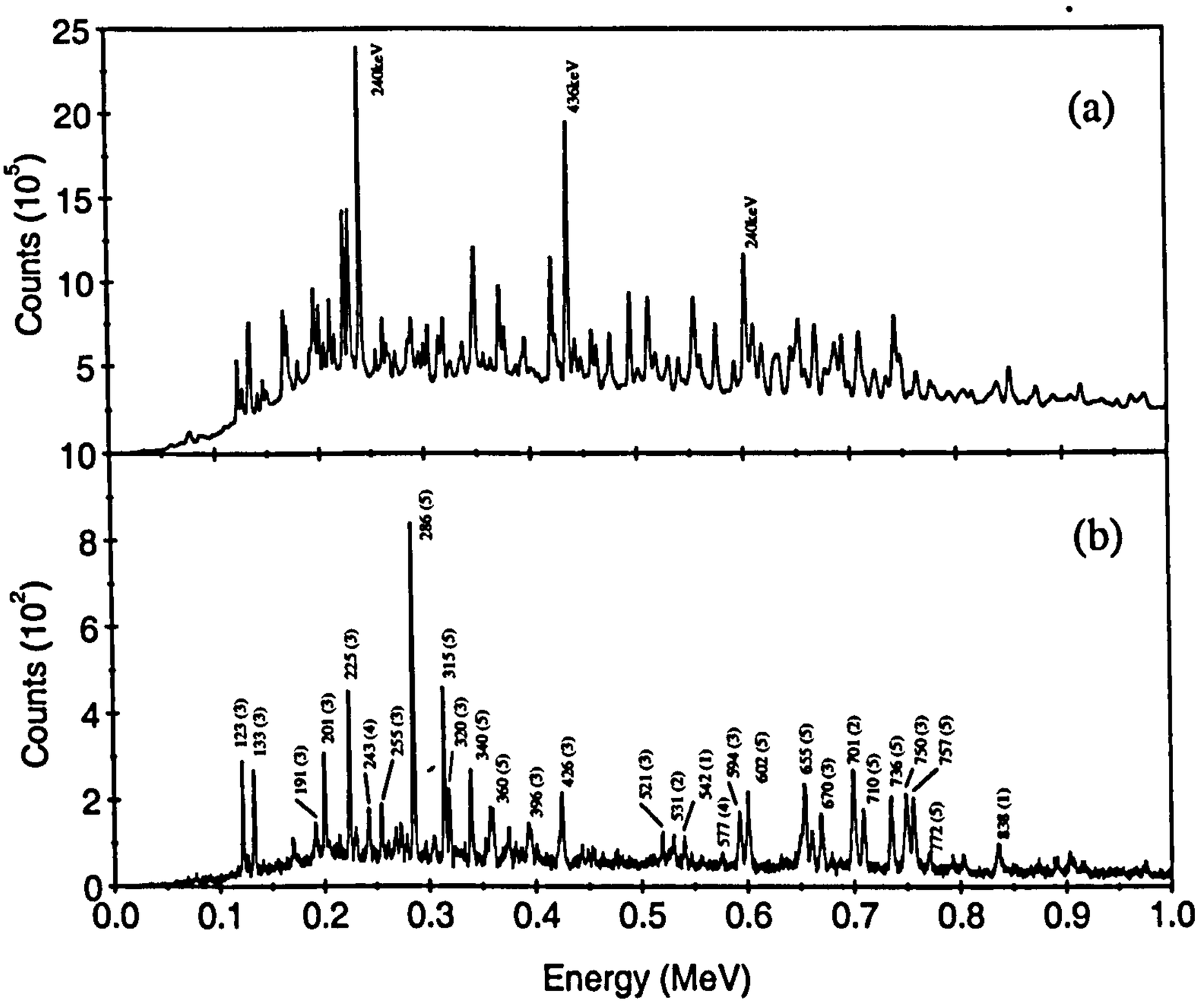

Figure 4.10: Panel (a) displays the raw gamma-ray spectrum produced and Panel (b) shows the gamma-rays selected for ^{124}La through a combination of gating techniques; the transitions are labelled by their energy in keV and band number.

ships deduced between gamma-ray transitions and from relative gamma-ray intensities. As the band shown in Fig. 4.12 has not been linked to the primary structure shown in Fig. 4.11, the level scheme must be considered in two separate sections. The spin and parities of all the bands have been relatively assigned and the significant extension of previously-observed bands, in addition to the observation of new bands, has been achieved. The two correlation cubes described have been used in conjunction with the gated mass spectra of the FMA to examine coincidences between gamma rays originating from ^{124}La. The cubes have been analysed with the LEVIT8R graphical analysis package [Rad95]. Representative one-dimensional spectra obtained from this analysis are displayed in Figs. 4.13, 4.14,and 4.15. The spectra show the rotational bands in ^{124}La.

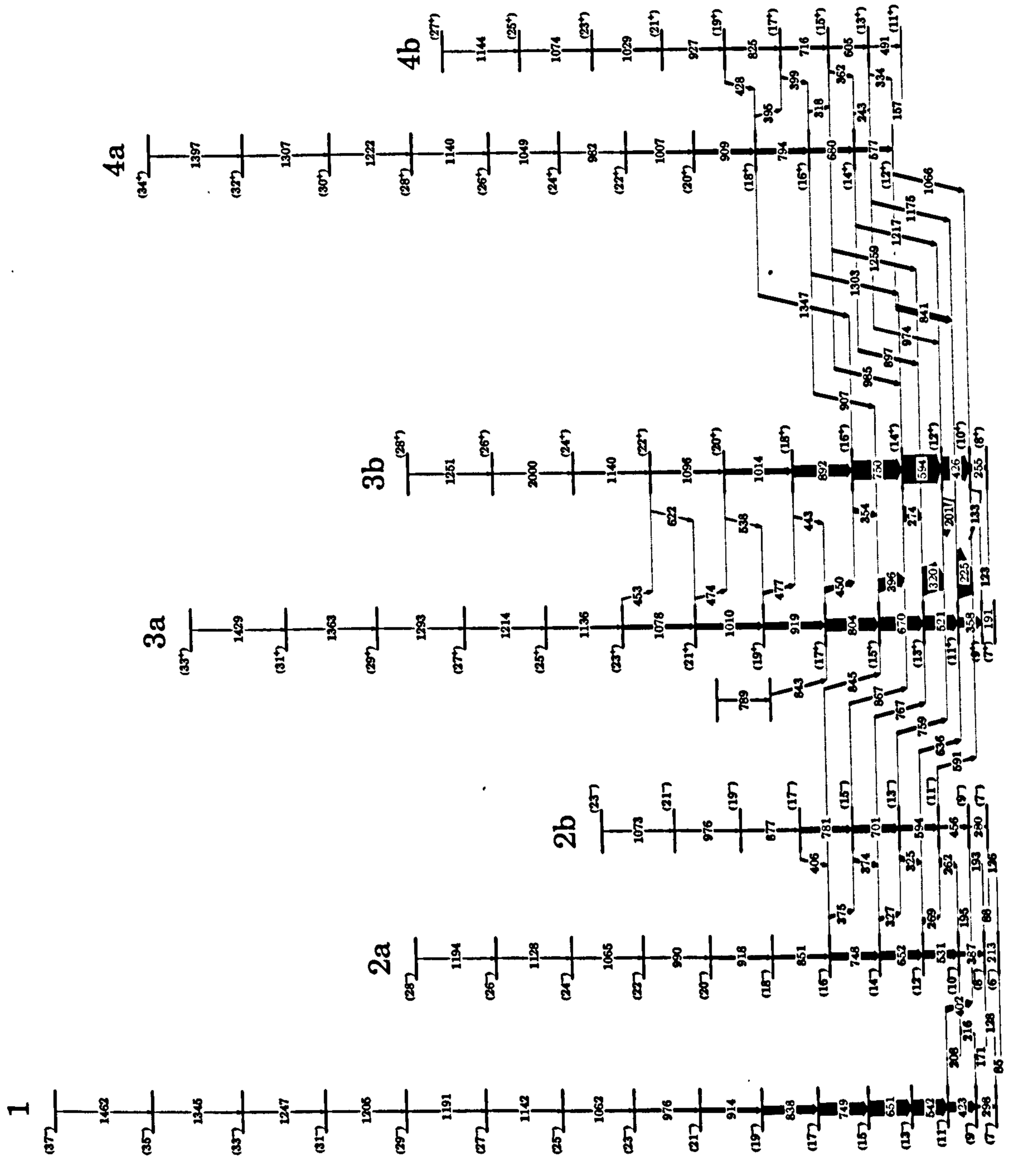

Figure 4.11: Partial level scheme of ^{124}La deduced in this study (also see Fig. 4.12. The transition energies are given in keV and their relative intensities are proportional to the widths of the arrows.

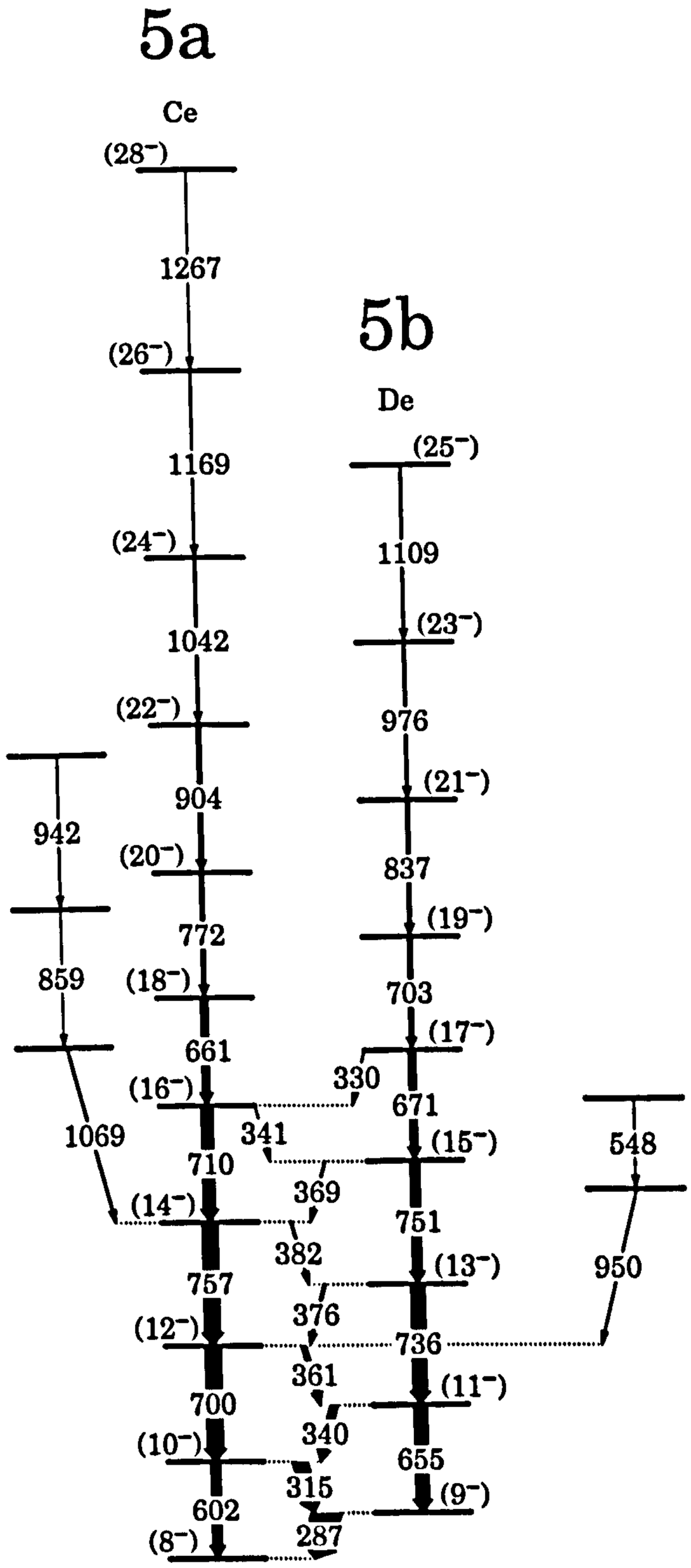

Figure 4.12: Partial level scheme of ^{124}La produced from these studies (also see Fig. 4.11. The transition energies are given in keV and their relative intensities are proportional to the widths of the arrows.

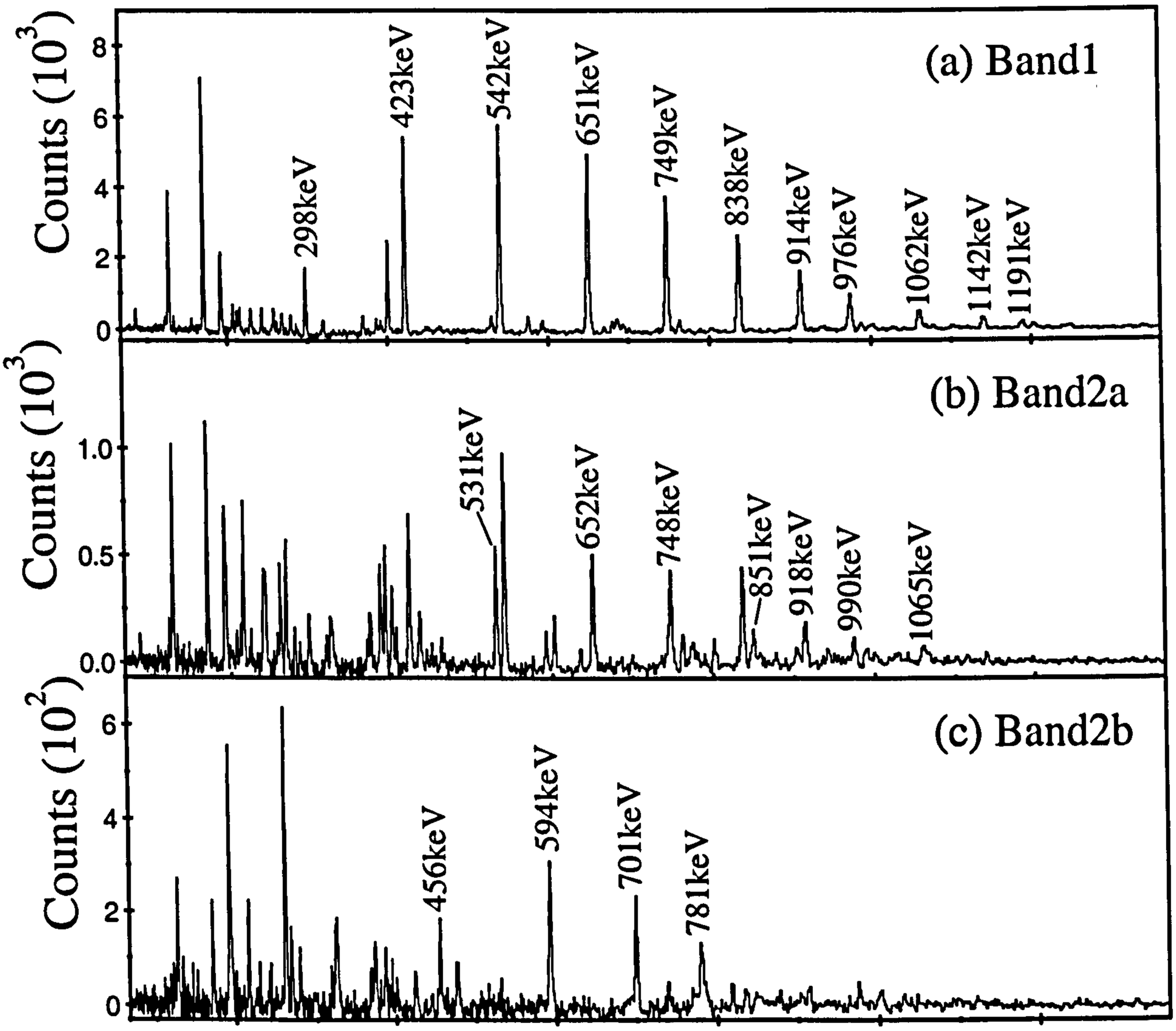

Figure 4.13: Coincidence spectra generated from the sum of double gates on labelled members. (a) shows the main gamma-ray transitions for the decoupled Band 1. (b) and (c) show the main transitions of the two signature partners of Band 2.

4.3.1 Spin and parity assignments

The multipolarity of a gamma ray transition, or by extension the multipole mixing ratio of the transition, can be determined if the angular distribution of the gamma ray is known [Gil75] [Fer65] [Fra65] [Ros67]. Angular distribution measurements have therefore been used, in conjunction with intensity arguments, to determine the multipolarities of transitions within the ^{124}La nucleus. These multipolarities have then been used to assign spins and parities to the observed levels, based upon a spin and parity of $I^{\pi} = 7^{+}$, which is the

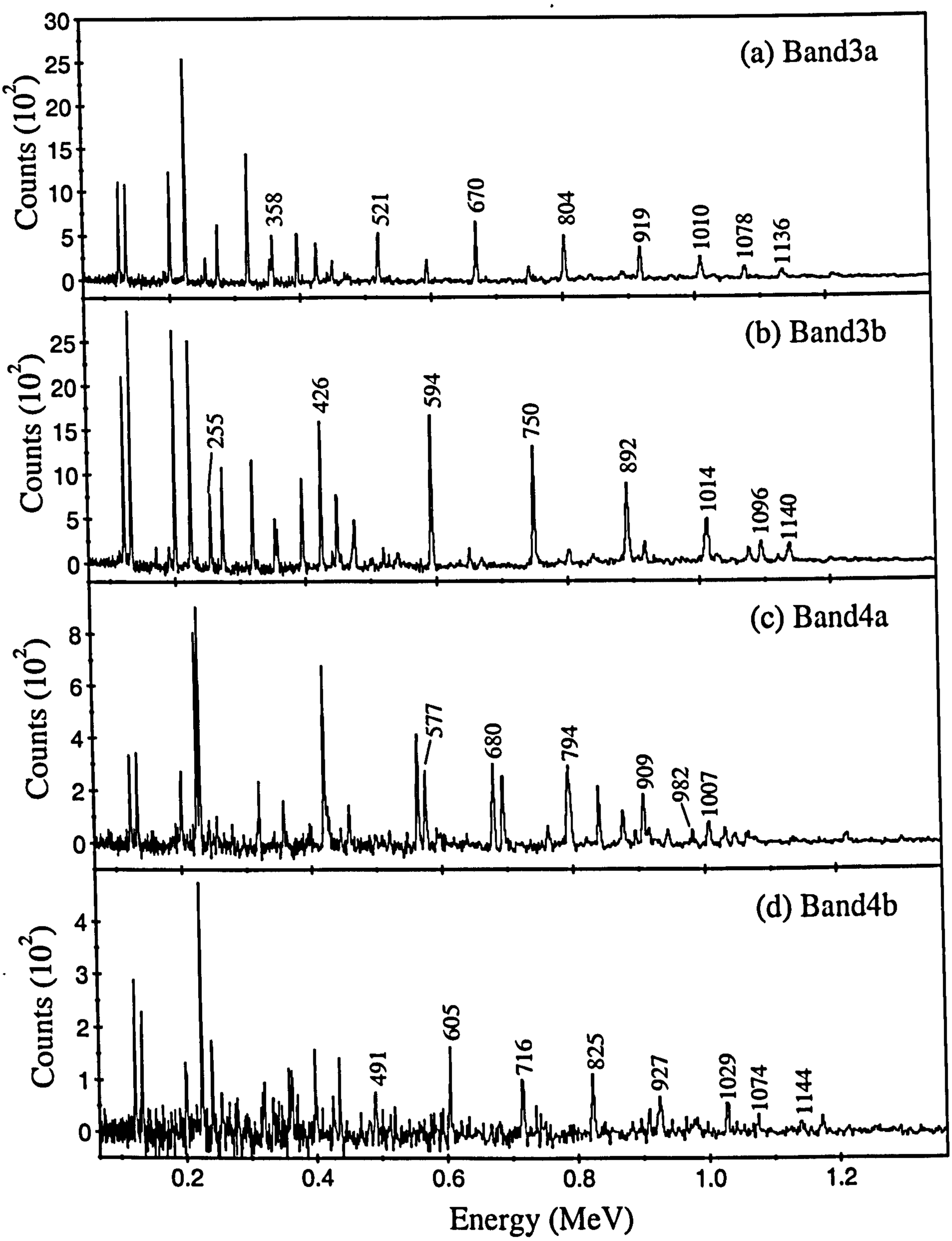

Figure 4.14: Coincidence spectra created from the sum of double gates on the labelled gamma-rays. Spectra (a) and (b) show the main transitions observed for the yrast signature partners of Band 3. Spectra (c) and (d) show the main gamma-ray transitions for the two signature partners of Band 4.

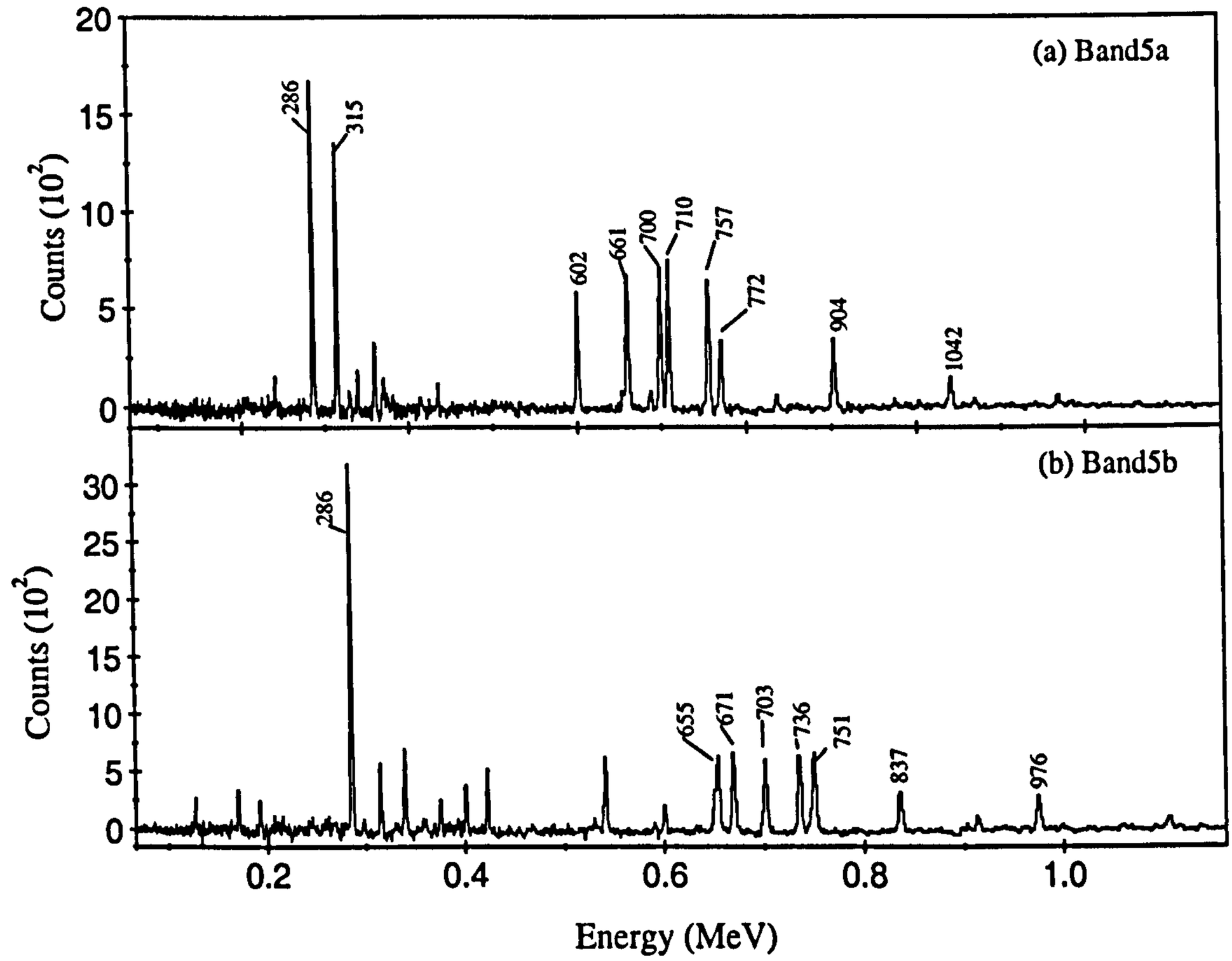

Figure 4.15: Coincidence spectra of the main transitions observed in the signature partners of Band 5, created from the sum of double gates on the labelled members of the Band 5.

lowest energy level of Fig. 4.11. Justification for this assignment will be given in the following chapter. Irrespective of this assumption, the measured multipolarities ensure at the very least that the relative assignments to the observed levels are correct. Gamma-ray intensities were measured as a function of angle by considering the constituent rings of the Gamma-sphere array; after selecting ^{124}La transitions with the ancillary detectors, the gamma-ray data were subsequently projected against ring number, eight rings being used in this analysis. The normalised transition intensities were determined for each ring and were fitted to the standard Legendre expansion of the angular-distribution function [Yam67] [Mat74],

$$W(\theta) = 1 + A_2 P_2(\cos\theta) + A_4 P_4(\cos\theta). \tag{4.3}$$

Empirical A_2 and A_4 angular-distribution coefficients were thus obtained. For some of the weaker transitions, or those with an unphysically large fitted A_4 value, A_4 was set to zero and only a value for A_2 was extracted. A pure stretched dipole transition should display

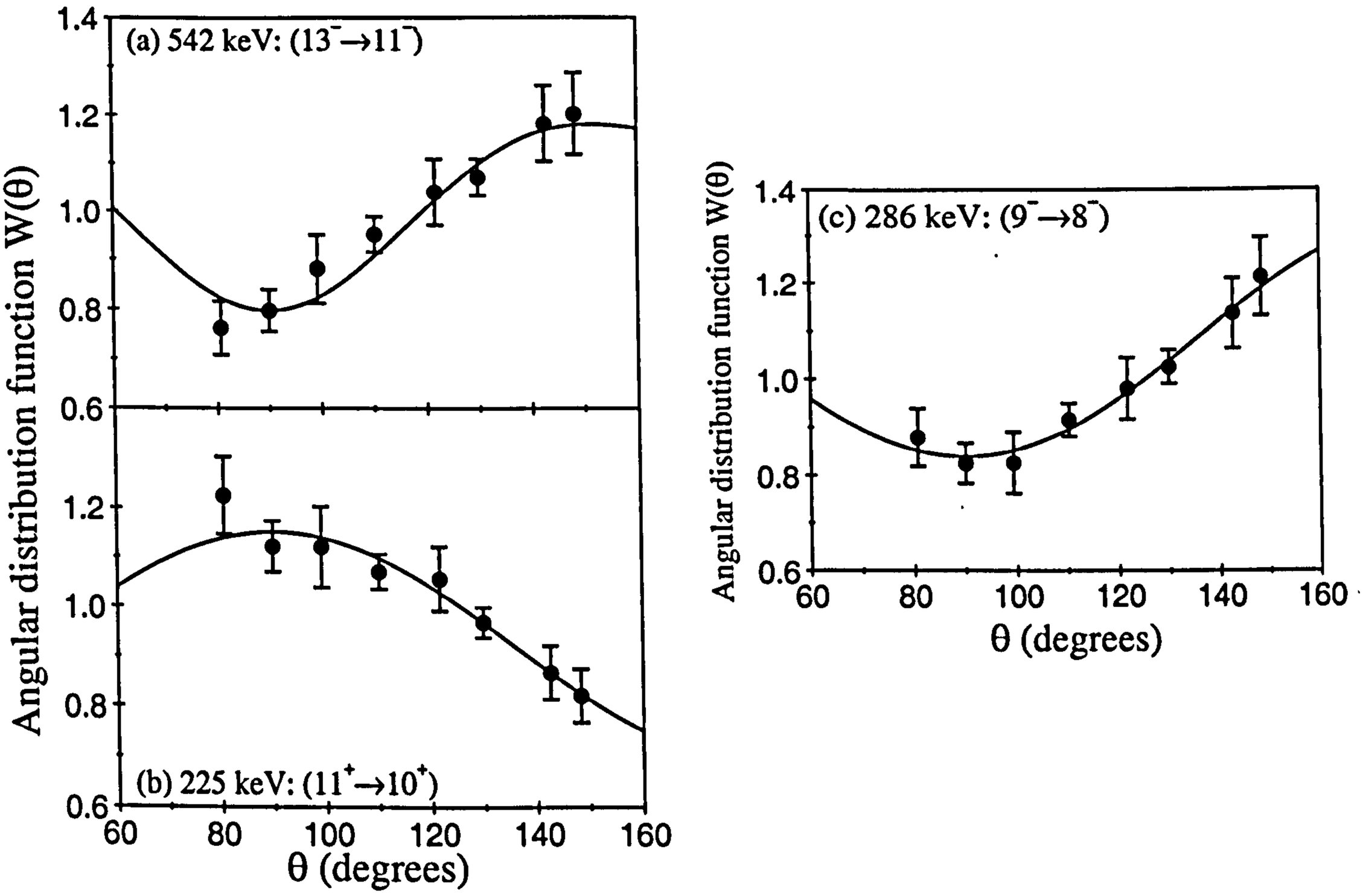

Figure 4.16: Examples of angular distributions. Experimental intensities are shown by the data points, while fitted angular-distribution functions are shown by the curves. (a) and (b) display typical plots for pure quadrupole and dipole transitions, respectively, and plot (c) is an example of a $\Delta I = 1$ transition of mixed $M1/E2$ character ($\delta > 0$).

a distribution with a maximum value of $W(\theta)$ at 90° while a pure stretched quadrupole transition displays a minimum at this angle. Examples of the fitted angular distributions are shown in Fig 4.16, where (a) and (b) display typical plots for pure quadrupole and dipole transitions respectively. Plot (c) is an example of a transition which has a mixture of quadrupole and dipole character. The angular distribution coefficients obtained for some of the more intense transitions were used to extract multipole mixing ratios, δ, by comparing the deduced A_2 and A_4 values to theoretical values [Yam67] [Der74]. The results for bands 2, 3, and 5, using the phase convention of Ref. [Yam67], are included in Tables 4.2, 4.3, 4.4

and 4.5, and 4.7, respectively.

To observe some of the weakest transitions, coincidences between gamma rays must be studied. Therefore, rather than direct angular distribution analysis, measured $\gamma - \gamma$ angular correlation ratios have been used to ascertain multipolarities [Krä89]. The theory of directional correlations of γ-radiation emitted from oriented states (DCO) is well developed, with simplifications of the formulae for $\gamma - \gamma$ angular correlations involving high-spin states proposed [Kra73]. The analysis involves the detection of two gamma rays emitted sequentially in the same cascade as shown in Fig. 4.17. As the transition of interest is

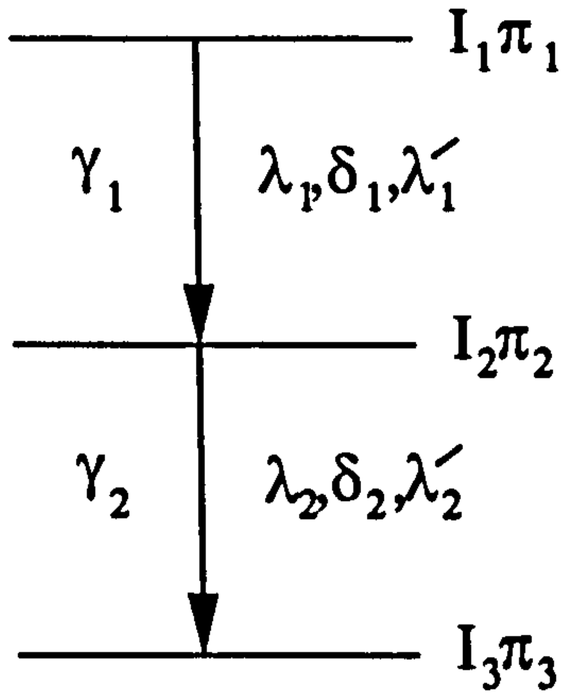

Figure 4.17: Two gamma rays emitted sequentially in the same cascade, showing the spin and parities of the levels, and multipolarities of the gamma-rays.

now observed following another transition, the orientation axis is modified by the latter and is no longer merely the beam direction as in the case of direct angular distributions. The angular distribution function is therefore dependent upon both θ_1 and θ_2. It is strictly also a function of the angle between the gamma rays, $\Delta\phi$, but typical measurements, including those of the present study, are usually taken over all $\Delta\phi$ and so this dependency can be neglected here. An experimentally measured DCO ratio is given by,

$$R_{DCO} = \frac{I^{\gamma_2}_{\theta_1}(Gate^{\gamma_1}_{\theta_2})}{I^{\gamma_2}_{\theta_2}(Gate^{\gamma_1}_{\theta_1})}. \tag{4.4}$$

As forward and backward angles are equivalent in this approach, it is customary to evaluate the ratio for angles as close to 90°, and 0° or 180°, respectively. In the present study, due to the presence of the Neutron Shell, the closest available values were 90°, and 50° or 130°.

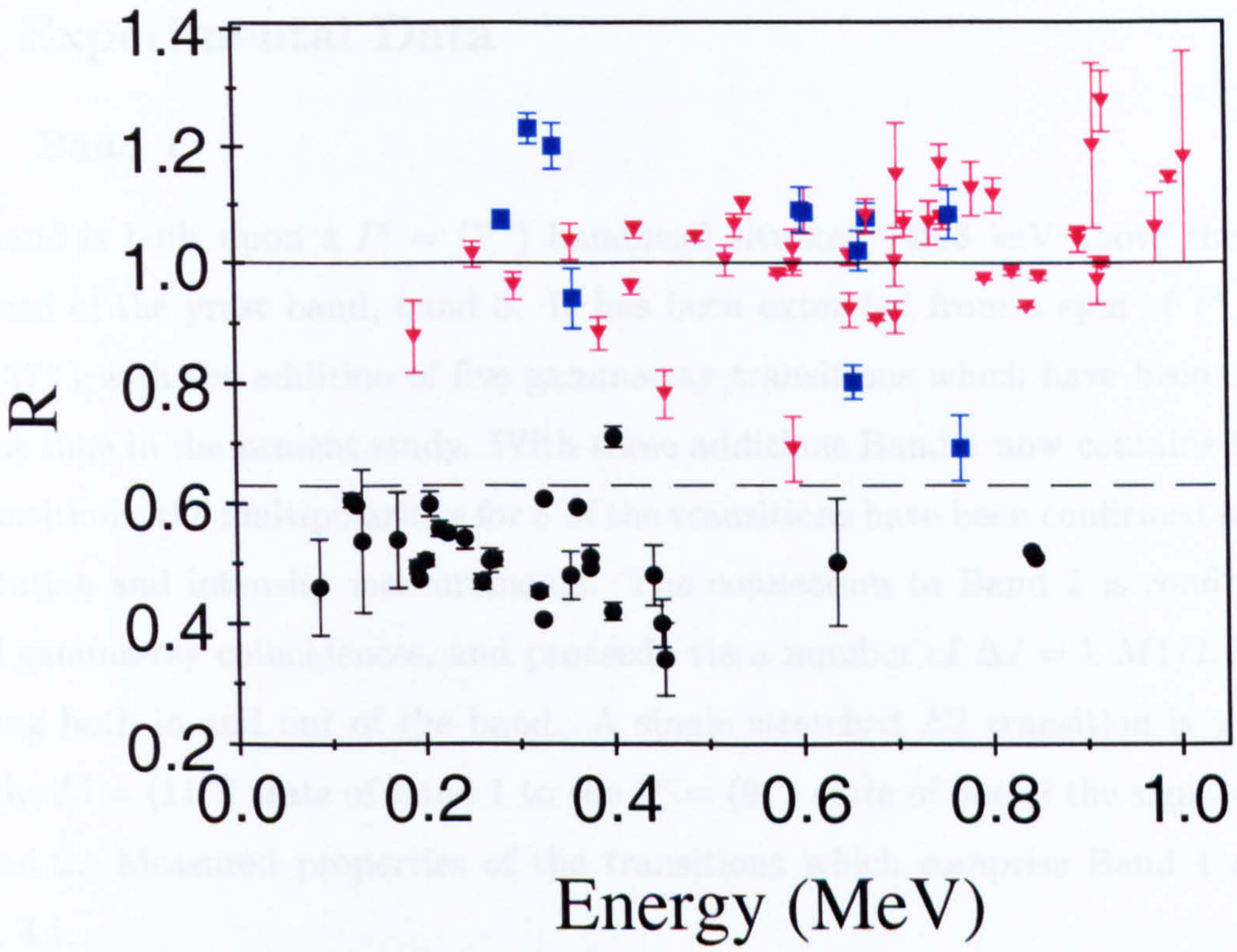

Figure 4.18: A plot of the angular-intensity ratio for gamma-ray transitions in ^{124}La. The solid line shows the theoretical value for pure quadrupole transitions and the dashed line shows the value for a pure dipole transition. The values displayed by squares represent the dipole transitions of Band 5 shown in Fig. 4.12, which have characteristically large angular-intensity ratios.

The measured DCO ratios were therefore evaluated using,

$$R = \frac{I_{\gamma\gamma}(\theta_1 \approx 50°, 130°; \theta_2 \approx 90°)}{I_{\gamma\gamma}(\theta_1 \approx 90°; \theta_2 \approx 50°, 130°)}. \tag{4.5}$$

Here the coincident intensities $I_{\gamma\gamma}$ were measured at an angle θ_1 when gated by quadrupole transitions at an angle θ_2. Ratios were obtained for many transitions but were of particular importance for the weaker transitions where A_2 and A_4 coefficients could not be measured. The results are given in Tables 4.1—4.7 and are displayed in Fig. 4.18. Theoretical values of R, against which experimentally determined values must be compared to obtain multipolarities, are approximately 1.00 and 0.63 for pure stretched quadrupole and pure stretched

dipole transitions respectively.

4.4 Experimental Data

4.4.1 Band 1

This band is built upon a $I^\pi = (7^-)$ bandhead situated 140.3 keV above the $I^\pi = (7^+)$ bandhead of the yrast band, band 3. It has been extended from a spin of $I^\pi = (27^-)$ to $I^\pi = (37^-)$ with the addition of five gamma-ray transitions which have been observed for the first time in the present study. With these additions Band 1 now contains 15 stretched $E2$ transitions; the multipolarities for 8 of the transitions have been confirmed from angular distribution and intensity measurements. The connection to Band 2 is confirmed by observed gamma-ray coincidences, and proceeds via a number of $\Delta I = 1$ $M1/E2$ transitions decaying both in and out of the band. A single stretched $E2$ transition is also observed from the $I^\pi = (11^-)$ state of Band 1 to the $I^\pi = (9^-)$ state of one of the signature partners of Band 2. Measured properties of the transitions which comprise Band 1 are given in Table. 4.1.

4.4.2 Band 2

Built upon a $I^\pi = (6^-)$ bandhead at 54.8 keV, Band 2 comprises two signature partner sequences. The odd-spin partner (Band 2b) has been extended higher in spin from $I^\pi = (17^-)$ to $I^\pi = (23^-)$. This sequence has also been extended lower in spin from $I^\pi = (9^-)$ to $I^\pi = (7^-)$. Six gamma-ray transitions have been added to the even-spin partner (Band 2a), which now extends up to $I^\pi = (28^-)$. Stretched $E1$ transitions which decay out of Band 2 connect it to the yrast band, Band 3. Measured properties of the transitions which comprise Band 2 are given in Tables. 4.2 and 4.3.

4.4.3 Band 3

Band 3 is yrast at low spin. It is constructed from two signature-partner sequences of positive parity connected via $\Delta I = 1$ $M1/E2$ transitions. The $\alpha = 1$, odd-spin partner, has been extended to a maximum observed spin of (33) $\hbar$ with the addition of four newly discovered $E2$ gamma-ray transitions. The $\alpha = 0$, even-spin partner, has been extended

in the current study to a spin of (28) $\hbar$. Angular distribution and intensity methods have confirmed the multipolarities of 25 of the transitions. Details regarding the bandhead assignment of $I^{\pi} = (7^{+})$, upon which almost all other assignments in this nucleus are based, will be given in the following chapter. Measured properties of the transitions which comprise Band 3 are given in Tables. 4.4 and 4.5.

4.4.4 Band 4

Band 4 was established for the first time in the present study. Two signature partners of positive parity are observed with $\Delta I = 1$ transitions connecting them. The bandhead is observed at an excitation energy of 1234.3 keV and is assigned a spin of (11) $\hbar$. The even-spin sequence, Band 4a, contains 11 stretched $E2$ transitions built upon a state with $I^{\pi} = (12^{+})$. The odd-spin sequence comprises eight stretched $E2$ transitions built upon the bandhead. Both sequences decay into the yrast band, via both $\Delta I = 2$ and $\Delta I = 1$ transitions in the former case and $\Delta I = 1$ transitions in the latter. The multipolarity of some linking transitions has been confirmed through gamma-ray coincidence methods as well as angular distribution and intensity measurements. Measured properties of the transitions which comprise Band 4 are given in Table 4.6.

4.4.5 Band 5

This band is somewhat anomalous as no transitions have been observed which link it to the remaining structure. It has been observed for the first time in the current study. However, in structure it is very much like the previously described bands, consisting of two signature partners connected via strong $\Delta I = 1$ transitions. The bandhead is proposed to have a spin of $I^{\pi} = (8^{-})$. The reasoning behind this proposed assignment is given in the following chapter. Measured properties of the transitions which comprise Band 5 are given in Table 4.7.

Table 4.1: Measured properties of the γ-ray transitions assigned to Band 1.

E_γ(keV) [a]	I_γ [b]	A_2	A_4	R	Mult	Assignment
298.0	14.2			0.96(3)	$E2$	$(9^- \rightarrow 7^-)$
423.1	48.2			0.96(2)	$E2$	$(11^- \rightarrow 9^-)$
541.5	75.6	0.223(86)	-0.278(94)	1.10(2)	$E2$	$(13^- \rightarrow 11^-)$
651.1	73.1			1.01(2)	$E2$	$(15^- \rightarrow 13^-)$
749.3	59.2			1.07(2)	$E2$	$(17^- \rightarrow 15^-)$
837.8	38.8			0.93(2)	$E2$	$(19^- \rightarrow 17^-)$
914.1	19.6			0.97(4)	$E2$	$(21^- \rightarrow 19^-)$
975.6	11.5			1.06(6)	$E2$	$(23^- \rightarrow 21^-)$
1061.7	6.4					$(25^- \rightarrow 23^-)$
1141.6	3.9					$(27^- \rightarrow 25^-)$
1190.6	2.9					$(29^- \rightarrow 27^-)$
1204.9	1.6					$(31^- \rightarrow 29^-)$
1246.6	1.3					$(33^- \rightarrow 31^-)$
1345.1	0.7					$(35^- \rightarrow 33^-)$
1462.4	0.1					$(37^- \rightarrow 35^-)$

[a] The γ-ray energies are estimated to be accurate to $\pm$0.3 keV for the strong transitions ($I_\gamma >$ 10), rising to $\pm$0.6 keV for the weaker transitions. Energies quoted as integers have errors $\pm$1 keV.

[b] Errors on the relative intensities are estimated to be less than 5% of the quoted values for strong transitions ($I_\gamma > 10$) and less than 10% for the weaker transitions.

Table 4.2: Measured properties of the γ-ray transitions assigned to Band 2.

E_γ(keV) [a]	I_γ [b]	A_2	A_4	δ	R	Mult	Assignment
87.5	4.5				0.46(8)	$M1/E2$	$(8^- \rightarrow 7^-)$
126.3	10.0				0.55(4)	$M1/E2$	$(7^- \rightarrow 6^-)$
192.5	34.5				0.49(2)	$M1/E2$	$(9^- \rightarrow 8^-)$
194.5	17.8				0.47(2)	$M1/E2$	$(10^- \rightarrow 9^-)$
212.5	5.1						$(8^- \rightarrow 6^-)$
262.0	34.5	-0.139(70)	0.105(84)	0.057(13)	0.47(2)	$M1/E2$	$(11^- \rightarrow 10^-)$
269.3	23.6	-0.565(85)	$\equiv 0$		0.50(2)	$M1/E2$	$(12^- \rightarrow 11^-)$
279.6	5.9						$(9^- \rightarrow 7^-)$
324.7	20.6				0.41(2)	$M1/E2$	$(13^- \rightarrow 12^-)$
326.9	13.3				0.60(2)	$M1/E2$	$(14^- \rightarrow 13^-)$
373.6	15.0				0.51(2)	$M1/E2$	$(15^- \rightarrow 14^-)$
375.2	10.4				0.51(2)	$M1/E2$	$(16- \rightarrow 15^-)$
386.7	19.9				0.88(3)	$E2$	$(10^- \rightarrow 8^-)$
406.1	5.8						$(17^- \rightarrow 16^-)$
456.0	12.3				0.78(4)	$E2$	$(11^- \rightarrow 9^-)$
531.0	35.3				1.06(2)	$E2$	$(12^- \rightarrow 10^-)$
593.9	25.2	0.320(81)	-0.016(86)		0.99(2)	$E2$	$(13^- \rightarrow 11^-)$
651.8	40.0	0.544(66)	$\equiv 0$		0.97(3)	$E2$	$(14^- \rightarrow 12^-)$
700.6	34.7				0.91(3)	$E2$	$(14^- \rightarrow 13^-)$
748.0	33.9				1.17(4)	$E2$	$(15^- \rightarrow 13^-)$
781.2	26.5				1.13(5)	$E2$	$(17^- \rightarrow 15^-)$
851.3	14.5				0.98(5)	$E2$	$(18^- \rightarrow 16^-)$
877.0	7.0				1.63(10)	$E2$	$(19^- \rightarrow 17^-)$
917.7	10.7				1.00(5)	$E2$	$(20^- \rightarrow 18^-)$
976.4	3.8				1.06(6)	$E2$	$(21^- \rightarrow 19^-)$
990.4	4.1				1.14(7)	$E2$	$(22^- \rightarrow 20^-)$

Table 4.3: Measured properties of the γ-ray transitions assigned to Band 2 (cont).

E_γ(keV) [a]	I_γ [b]	A_2	A_4	δ	R	Mult	Assignment
1064.8	3.4						$(24^- \rightarrow 22^-)$
1072.6	1.5						$(23^- \rightarrow 21^-)$
1128.4	1.4						$(26^- \rightarrow 24^-)$
1194.4	0.6						$(28^- \rightarrow 26^-)$

[a] The γ-ray energies are estimated to be accurate to ± 0.3 keV for the strong transitions ($I_\gamma > 10$), rising to ± 0.6 keV for the weaker transitions. Energies quoted as integers have errors ± 1 keV.

[b] Errors on the relative intensities are estimated to be less than 5% of the quoted values for strong transitions ($I_\gamma > 10$) and less than 10% for the weaker transitions.

Table 4.4: Measured properties of the γ-ray transitions assigned to Band 3.

E_γ(keV) [a]	I_γ [b]	A_2	A_4	δ	R	Mult	Assignment
122.6	63.6				0.61(2)	$M1/E2$	$(9^+ \rightarrow 8^+)$
133.2	156.8				0.54(1)	$M1/E2$	$(10^+ \rightarrow 9^+)$
191.4	4.0				0.88(6)	$E2$	$(9^+ \rightarrow 7^+)$
200.9	148.8	-0.306(60)	0.049(77)	-0.050(12)	0.51(1)	$M1/E2$	$(12^+ \rightarrow 11^+)$
225.0	200.5	-0.286(61)	0.081(77)	-0.035(13)	0.55(1)	$M1/E2$	$(11^+ \rightarrow 10^+)$
255.4	35.6	0.236(79)	-0.053(95)		1.01(3)	$E2$	$(10^+ \rightarrow 8^+)$
274.1	61.6	-0.346(60)	0.081(77)	-0.079(15)	0.51(2)	$M1/E2$	$(14^+ \rightarrow 13^+)$
319.9	121.4	-0.401(58)	0.069(75)	-0.113(20)	0.45(1)	$M1/E2$	$(13^+ \rightarrow 12^+)$
354.1	19.2	-0.790(66)	0.094(94)	-0.751(120)	0.48(4)	$M1/E2$	$(16^+ \rightarrow 15^+)$
357.9	42.5	0.226(84)	-0.019(94)		1.04(3)	$E2$	$(10^+ \rightarrow 9^+)$
396.3	57.4	-0.363(60)	0.075(77)	-0.091(13)	0.42(2)	$M1/E2$	$(15^+ \rightarrow 14^+)$
425.6	110.5	0.225(79)	-0.129(86)		1.06(2)	$E2$	$(12^+ \rightarrow 10^+)$
442.8	4.2				0.48(5)	$M1/E2$	$(18^+ \rightarrow 17^+)$
449.9	23.3	-0.342(60)	$\equiv 0$		0.40(4)	$M1/E2$	$(17^+ \rightarrow 16^+)$

Table 4.5: Measured properties of the γ-ray transitions assigned to Band 3 (cont).

E_γ(keV) [a]	I_γ [b]	A_2	A_4	δ	R	Mult	Assignment
453.4	0.7				0.34(6)	$M1/E2$	$(23^+ \rightarrow 22^+)$
473.5	2.9						$(21^+ \rightarrow 20^+)$
476.6	8.1						$(19^+ \rightarrow 18^+)$
520.6	65.2	0.519(48)	$\equiv 0$		1.00(3)	$E2$	$(13^+ \rightarrow 11^+)$
537.9	1.4						$(20^+ \rightarrow 19^+)$
593.8	135.1	0.301(81)	-0.028(84)		1.02(4)	$E2$	$(14^+ \rightarrow 12^+)$
622.2	0.7						$(22^+ \rightarrow 21^+)$
670.2	63.4	0.339(81)	-0.068(85)		1.08(3)	$E2$	$(15^+ \rightarrow 13^+)$
750.3	91.4	0.416(84)	0.080(88)		1.08(2)	$E2$	$(16^+ \rightarrow 14^+)$
803.8	56.0	0.403(91)	-0.156(96)		1.12(3)	$E2$	$(17^+ \rightarrow 15^+)$
892.3	54.2	0.356(95)	-0.202(10)		1.05(4)	$E2$	$(18^+ \rightarrow 16^+)$
919.0	32.5	0.409(86)	0.002(90)		1.27(6)	$E2$	$(19^+ \rightarrow 17^+)$
1010.0	27.2				1.02(7)	$E2$	$(21^+ \rightarrow 19^+)$
1013.9	25.1				0.86(6)	$E2$	$(20^+ \rightarrow 18^+)$
1077.5	17.2						$(23^+ \rightarrow 21^+)$
1096.1	10.9				1.01(11)	$E2$	$(22^+ \rightarrow 20^+)$
1135.6	6.5						$(25^+ \rightarrow 23^+)$
1140.0	6.5						$(24^+ \rightarrow 22^+)$
1199.9	1.4						$(26^+ \rightarrow 24^+)$
1213.6	3.3						$(27^+ \rightarrow 25^+)$
1251.4	1.6						$(28^+ \rightarrow 26^+)$
1293.3	1.1						$(29^+ \rightarrow 27^+)$
1363.0	0.9						$(31^+ \rightarrow 29^+)$
1429.3	0.2						$(33^+ \rightarrow 31^+)$

[a] The γ-ray energies are estimated to be accurate to ± 0.3 keV for the strong transitions ($I_\gamma > 10$), rising to ± 0.6 keV for the weaker transitions. Energies quoted as integers have errors ± 1 keV.

[b] Errors on the relative intensities are estimated to be less than 5% of the quoted values for strong transitions ($I_\gamma > 10$) and less than 10% for the weaker transitions.

Table 4.6: Measured properties of the γ-ray transitions assigned to Band 4.

E_γ(keV) [a]	I_γ [b]	A_2	A_4	R	Mult	Assignment
157.1	1.2					$(12^+ \rightarrow 11^+)$
242.6	6.4			0.54(2)	$M1/E2$	$(14^+ \rightarrow 13^+)$
318.0	6.2					$(16^+ \rightarrow 15^+)$
334.0	3.9					$(13^+ \rightarrow 12^+)$
362.4	7.0			0.59(3)	$M1/E2$	$(15^+ \rightarrow 14^+)$
394.7	4.7					$(18^+ \rightarrow 17^+)$
398.6	6.8					$(17^+ \rightarrow 16^+)$
427.9	8.0					$(19^+ \rightarrow 18^+)$
490.7	3.9			1.04(6)	$E2$	$(13^+ \rightarrow 11^+)$
576.9	18.3	0.297(81)	-0.028(85)	0.98(2)	$E2$	$(14^+ \rightarrow 12^+)$
605.4	11.5			1.09(4)	$E2$	$(15^+ \rightarrow 13^+)$
680.3	23.6	0.431(71)	$\equiv 0$	0.90(2)	$E2$	$(16^+ \rightarrow 14^+)$
716.1	13.9					$(17^+ \rightarrow 15^+)$
794.2	24.6			0.97(2)	$E2$	$(18^+ \rightarrow 16^+)$
824.7	11.5					$(19^+ \rightarrow 17^+)$
909.2	22.7			1.20(14)	$E2$	$(20^+ \rightarrow 18^+)$
926.8	8.4					$(21^+ \rightarrow 19^+)$
982.2	1.5					$(24^+ \rightarrow 22^+)$
1006.9	11.2			1.18(18)	$E2$	$(22^+ \rightarrow 20^+)$
1029.1	10.6					$(23^+ \rightarrow 21^+)$
1049.2	2.5					$(26^+ \rightarrow 24^+)$
1074.4	3.4					$(25^+ \rightarrow 23^+)$
1140.1	2.3					$(28^+ \rightarrow 26^+)$
1143.8	1.7					$(27^+ \rightarrow 25^+)$
1221.8	2.2					$(30^+ \rightarrow 28^+)$
1307.2	1.3					$(32^+ \rightarrow 30^+)$
1397.0	0.9					$(34^+ \rightarrow 32^+)$

[a] The γ-ray energies are estimated to be accurate to ± 0.3 keV for the strong transitions ($I_\gamma >$ 10), rising to ± 0.6 keV for the weaker transitions. Energies quoted as integers have errors ± 1 keV.

[b] Errors on the relative intensities are estimated to be less than 5% of the quoted values for strong transitions ($I_\gamma > 10$) and less than 10% for the weaker transitions.

Table 4.7: Measured properties of the γ-ray transitions assigned to Band 5.

E_γ(keV) [a]	I_γ [b]	A_2	A_4	δ	R	Mult	Assignment
286.5	60	0.309(99)	0.135(120)	0.37(16)	1.07(2)	$M1/E2$	$(9^- \rightarrow 8^-)$
315.3	31.7	0.116(87)	-0.037(81)	0.22(6)	1.23(3)	$M1/E2$	$(10^- \rightarrow 9^-)$
329.8	1.5						$(17^- \rightarrow 16^-)$
340.0	16.6			1.20(4)		$M1/E2$	$(11^- \rightarrow 10^-)$
341.3	1.3						$(16^- \rightarrow 15^-)$
360.5	11.4			0.94(5)		$M1/E2$	$(12^- \rightarrow 11^-)$
369.3	2.6						$(15^- \rightarrow 14^-)$
375.8	5.5						$(13^- \rightarrow 12^-)$
381.6	3.5						$(14^- \rightarrow 13^-)$
601.6	20.9			1.09(4)		$E2$	$(10^- \rightarrow 8^-)$
655.2	29.6			0.80(3)		$E2$	$(11^- \rightarrow 9^-)$
661.4	16.3			1.02(4)		$E2$	$(18^- \rightarrow 16^-)$
670.7	16.5			1.07(3)		$E2$	$(17^- \rightarrow 15^-)$
700.4	35.1			1.00(4)		$E2$	$(12^- \rightarrow 10^-)$
702.5	10.3			1.15(8)		$E2$	$(19^- \rightarrow 17^-)$
710.1	26.2			1.07(2)		$E2$	$(16^- \rightarrow 14^-)$
736.3	31.2			1.07(4)		$E2$	$(13^- \rightarrow 11^-)$
751.4	22.1			1.08(3)		$E2$	$(15^- \rightarrow 13^-)$
757.4	33.4			1.08(5)		$E2$	$(14^- \rightarrow 12^-)$
772.1	8.6						$(20^- \rightarrow 18^-)$
836.7	7.9						$(21^- \rightarrow 19^-)$
904.4	9.3						$(22^- \rightarrow 20^-)$
976.2	5.3						$(23^- \rightarrow 21^-)$
1041.6	4.8						$(24^- \rightarrow 22^-)$
1109.3	3.5						$(25^- \rightarrow 23^-)$
1168.6	2.6						$(26^- \rightarrow 24^-)$
1266.8	0.9						$(28^- \rightarrow 26^-)$

[a] The γ-ray energies are estimated to be accurate to ± 0.3 keV for the strong transitions ($I_\gamma > 10$), rising to ± 0.6 keV for the weaker transitions. Energies quoted as integers have errors ± 1 keV.

[b] Errors on the relative intensities are estimated to be less than 5% of the quoted values for strong transitions ($I_\gamma > 10$) and less than 10% for the weaker transitions.

Table 4.8: Measured properties of the interband transitions.

Linking Transitions								
Transition	E_γ(keV) [a]	I_γ [b]	A_2/A_0	A_4/A_0	δ	R	Mult.	Assignment
$1 \rightarrow 2a$	85.4	10.0						$(7^- \rightarrow 6^-)$
$2a \rightarrow 1$	127.6	32.8				0.598(2)	$M1/E2$	$(8^- \rightarrow 7^-)$
$1 \rightarrow 2a$	171.0	53.8				0.539(8)	$M1/E2$	$(9^- \rightarrow 8^-)$
$1 \rightarrow 2a$	207.5	5.3				0.599(21)	$M1/E2$	$(11^- \rightarrow 10^-)$
$2a \rightarrow 1$	215.9	26.0				0.558(13)	$M1/E2$	$(10^- \rightarrow 9^-)$
$1 \rightarrow 2b$	401.7	22.8				0.711(17)	$E2$	$(11^- \rightarrow 9^-)$
$2b \rightarrow 3b$	591.3	5.6				0.690(54)	$E1$	$(11^- \rightarrow 10^+)$
$2a \rightarrow 3a$	636.4	10.4				0.502(106)	$E1$	$(12^- \rightarrow 11^+)$
$2b \rightarrow 3b$	758.8	12.9				0.637(79)	$E1$	$(13^- \rightarrow 12^+)$
$2a \rightarrow 3a$	767.1	9.4				0.692(54)	$E1$	$(14^- \rightarrow 13^+)$
$4a \rightarrow 3a$	840.9	26.9	0.194(100)	0.108(110)	0.28(10)	0.520(1)	$M1/E2$	$(12^+ \rightarrow 11^+)$
$2a \rightarrow 3a$	845.4	7.5				0.509(3)	$E1$	$(16^- \rightarrow 15^+)$
$2b \rightarrow 3b$	867.3	8.0						$(15^- \rightarrow 14^+)$
$4a \rightarrow 3a$	896.7	12.5						$(14^+ \rightarrow 13^+)$
$4a \rightarrow 3a$	907.1	7.0						$(16^+ \rightarrow 15^+)$
$4b \rightarrow 3b$	974.3	21.5	-0.089(54)	$\equiv 0$	0.085(30)			$(13^+ \rightarrow 12^+)$
$4b \rightarrow 3b$	985.4	9.1						$(15^+ \rightarrow 14^+)$
$4a \rightarrow 3b$	1065.8	4.7						$(12^+ \rightarrow 10^+)$
$4b \rightarrow 3a$	1175.0	5.4						$(13^+ \rightarrow 11^+)$
$4a \rightarrow 3b$	1216.9	6.8						$(14^+ \rightarrow 12^+)$
$4b \rightarrow 3a$	1259.4	3.1						$(15^+ \rightarrow 13^+)$
$4a \rightarrow 3b$	1303.4	4.0						$(16^+ \rightarrow 14^+)$
$4a \rightarrow 3b$	1347.3	2.5						$(18^+ \rightarrow 16^+)$

[a] The γ-ray energies are estimated to be accurate to ± 0.3 keV for the strong transitions ($I_\gamma > 10$), rising to ± 0.6 keV for the weaker transitions. Energies quoted as integers have errors ± 1 keV.

[b] Errors on the relative intensities are estimated to be less than 5% of the quoted values for strong transitions ($I_\gamma > 10$) and less than 10% for the weaker transitions.

Chapter 5

Discussion

Within this chapter an interpretation of the results presented previously will be given. The nuclear properties and characteristics of ^{124}La, specifically the signature inversion observed in bands 3 and 4, are discussed and some perspective is given with mention of the behaviour of the surrounding isotopes and isotones in the rare-earth region.

5.1 Spin and Parity assignments

Nordheim [Nor50] was the first to suggest that the ground state spins of odd-odd nuclei can be accounted for on the basis of the $j-j$ coupling model, with the assumption that the intrinsic spins of the unpaired proton and neutron will always tend to line up parallel. However, while this method has validity for a surprising number of nuclei, effects of the correlations between particles outside of closed shells are seen to be extremely important. An improvement of this model was therefore proposed by Gallagher and Moszkowski [Gal58] who used a similar basis as Nordheim, whilst incorporating the deformation of the nucleus. With the introduction of a quantisation axis, the $j-j$ coupling proposed by Nordheim is subsequently modified. It is now assumed that merely the components of the nucleon spins along the symmetry axis, Σ_p and Σ_n, are coupled parallel. If the deformation is sufficiently large then the orbital angular momentum projection Λ, and the spin angular momentum projection Σ, of each single-particle state are good quantum numbers. The separation of Ω into Λ and Σ is still therefore expected to have approximate validity and the following

rules are thus established:

$$I = \Omega_p + \Omega_n \quad \text{if} \quad \Omega_p = \Lambda_p \pm \frac{1}{2} \quad \text{and} \quad \Omega_n = \Lambda_n \pm \frac{1}{2}, \tag{5.1}$$
$$I = |\Omega_p - \Omega_n| \quad \text{if} \quad \Omega_p = \Lambda_p \pm \frac{1}{2} \quad \text{and} \quad \Omega_n = \Lambda_n \mp \frac{1}{2}.$$

The low-spin yrast configuration of ^{124}La is $\pi h_{11/2} \otimes \nu h_{11/2}$ and comprises the proton orbital [550]$1/2^-$ and the neutron orbital [523]$7/2^-$. Therefore, the former of the Gallagher and Moszkowski rules applies and the bandhead of the yrast sequence should possess a spin of $4\hbar$. However, as revealed in Fig. 4.11, the bandhead of the ^{124}La yrast sequence is assigned $I = 7\hbar$ in the present work. This assignment is based upon comparisons between the observed level energies and those predicted by the core-quasiparticle coupling model and is also consistent with systematic trends among neighbouring nuclei. It is believed that spin states of $4\hbar$, $5\hbar$ and $6\hbar$ are present in the ^{124}La decay scheme, but are not observed in the present experiment due to the prohibitively low energies of the gamma-ray transitions which feed and depopulate them. As discussed in section. 4.3.1, all the spin and parity assignments proposed in the present study have been inferred from angular distribution and intensity measurements, relative to the yrast bandhead. This assignment is therefore of paramount importance.

5.1.1 Comparison to the Core-Quasiparticle Coupling Model

The original core-particle-hole coupling model was devised in order to investigate the properties of the $\pi h_{11/2} \otimes \nu h_{11/2}$ doublet bands in odd-odd ^{132}La, where a good agreement between experiment and theory was observed [Sta97] [Mor98] [Sta02].

The core-quasiparticle model [Dia94] [Dön79] [Dro80] is based upon the consecutive coupling of valence particles to an even-even core. The first valence proton (neutron) is coupled to the core resulting in an odd-A system, this odd-proton (neutron) nucleus is then taken as a core, and the subsequent coupling of a neutron (proton) yields an odd-odd system which can be used to predict level energies and electromagnetic properties. In this way the pairing interactions in this region can be dealt with conveniently. Additionally, this model is based within a laboratory reference frame, enabling the total angular momentum of the system to remain a good quantum number. This allows the calculated observables to be directly related to those measured.

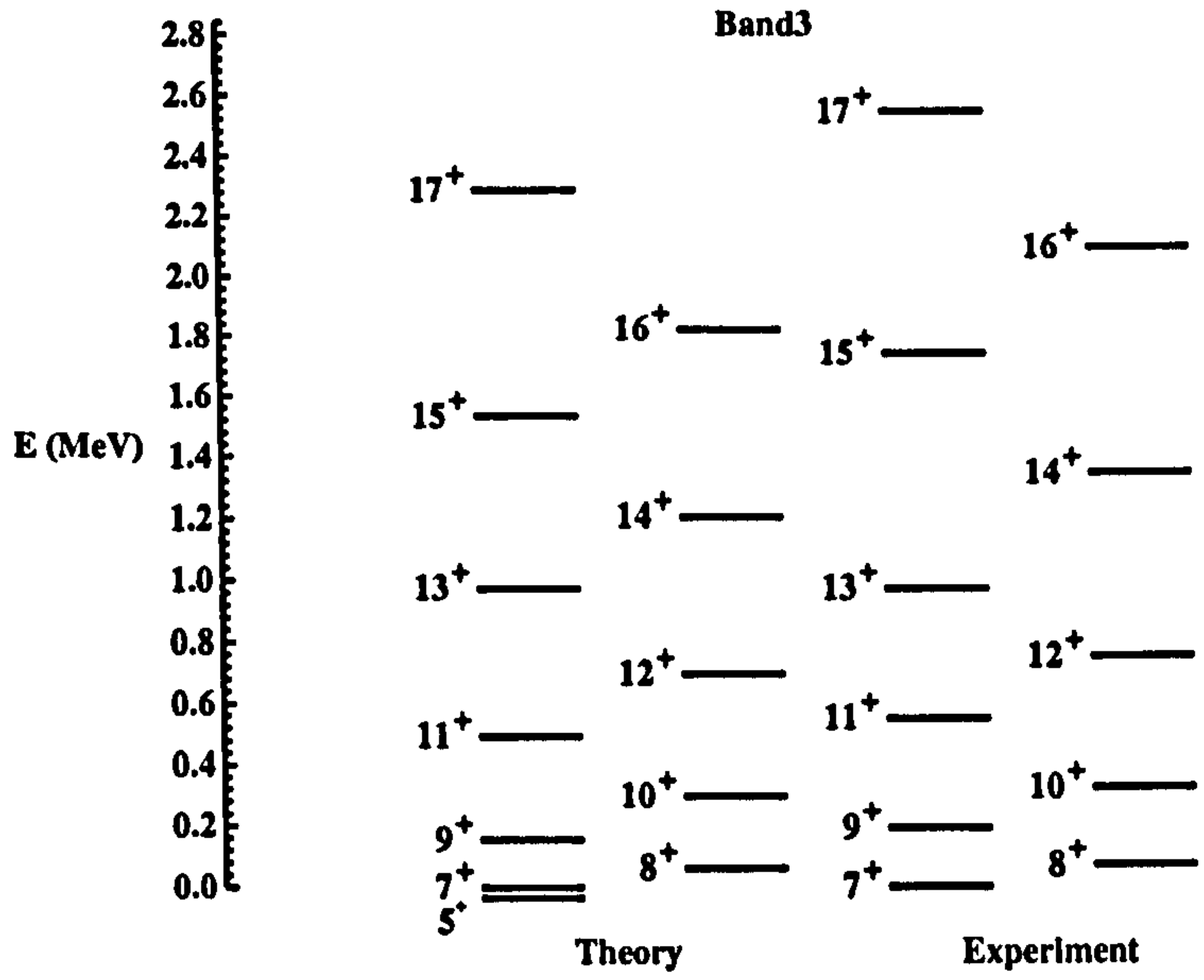

Figure 5.1: Comparison of the energy levels of band 3 in ^{124}La with results of the CQPC model for the first $\pi h_{11/2} \otimes \nu h_{11/2}$ configuration. Theory suggests a spin of $5\hbar$ for the lowest experimental state of band 3.

The Hamiltonian is composed of a spherically symmetric mean field with monopole pairing and separable two body quadrupole-quadrupole interactions:

$$H = \sum_{\tau\alpha} \epsilon_{\tau\alpha} \alpha^{\dagger}_{\tau\alpha} \alpha_{\tau,\alpha} - \frac{1}{2} \sum_{\tau} G_{\tau} P^{\dagger}(\tau) P(\tau) - \frac{1}{2} \sum_{\tau,\tau'} \chi_{\tau\tau'} \sum_{m} Q^{\dagger}_{m}(\tau) Q_{m}(\tau'), \qquad (5.2)$$

where G_τ denotes the strength of the pairing term and is dependent on the spatial overlap of the two nucleons, and $\epsilon_{\tau\alpha}$ denotes the eigen energy for the single-particle state $|\alpha\rangle$, which is represented by a set of the quantum numbers $(j_\alpha, m_\alpha, n_\alpha, l_\alpha)$, with the indices τ and $\tau\prime$ running over both the protons and neutrons. The two indices are required to give the two-body quadrupole interaction term but only one index is required for pairing, as the neutron-proton pairing interaction is not considered here. The monopole pairing is expressed by the operator $P(\tau)$, which annihilates a pair of protons or neutrons in a single-particle state with opposite orientation of angular momentum, and is defined as:

$$P(\tau) = \sum_{\tau\alpha} \tilde{a}_{\tau\alpha} a_{\tau\alpha}. \qquad (5.3)$$

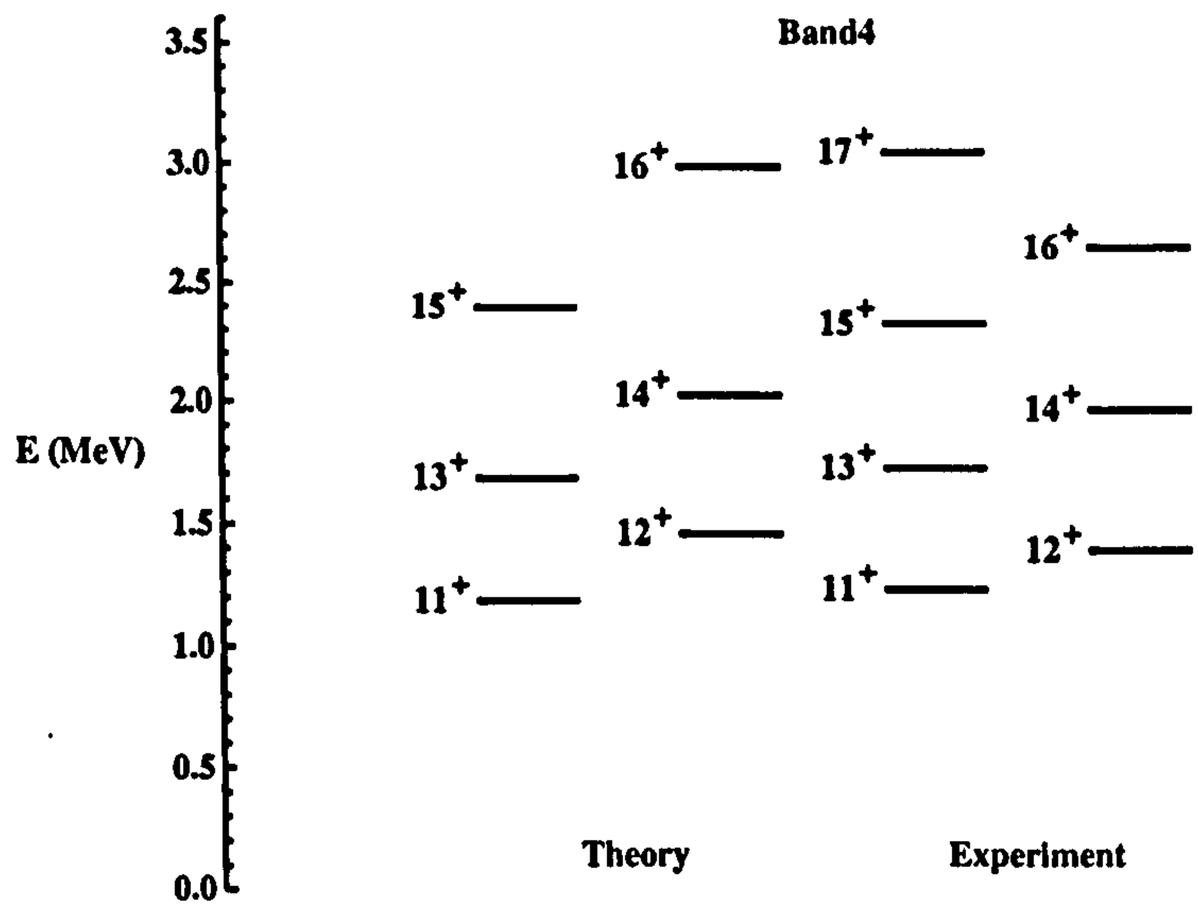

Figure 5.2: Comparison of the energy levels of band 4 in ^{124}La with results of the CQPC model for the second $\pi h_{11/2} \otimes \nu h_{11/2}$ configuration.

The quadrupole operator of protons or neutrons, $Q_m(\tau)$ is given by,

$$Q_m(\tau) = \frac{1}{\sqrt{5}} \sum_{\sigma_{\tau\alpha},\sigma_{\tau\alpha'}} q(\sigma_{\tau\alpha},\sigma_{\tau\alpha'})[a^{\dagger}_{\tau\alpha}\tilde{a}_{\tau\alpha'}]_{2m}, \tag{5.4}$$

where $\sigma_{\tau\alpha} = (j_\alpha, n_\alpha, l_\alpha)$ denotes the set of quantum numbers for the single particle states $|\alpha\rangle$, without the magnetic quantum number m_α, for $\tau = \pi$ or $\tau = \nu$. The reduced matrix element of the single-particle quadrupole operator calculated between the states $|\alpha\rangle$ and $|\alpha'\rangle$ is defined as $q(\sigma_{\tau\alpha},\sigma_{\tau\alpha'})$.

The calculated results of the CQPM for ^{124}La [Koi01] are compared to the experimental level energies for both the yrast and excited $\pi h_{11/2} \otimes \nu h_{11/2}$ signature partner bands, and are shown in Figs. 5.1 and 5.2. In both cases the agreement is seen to be excellent.

5.2 Standard Total Routhian Surface Calculations

The addition of pairing and rotation to the Strutinski shell correction procedure (Section. 1.4) produces an approach known as the total Routhian surface (TRS) method [Naz87] [Naz89] [Wys90] [Sat91], where the deformation and energies of particular configurations can be predicted for fixed values of rotational frequency. At an absolute minimum of the Routhian,

at a fixed rotational frequency, there will be an energetically favoured configuration and nuclear shape. An example of a calculated total Routhian surface, which has been constructed for the ^{124}La nucleus is shown in Fig. 5.3. This TRS plot displays a minimum at $\gamma = 0.0°$, indicating a prolate shape. Average deformation parameters $\beta_2 = 0.275$, and $\beta_4 = 0.0$, are also determined. The ^{124}La nucleus is a prospective candidate for chirality, which is thought to be an indicator of the triaxiality of the nuclear shape. However, the prolate shape that has been determined from TRS calculations contradicts this prediction and dismisses this nucleus to possess the chiral twin bands seen in ^{132}La [Sta02]. Fig. 4.11 shows Band 3 and Band 4 (both built on a $\pi h_{11/2} \otimes \nu h_{11/2}$ configuration) with an average difference of $\sim$ 600 keV between levels of the same spin and parity in each band. Had chirality been apparent in this nucleus, these levels would be almost degenerate.

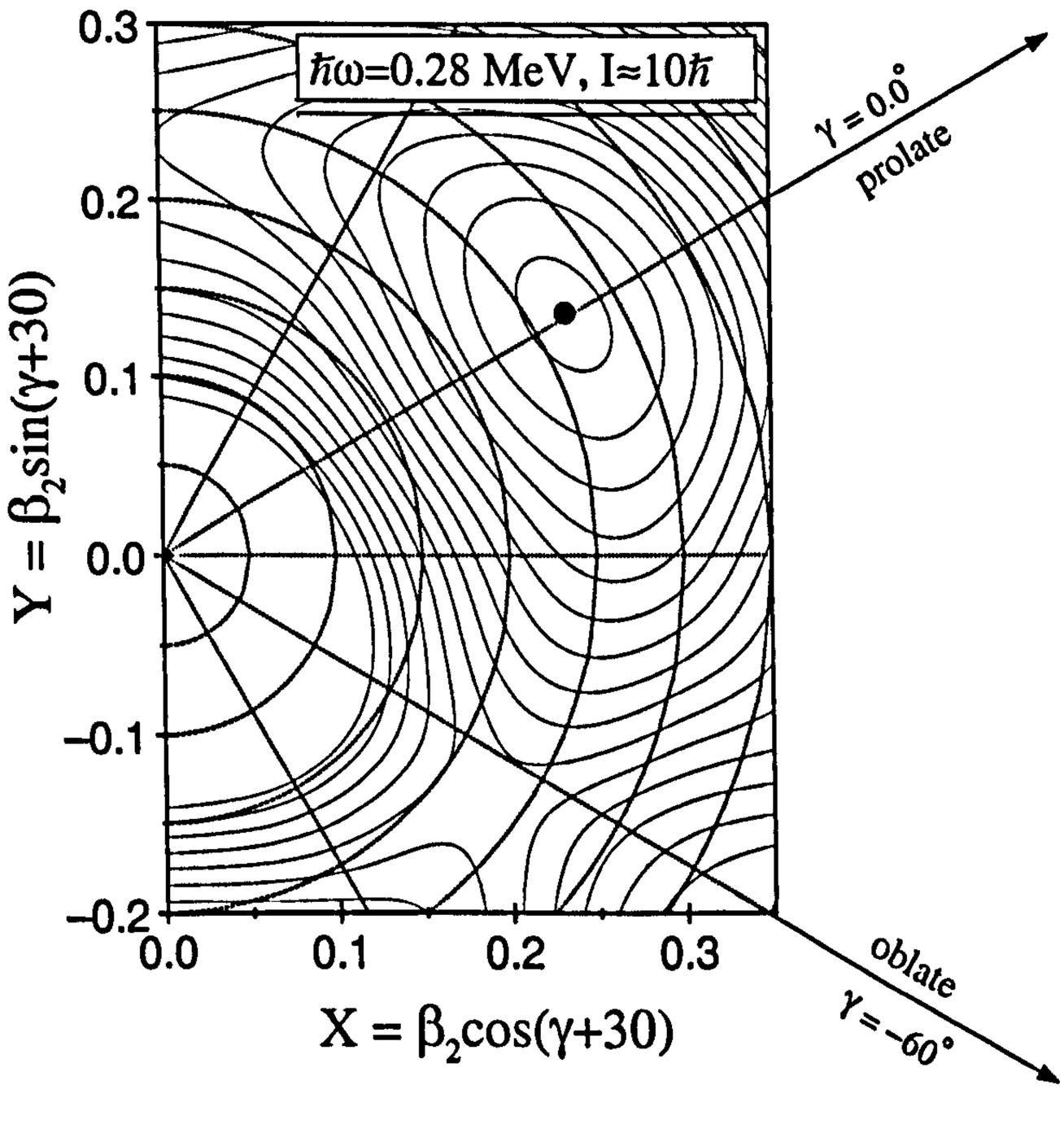

Figure 5.3: TRS calculation for the lowest configuration in ^{124}La. An energy minimum at $\gamma = 0.0°$ can be seen, thus predicting a prolate shape for the nucleus.

5.3 Cranked Woods-Saxon Calculations

The results of cranked Woods-Saxon calculations performed for ^{124}La are shown in Fig. 5.4. These results were produced by employing a Woods-Saxon single-particle potential [Naz85] [Cwi87]. The pairing strength has been calculated at zero rotational frequency, and is

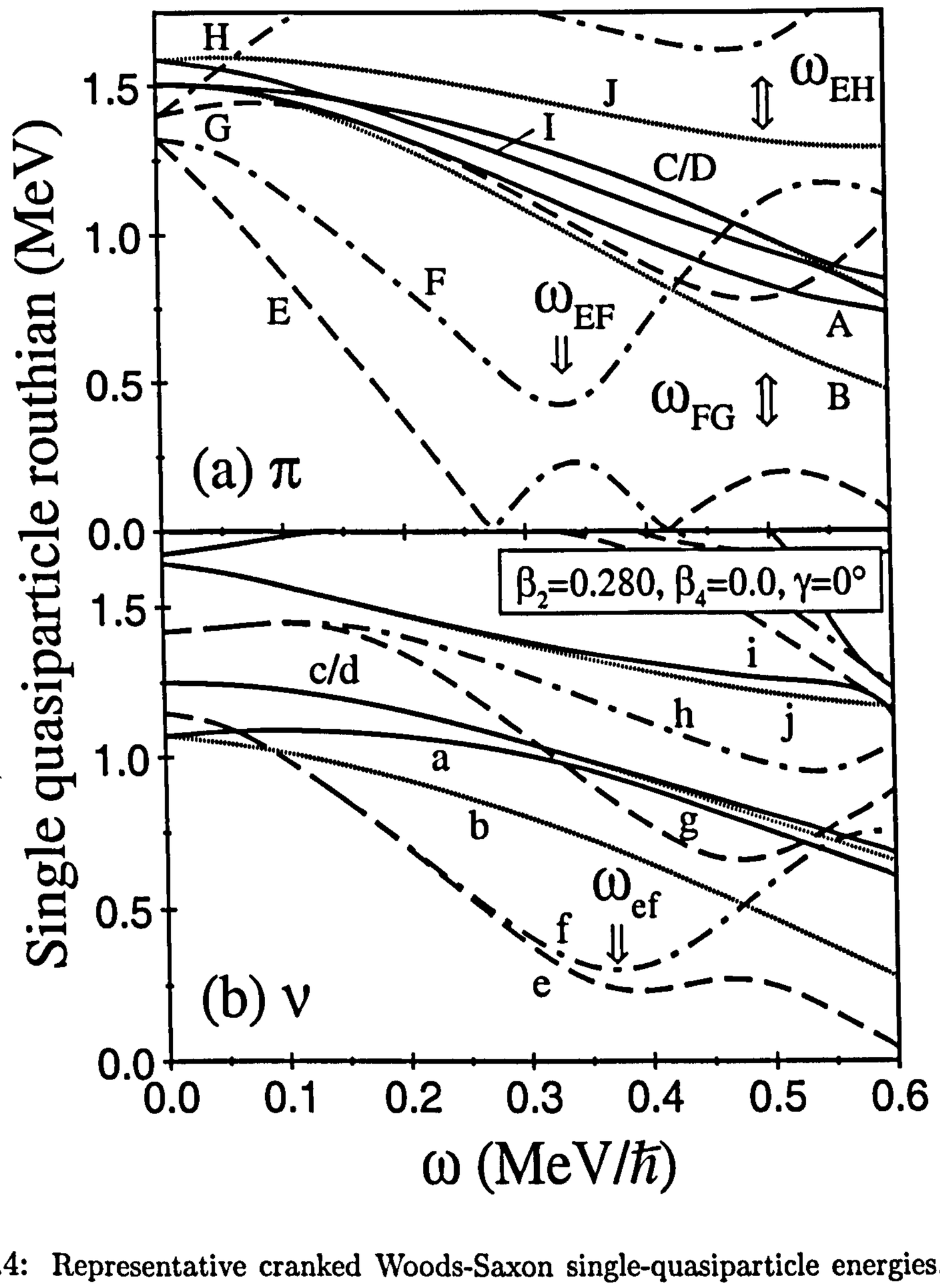

Figure 5.4: Representative cranked Woods-Saxon single-quasiparticle energies, appropriate for ^{124}La, for protons (a) and neutrons (b). The parity and signature (π,α) of the levels are (+,+1/2), solid lines; (+,−1/2), dotted lines; (−,−1/2), dashed lines; (−,+1/2), dot-dashed lines. Quasiparticle alignments are indicated by the arrows and labelled by the aligning quasiparticles.

modelled to decrease with increasing rotational frequency such that it has fallen by 50% at $\omega = 0.70$ MeV/$\hbar$ as detailed in Ref. [Wys88]. The calculations were performed over a decomposition of harmonic oscillator basis states, the dominant components of which are included in Table 5.1 for each level, together with each calculated g-factor [Cwi87], which in turn are determined by:

$$g_\Omega = \frac{1}{\Omega}[g_l\langle l_z\rangle + g_s\langle s_z\rangle], \tag{5.5}$$

where g_l is the g-factor corresponding to the orbital angular momentum and g_s is the g-factor for the intrinsic spin of either the proton or the neutron. To account for the fact that the nucleon is not free but bound within the nucleus, g_s is taken to be 70% of $g_{s,free}$, this value being the *quenching factor*. Also, it is assumed that $g_l = 1$ for protons and $g_l = 0$ for neutrons.

Table 5.1: Quasiparticle orbitals as labelled in Fig. 5.4 with their dominant Nilsson components and calculated g-factors. The calculations were performed with $\beta_2 = 0.28$ and $\gamma = 0°$.

Label		Nilsson configuration		
$\alpha = +1/2$	$\alpha = -1/2$	$[Nn_z\Lambda]\Omega^\pi$	Subshell	g-factor
A	B	$[422]3/2^+$ (91%)	$g_{7/2}$	0.54
C	D	$[404]9/2^+$ (93%)	$g_{9/2}$	1.32
F	E	$[550]1/2^-$ (89%)	$h_{11/2}$	1.65
H	G	$[541]3/2^-$ (90%)	$h_{11/2}$	1.50
I	J	$[420]1/2^+$ (80%)	$d_{5/2}$	2.52
a	b	$[411]1/2^+$ (77%)	$d_{3/2}$	1.85
c	d	$[413]5/2^+$ (92%)	$g_{7/2}$	0.38
f	e	$[523]7/2^-$ (90%)	$h_{11/2}$	–0.32
h	g	$[532]5/2^-$ (88%)	$h_{11/2}$	–0.38
i	j	$[402]5/2^+$ (75%)	$d_{5/2}$	–0.48

5.4 Experimental alignments

The experimental alignment plots [Ben79] described by Eq. 1.46, have been created for the five bands of ^{124}La and are shown in Fig. 5.5 as a function of rotational frequency (which can be approximated to $\omega \approx E_\gamma/2\hbar$ for $\Delta I = 2$ transitions). The Harris parameters used for

these plots were $\mathcal{J}_0 = 22.7\hbar^2$ MeV^{-1} and $\mathcal{J}_1 = 16.6\hbar^4$ MeV^{-3}. Band 1 displays an upbend at a rotational frequency of around 0.6 MeV/$\hbar$. Bands 3 and 4 show upbends around a rotational frequency of 0.5 MeV/$\hbar$. Band 5 exhibits a backbend at 0.3 MeV/$\hbar$ which is at a much lower frequency than the other bands.

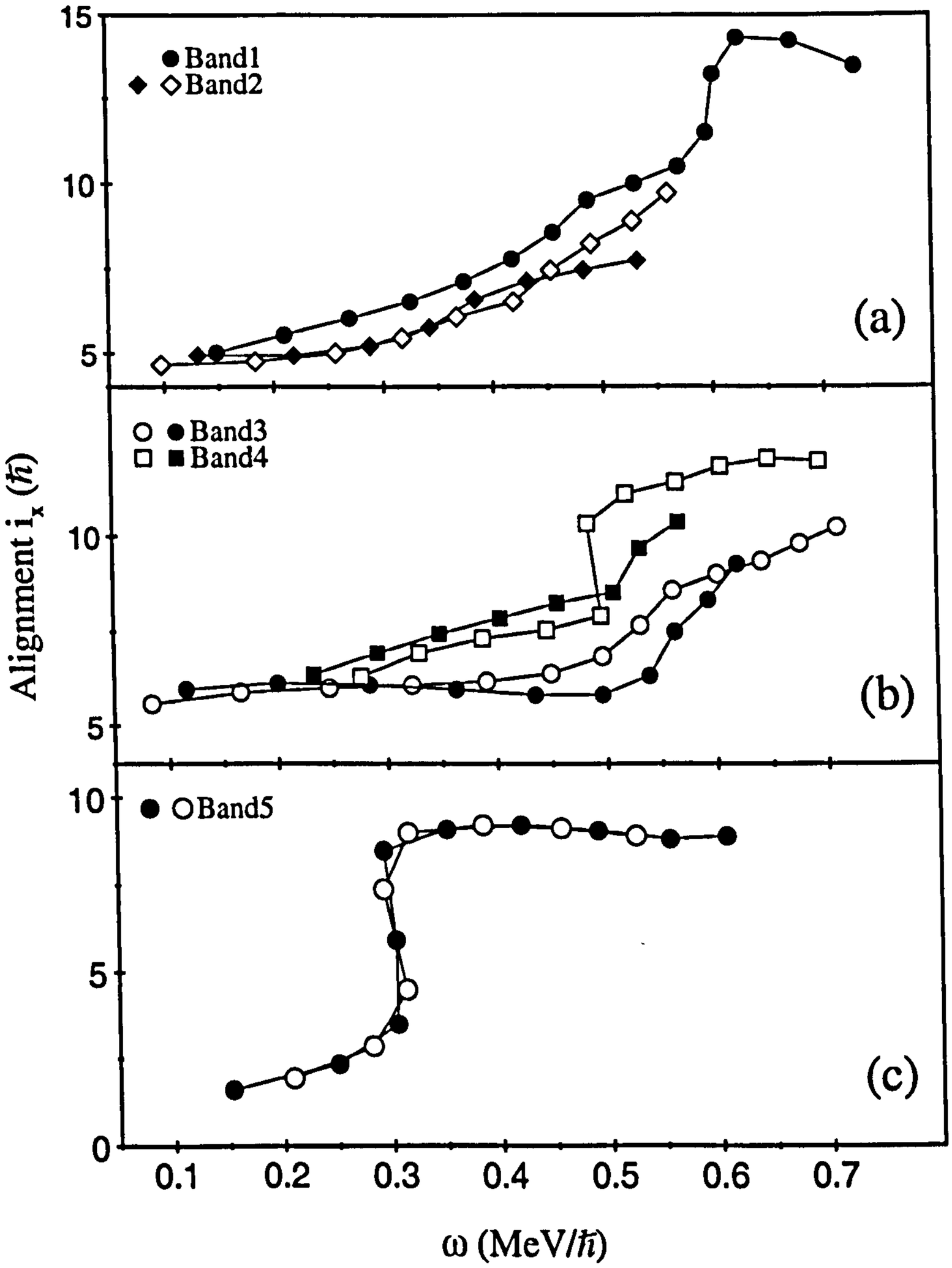

Figure 5.5: Experimental alignment plots for the bands in ^{124}La. (a) shows Band 1, the doubly decoupled band with a delayed neutron upbend. (b) shows the 'twin bands' 3 and 4 exhibiting upbends. (c) shows the alignment plot of band 5 with a backbend.

5.5 Rigid-rotor plots

In order to further investigate the structure of a specific configuration within ^{124}La, the level energy relative to a *rigid-rotor* reference can be plotted as a function of spin, yielding a rigid-rotor plot. The rigid-rotor energy reference E_{LD} is described as the energy given to a rotating liquid-drop (core) and is calculated by:

$$E_{LD} = \frac{\hbar^2}{2\mathcal{J}_{rig}} I(I+1), \tag{5.6}$$

where $\mathcal{J}_{rig}$ is the rigid-body moment of inertia which is usually normalised to ^{158}Er with $\beta_2 = 0.2$, such that:

$$\frac{\hbar^2}{2\mathcal{J}_{rig}} = 0.007 \left[\frac{158}{A}\right]^{\frac{5}{3}} \text{MeV}, \tag{5.7}$$

with A representing the mass number. This rigid-rotor reference is subsequently subtracted from the measured level energies of the particular nucleus and the resultant $E - E_{LD}$ is plotted against the spin. The rigid-rotor plots created for Bands 1–4 of ^{124}La are given in Fig. 5.6. It is evident in Fig. 5.6 that Band 3 is yrast upto a spin of $23\hbar$, about which Band 1 becomes more energetically favoured.

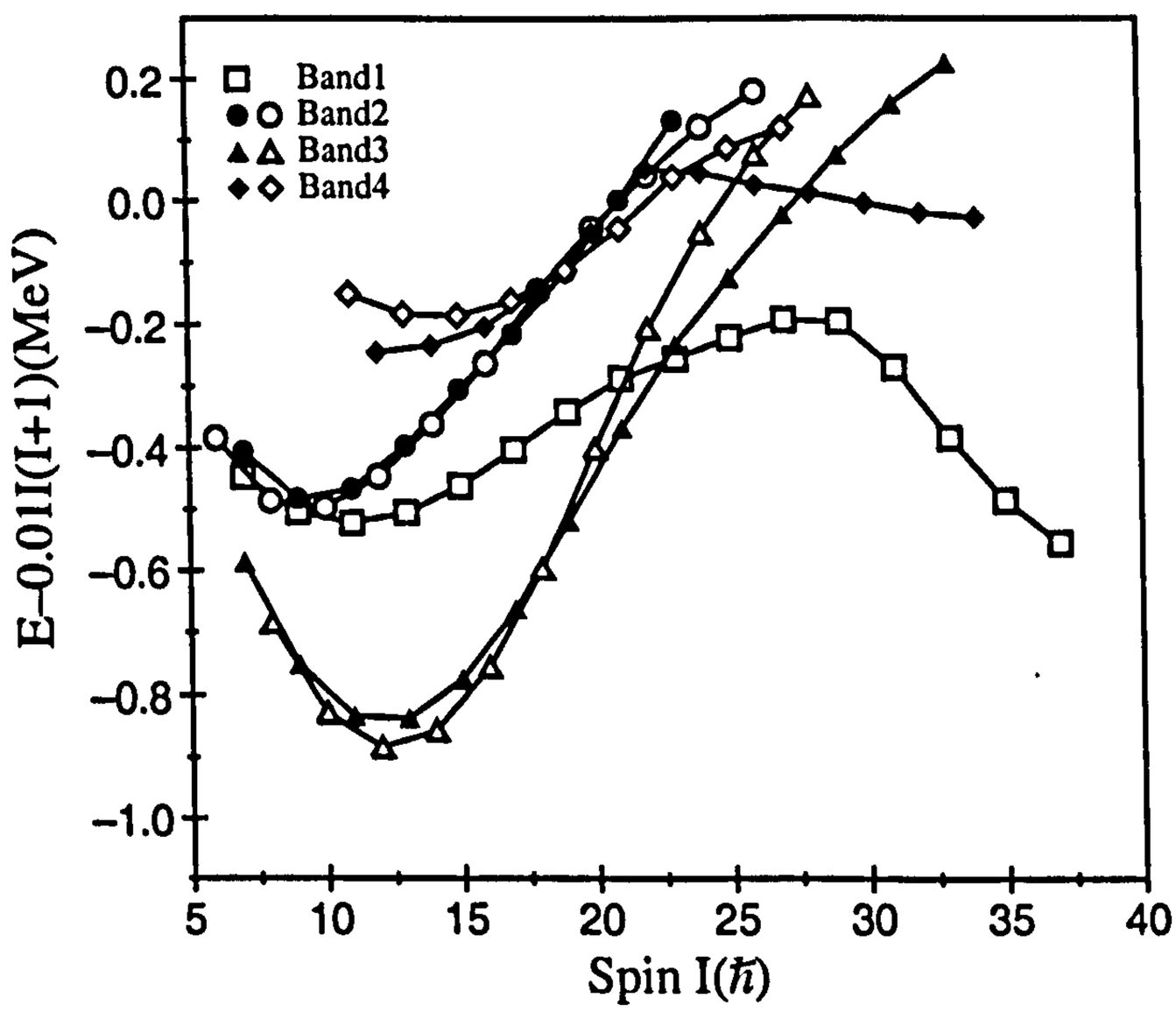

Figure 5.6: Experimental alignment plots for the bands in ^{124}La. It is shown that band 3 represents the yrast band at a low spin but that band 1 becomes yrast at high spin.

5.6 $B(M1)/B(E2)$ ratios of reduced transition probabilities

To test for the presence of signature staggering effects in ^{124}La, experimental ratios of reduced transition probabilities, $B(M1; I \rightarrow I-1)/B(E2; I \rightarrow I-2)$, have been extracted as a function of spin for the strongly coupled Bands 2, 3, 4 and 5. The results are shown in Fig. 5.7.

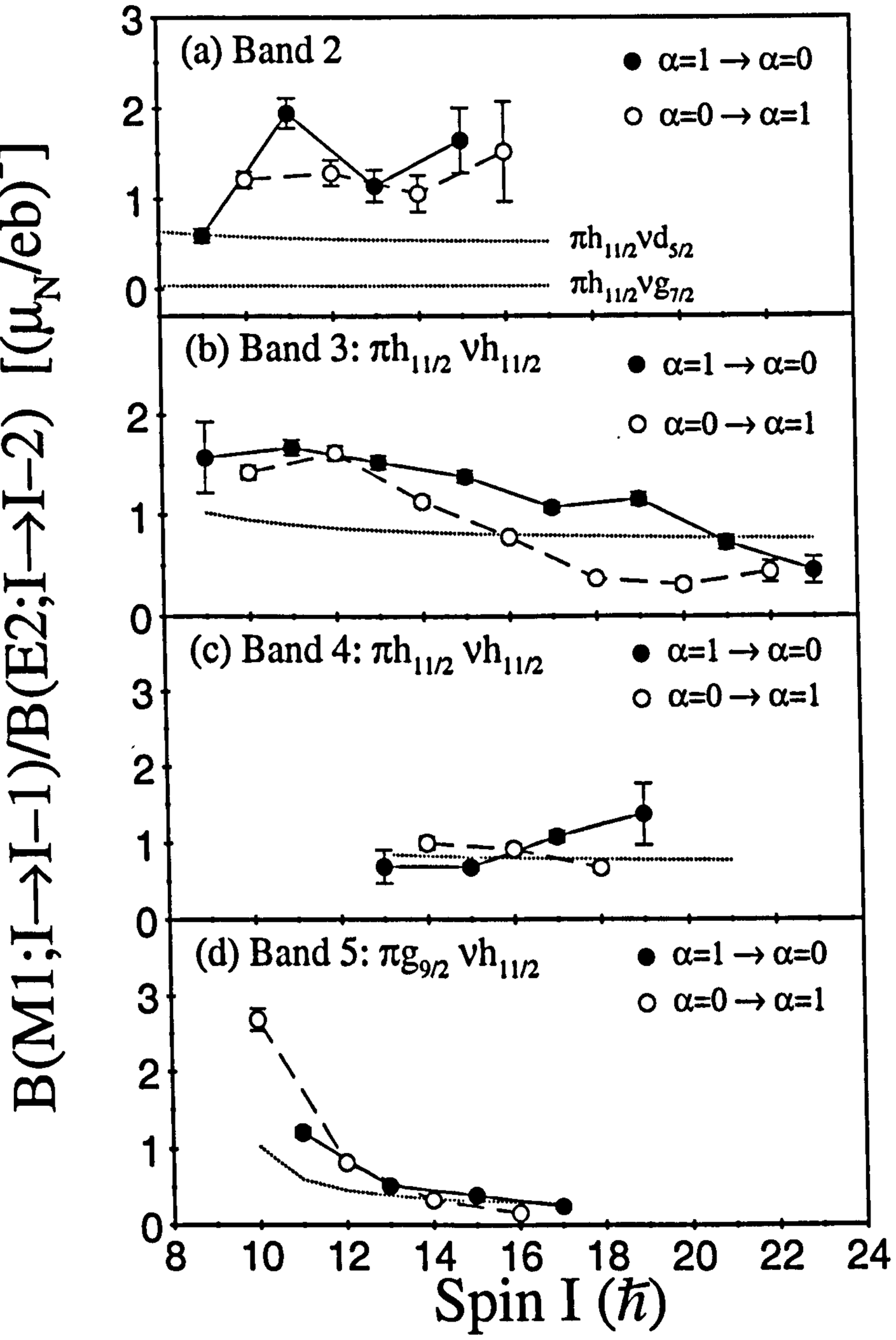

Figure 5.7: Experimental $B(M1; I \rightarrow I-1)/B(E2; I \rightarrow I-2)$ ratios of reduced transition probabilities for the $\Delta I = 1$ bands in ^{124}La. The dotted lines show the theoretical estimates obtained for the given configurations.

The experimental $E2/M1$ multipole mixing ratio δ (refer to Section. 1.12), where available, was used in calculating the $B(M1)/B(E2)$ ratios; otherwise δ was set to zero as the ratio, proportional to $[1+\delta^2]^{-1}$, is insensitive to the exact value of δ. The $B(M1)/B(E2)$ ratios can also be compared to theoretical estimates for given configurations to aid in band configuration assignment. The dotted lines shown in Fig. 5.7 refer to the theoretical estimates obtained for the given configurations using Eq. 1.69.

5.7 Configuration assignments

In addition to previous work, the gamma-ray properties measured in the present study and comparisons to the Woods-Saxon cranking calculations shown in Fig. 5.4, have allowed the assignment of quasiparticle configurations to the rotational bands of ^{124}La. The results are summarised in Table. 5.2 and the bands are discussed individually below.

Table 5.2: Quasiparticle assignments to the rotational bands in ^{124}La at low spin, for the corresponding quasiparticle orbital labels introduced in Table. 5.1

Band	Quasiparticle label	Dominant configuration
1	Eb	$\pi h_{11/2} \otimes \nu d_{3/2}$
2	Ei,Ej[a]	$\pi h_{11/2} \otimes \nu d_{5/2}$
3	Ee,Ef	$\pi h_{11/2} \otimes \nu h_{11/2}$
4	Fe,Ff	$\pi h_{11/2} \otimes \nu h_{11/2}$
5	Ce,De	$\pi g_{9/2} \otimes \nu h_{11/2}$

[a] Preferred assignment based on electromagnetic properties.

5.7.1 Band 1

Band 1 displays a decoupled nature and is therefore thought to be built upon a configuration with a low-K value. The configuration assigned is $\pi h_{11/2} \otimes \nu d_{3/2}$ with $\Omega = 1/2$, and has a $K^\pi = 1^-$ value. A similar sequence has been observed in the ^{126}La isotope [Tim00], and a decoupled band has been seen in the ^{126}Pr isotone [Har02]. There is a strong possibility that both these sequences are also built upon the same configuration. The evidence for a

rotational alignment of particles at approximately $\omega = 0.60$ MeV/$\hbar$, as shown in Fig. 5.5, has been linked to the ef alignment of $h_{11/2}$ neutrons which is blocked in all the other bands. The Woods-Saxon calculations shown in Fig. 5.4 actually predict this alignment to occur at $\omega_{ef} \approx 0.36$ MeV/$\hbar$, but the experimental alignment occurs much later than expected. This delay in the alignment of a neutron pair is a common feature of this mass region [Pau00] [Har99] and has been attributed to proton-neutron pairing or deformation effects.

5.7.2 Band 2

The structure of Band 2 is observed to result from the coupling of the $\pi h_{11/2}$ intruder orbital and a higher-lying positive-parity neutron orbital than that for Band 1. Fig. 5.4 shows that two such neutron orbitals, with $\Omega^\pi = 5/2^+$, can be proposed based upon $\nu[413]5/2^+$ ($g_{7/2}$, with near-degenerate signature components c and d) and $\nu[402]5/2^+$ ($d_{5/2}$, with components i and j). Theoretical calculations assuming $\beta_2 = 0.275$ and $\gamma = 0°$ as shown in Fig. 5.4 suggest that the $K^\pi = 3^-$, $\pi h_{11/2} \otimes \nu g_{7/2}$ configuration, with signature components Ec ($\alpha = 0$) and Ed ($\alpha = 1$) would be energetically favoured over the $K^\pi = 3^-$ $\pi h_{11/2} \otimes \nu d_{5/2}$ configuration with signature components Ei ($\alpha = 0$) and Ej ($\alpha = 1$). This is repudiated however by the measured $B(M1)/B(E2)$ ratios; as shown in Fig. 5.7 these ratios are more consistent with the estimates for the latter configuration, following the reasoning that the $l + 1/2$ νd$_{5/2}$ orbital induces larger $B(M1)$ values than the $l - 1/2$ $\nu g_{7/2}$ orbital. The $\pi h_{11/2} \otimes \nu d_{5/2}$ configuration is therefore the preferred assignment for Band 2, leading to the correct signature ($\alpha = 0$) being favoured at low spin as shown in Fig. 5.8. As an additional confirmation it should be noted that the $\pi h_{11/2} \otimes \nu d_{5/2}$ configuration has also been assigned to a corresponding band of the ^{126}La isotope [Tim00]. The cranking calculations can be reconciled with the preferred configuration by a slight alteration of the quadrupole deformation parameters. A decrease in β_2 will slightly lower the excitation energy of i and j ($\nu d_{5/2}$) in Fig. 5.4, or a more effective change can occur if triaxiality is introduced with $\gamma > 0°$. An increase in γ to approximately 20° actuates the c/d ($\nu g_{7/2}$) and i/j ($\nu d_{5/2}$) levels to become degenerate at zero frequency.

5.7.3 Bands 3 and 4

Bands 3 and 4 are collectively referred to as the *twin bands*, with both exhibiting the phenomenon of signature inversion and possessing the same $\pi h_{11/2} \otimes \nu h_{11/2}$ configuration.

Fig. 5.5 shows that Band 3 has a flat i_x for $\omega < 0.5$ MeV/$\hbar$, implying the $\pi h_{11/2} \otimes \nu h_{11/2}$ configuration through alignment blocking arguments, i.e neither the theoretical EF proton nor the ef neutron alignments of Fig, 5.4 are evident. The quasiparticle labels given to this band are the two signature components corresponding to the Ee (α= 1) and Ef (α = 0) configurations. As in Band 3, the proton EF and neutron ef of Fig. 5.4 are also absent (blocked) in Band 4 and hence this band is assigned an excited $\pi h_{11/2} \otimes \nu h_{11/2}$ structure, with the two signature components corresponding to Fe ($\alpha = 0$) and Ff ($\alpha = 1$) configurations respectively. Both Bands 3 and 4 display evidence for the rotational alignment at $\omega \approx$ 0.50 MeV/$\hbar$ that corresponds to the FG and EH alignments in Fig. 5.4. The rigid-rotor plot for Bands 3 and 4, displayed in Fig. 5.6, shows that the energy splitting between the bands decreases with increasing spin, and at $I \approx 26\hbar$, after a backbend, the excited band becomes energetically favoured. The signature splitting within the two bands can be related to the energy splitting of the $\nu h_{11/2}$ orbital, while the energy difference between the two bands is seen to be a result of the energy splitting of the $\pi h_{11/2}$ orbital. The latter splitting of the E and F orbitals is expected to increase with an increase in spin, as shown in Fig. 5.4, contrary to experiment. A similar situation has been observed in the corresponding bands of ^{134}Pr and has been attributed to different quadrupole deformations [Pet96] and more recently to chiral symmetry [Sta01].

Signature dependence in the twin bands

The favoured signature component of a specific j-shell is described by $\alpha_f = j \mathrm{mod} 2$ and the favoured signature component of a specific $j_\pi \otimes j_\nu$ shell-model configuration in a doubly-odd nucleus is expected to be:

$$\alpha_f = [j_\pi + j_\nu] \mathrm{mod} 2. \tag{5.8}$$

Therefore, the favoured signature component of the yrast $\pi h_{11/2} \otimes \nu h_{11/2}$ configuration should have $\alpha = [11/2 + 11/2] \mathrm{mod} 2 = 1$, or comprise odd spins. However, with this definition, Band 3 exhibits a signature inversion at low spin with the 'favoured' odd-spin component actually higher in energy than the 'unfavoured' even-spin component. Fig. 5.8 shows

this phenomenon along with the staggering plots for all four coupled bands. Fig. 5.8(b) and (c) displays a signature inversion at $I_c = 18.5\hbar$, corresponding to a rotational frequency $\omega = 0.45$ MeV/$\hbar$.

The splitting observed in Band 3 is related to the energy difference of the two signatures of the $\nu h_{11/2}$ orbital (levels e and f) in Fig. 5.4(b); it should be noted that the e and f orbitals are essentially degenerate at low spin/frequency and no signature splitting should therefore occur in Band 3 at low spin. Fig. 5.9 shows the corresponding $\pi h_{11/2} \otimes \nu h_{11/2}$ bands in neighbouring odd-odd ^{122}La [Fle01] and ^{126}La [Tim00] [Nya89], taking the spin assignments from smooth systematic trends as proposed by Ref. [Liu96]. The spin at which inversion occurs can be seen to increase with mass number as noted in Ref. [Smi98] for odd-odd nuclei of this mass region [Liu96].

In the case of Band 4 (Fig. 5.8(c)), there is a large signature splitting at low spin. The excited $\pi h_{11/2} \otimes \nu h_{11/2}$ configuration comprises the proton F orbital ($\alpha = 1/2$) coupled to the neutron e and f orbitals and the favoured signature Fe has $\alpha = 0$, or even spins. This is indeed the case for Band 4 at low spin, but there is now a signature inversion *above* I_c in contrast to the signature inversion *below* I_c in Band 3. Moreover, the signatures are inverted once more in Band 4 at $I = 24.5\hbar$, though this could be a result of perturbations of the smooth band behaviour by alignments of quasiparticle pairs. Indeed, as seen in Fig. 5.5, there is a sharp backbend in the $\alpha = 1$ signature of Band 4 at $\omega \approx 0.5$ MeV/$\hbar$ rather than a more gradual upbend as seen in the $\alpha = 0$ signature and both signatures of Band 3. This behaviour of the signature in Bands 3 and 4 at low spin is described as a 'signature quartette' in Ref. [Taj94], where the excited $\pi h_{11/2} \otimes \nu h_{11/2}$ band is predicted to display a signature inversion *above* the critical spin.

The two $\pi h_{11/2} \otimes \nu h_{11/2}$ bands in ^{124}La display behaviour similar to the chiral-partner bands seen in this mass region [Sta01] [Hec01] [Har01], where low-spin signature inversion is seen in the $\pi h_{11/2} \otimes \nu h_{11/2}$ yrast configuration. Furthermore, it is suggested that signature inversion and chirality may be intimately related [Rie01]. The experimental $B(M1; I \rightarrow I-1)/B(E2; I \rightarrow I-2)$ ratios for Band 3 also show a clear signature dependence, as seen in Fig. 5.7(b) and more clearly in Fig. 5.10. The ratios are larger for the transitions from the $\alpha = 1$ signature to the $\alpha = 0$ signature compared to those for the transitions from the $\alpha = 0$ signature to the $\alpha = 1$ signature. Nevertheless, unlike

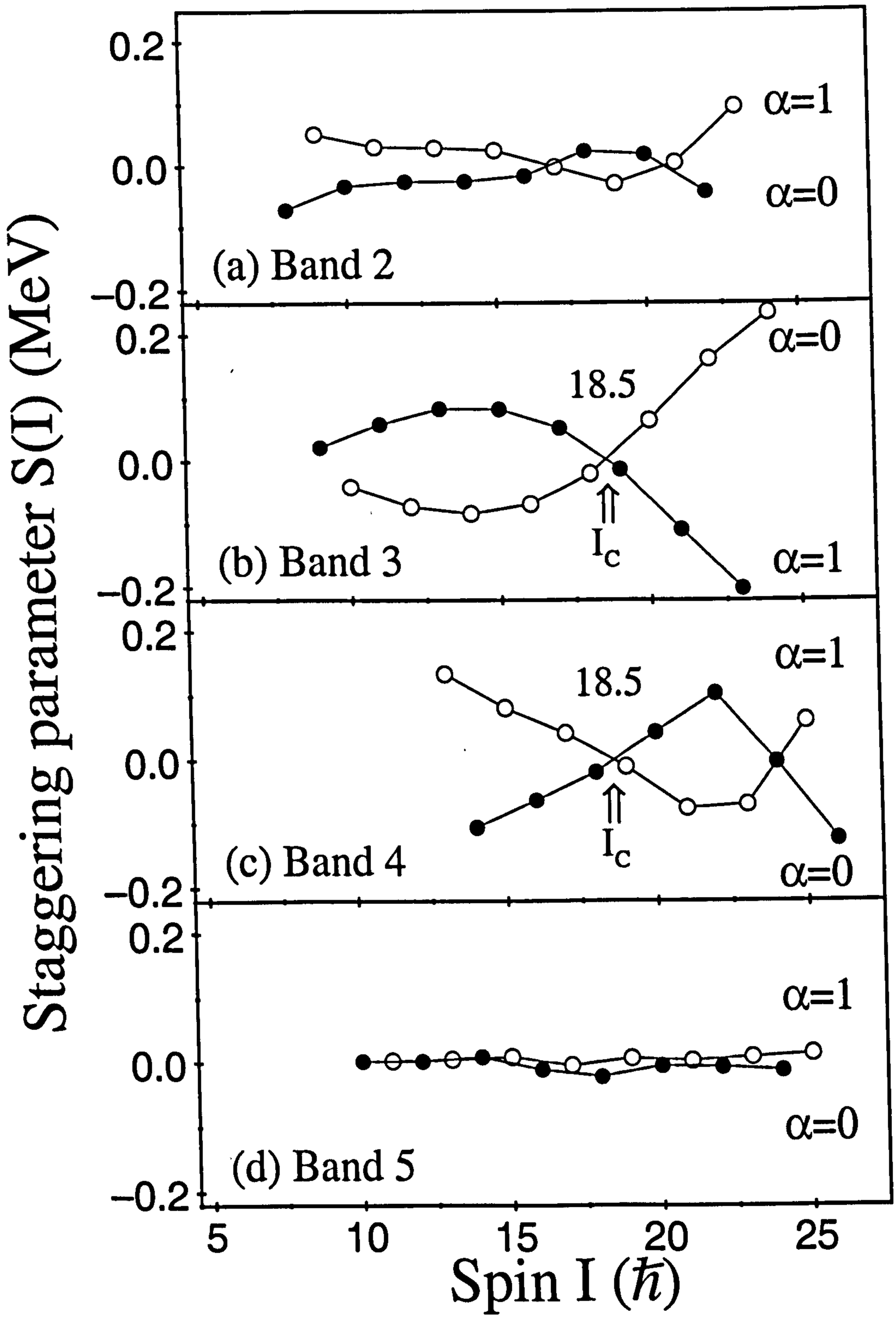

Figure 5.8: Plot of the energy staggering parameter $S(I)$ versus the assumed spin I for the $\Delta I = 1$ bands in ^{124}La. The solid and open symbols represent the two signatures of each band, with the solid symbol corresponding to the theoretically 'favoured' component and the open symbol corresponding to the 'unfavoured' component.

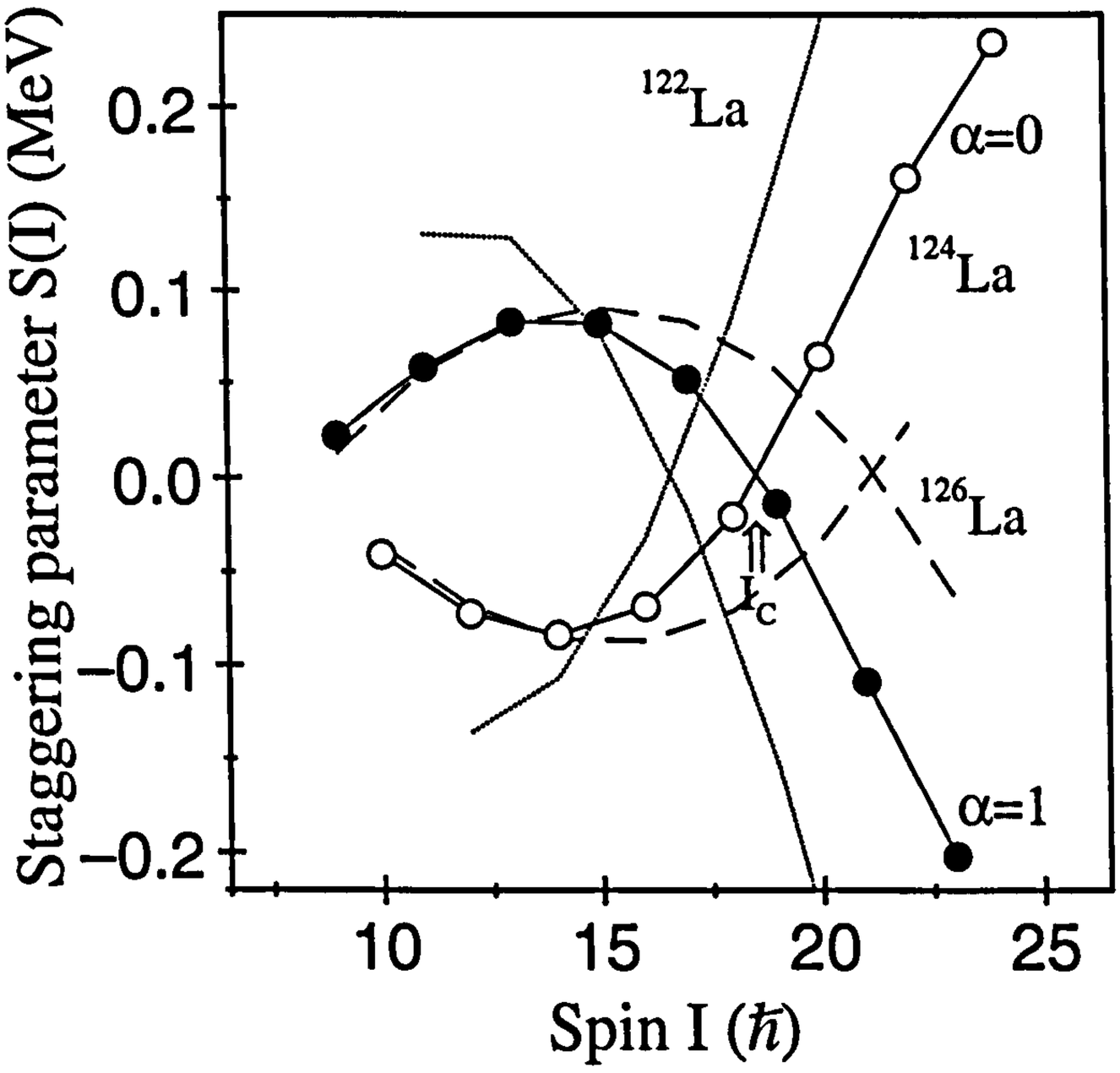

Figure 5.9: Plot of the energy staggering parameter $S(I)$ versus assumed spin I for Band 3. The dotted and dashed lines represent the corresponding bands in ^{122}La and ^{126}La, respectively.

the level energies, no signature inversion is evident, although this is consistent with neighbouring odd-odd nuclei [Ced92] [Kom93]. The calculated $B(M1)/B(E2)$ ratios for the $\pi h_{11/2} \otimes \nu h_{11/2}$ configurations are included in Figs. 5.8(a) and 5.8(c) and generally agree with the experimental values. The experimental $B(E2; I \rightarrow I-1)/B(E2; I \rightarrow I-2)$ ratios for Band 3 have also been measured, but due to insufficient sensitivity the signature effects could not be examined. However, an average value of approximately 0.03 was deduced, and the results of these measurements are shown in Fig. 5.11. Any signature dependence (staggering) that is apparent in either the $B(M1; I \rightarrow I-1)/B(E2; I \rightarrow I-2)$ or the $B(E2; I \rightarrow I-1)/B(E2; I \rightarrow I-2)$ values is attributed to the $\Delta I = 1$ reduced transition probabilities rather than the $B(E2; I \rightarrow I-2)$ values as neither experimental nor theoretical evidence exists which suggests that the $B(E2; I \rightarrow I-2)$ value should exhibit significant signature-dependent effects. The reason for the signature dependence of the $M1$ transition

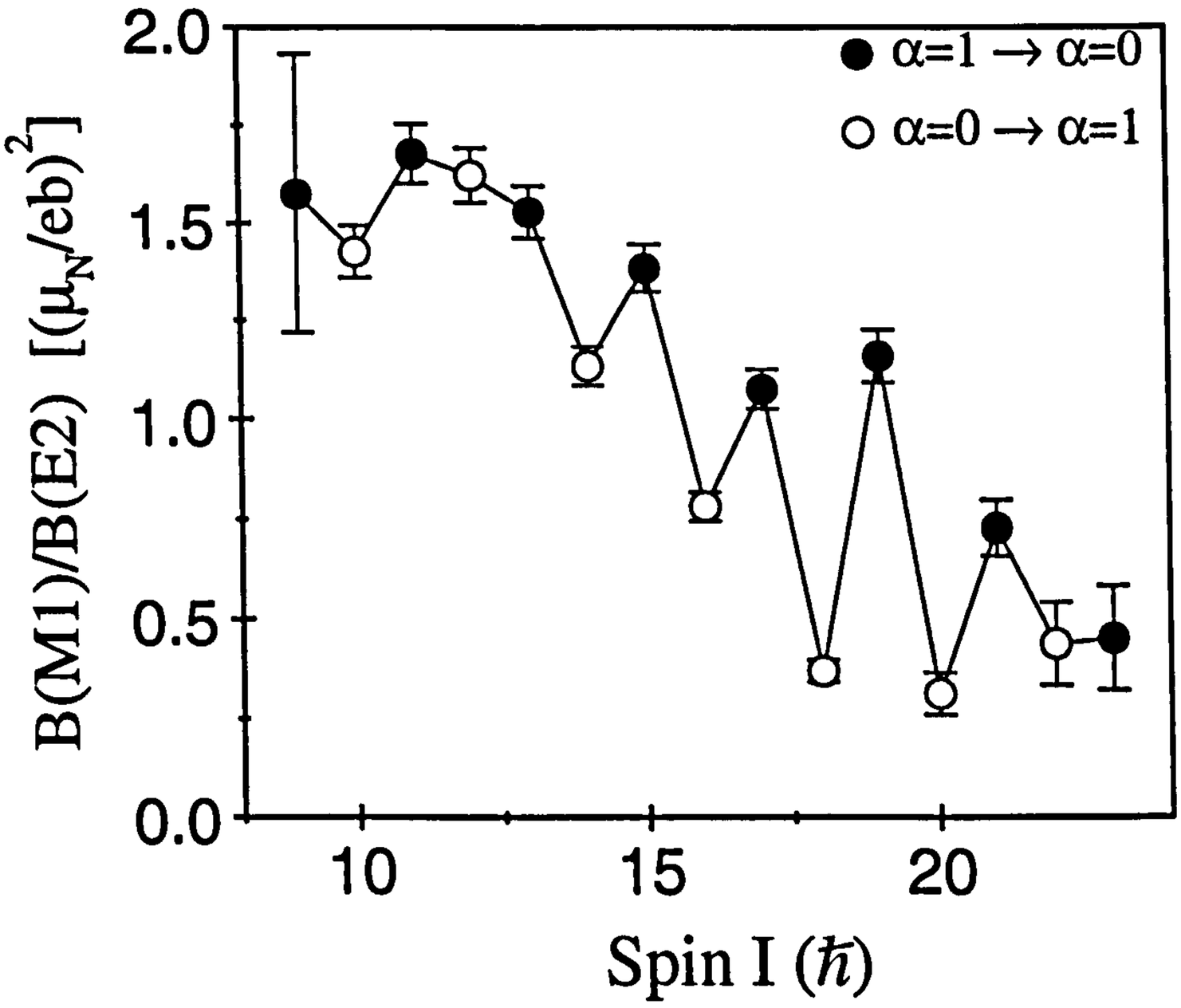

Figure 5.10: Experimental B(M1;$I \rightarrow I-1$)/B(E2;$I \rightarrow I-2$) ratios of reduced transition probabilities for Band 3 showing a clear signature dependence maximal at a spin $I = (18.5\hbar)$, the inversion spin.

probabilities is thought to be purely due to the Coriolis mixing of $\Omega \doteq 1/2$ states in the nuclear wavefunction and occurs for both axially symmetric and triaxial shapes. However, a significant signature dependence of the non-stretched $E2$ transition probabilities only occurs for non-axial shapes [Ham83].

A triaxial nuclear shape has been proposed as a reason for the signature inversion phenomena, with $\gamma > 0°$ (see Fig. 1.4) in conjunction with the specific position of the Fermi surface within a given subshell [Ben84]. A positive value of γ corresponds to a rotation about the short axis of the triaxial nuclear shape. Fig. 5.12 shows the cranked-shell model calculations for ^{124}La where it is observed that only a slightly positive value of γ is needed for signature inversion to be apparent in the $\nu h_{11/2}$ orbital. The results displayed in Fig. 5.12 are calculated at a rotational frequency of $\omega = 0.25$ MeV/$\hbar$, and the inversion of the e and f orbitals can be seen for $\gamma > 4°$. For higher frequencies the inversion point increases

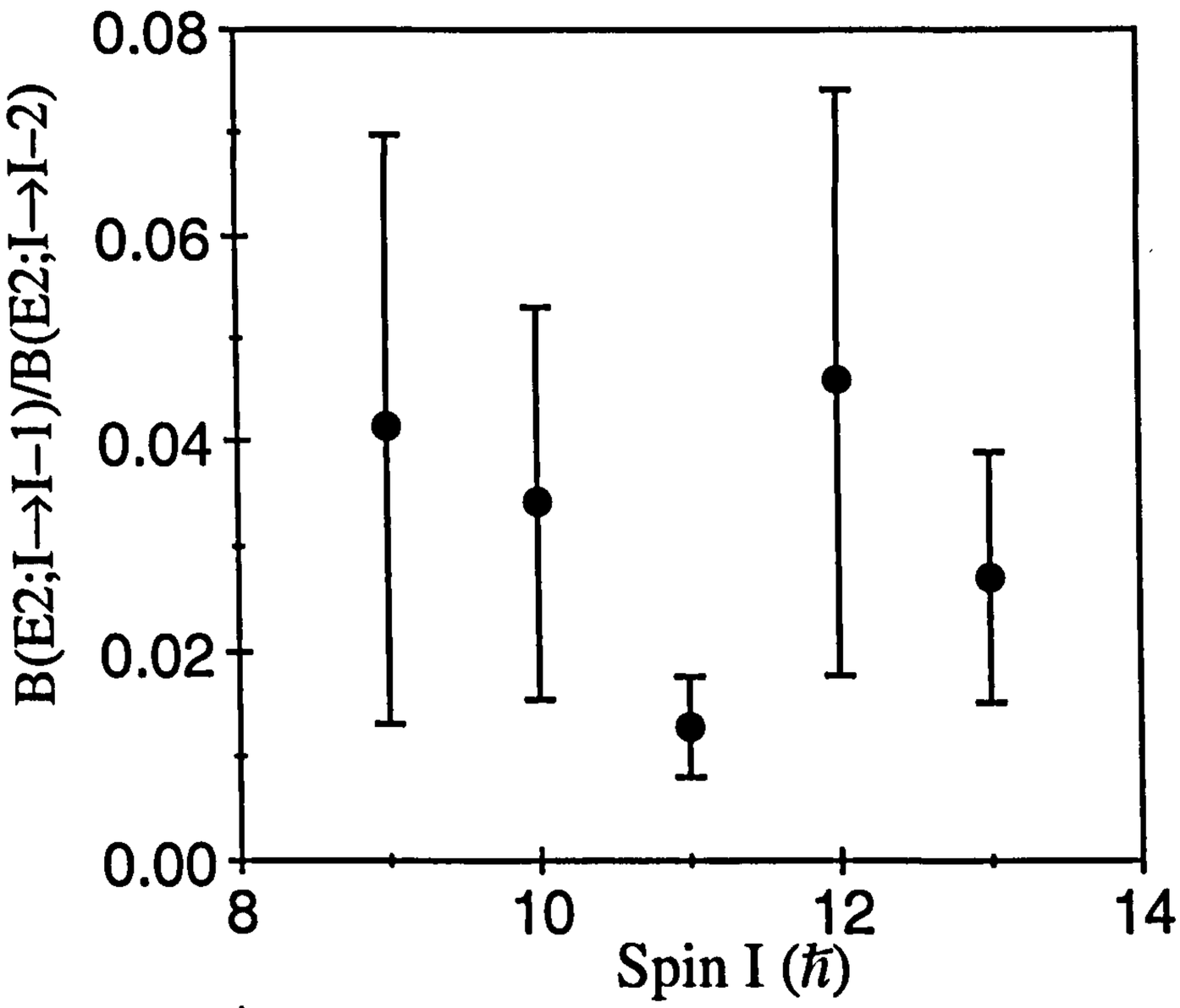

Figure 5.11: Experimental $B(E2; I \rightarrow I-1)/B(E2; I \rightarrow I-2)$ ratios of reduced transition probabilities for Band 3 in ^{124}La.

slightly such that at $\omega = 0.50$ MeV/$\hbar$, $\gamma = 10°$. Therefore it can be argued that the signature inversion apparent in Band 3 of ^{124}La can be simply explained by a small positive γ deformation ($\gamma > 4°$) at $I < I_c$ and an axially-symmetric shape ($\gamma \approx 0°$) for $I > I_c$. However, in the case of Band 4 the *opposite* effect would be needed to explain the signature inversion i.e $\gamma \approx 0°$ for $I < I_c$ and $\gamma > 4°$ for $I > I_c$. This scenario seems unlikely and therefore suggests that signature inversion is related to other physical effects rather than triaxiality.

As signature inversion is only ever observed in multi-quasiparticle configurations, another theory to which it has been attributed is that of the residual proton-neutron interaction [Ced92]. In the case of a semidecoupled [Kre84] (i.e one high Ω particle and one low Ω particle) structure, such as Band 3, low-spin signature inversion has been attributed to a large repulsive matrix element of the $p-n$ force acting in the maximally aligned intrinsic state [Car99]. It is suggested in Ref. [Kre84] that signature inversion is expected at low-spins, but with increasing rotation the expected signature order is established. Semmes and

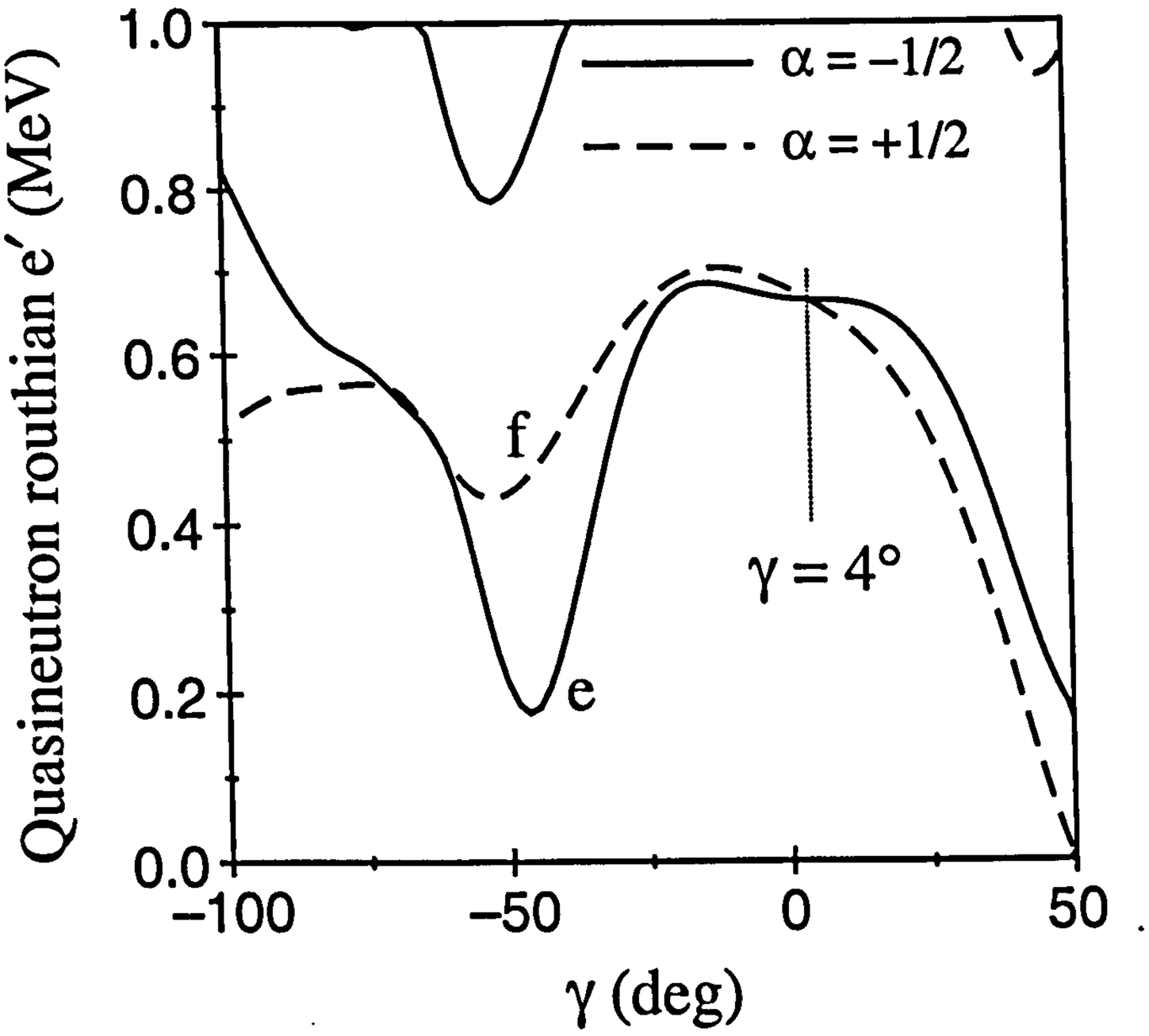

Figure 5.12: Quasineutron levels calculated as a function of the triaxiality parameter γ for ^{124}La at a rotational frequency $\omega = 0.25 MeV/\hbar$. An inversion of the e and f levels, derived from a $\nu h_{11/2}$ orbital is apparent at $\gamma = 4°$, which is very close to the axial prolate shape with $\gamma = 0°$.

Ragnarsson [Sem91] have also shown cases in which the odd-proton–odd-neutron residual interaction can induce signature inversion in prolate shapes, where both the proton and neutron occupy high-j states. If correct, axial asymmetry of the nucleus can be dismissed as a prerequisite for this phenomenon.

A more recent consideration of the origins of signature inversion has focussed upon quadrupole pairing correlations [Xu00]. Here, even when considering a triaxial shape, the addition of the quadrupole pairing force increases the signature splitting by $\sim$ 40 keV, whereas previous γ deformation calculations could not account for this. 'Extended TRS' calculations [Xu00] which include a quadrupole pairing force suggest that the $(\lambda\mu) = (22)$ component is dominant in the induction of signature inversion in A$\sim$125 nuclei around the

$\nu h_{11/2}$ midshell, i.e nuclei with N = 65, 67; two prime examples of such systems are ^{122}La and ^{124}La. The Extended TRS calculations predict a triaxial shape for the $\pi h_{11/2} \otimes \nu h_{11/2}$ configuration in ^{124}La, with $\beta_2 \approx 0.29$ and $\gamma \approx 13°$, in agreement with the QPCM calculations which also give $\gamma \approx 13°$. The simpler TRS calculations that were employed in the present study yielded an axially symmetric shape, in contrast to the extended calculations. This difference can be used in conjunction with measured $B(M1)$ rates, as proposed in Ref. [Hag89], as a test of triaxiality. Taking a unique-parity high-spin orbital (such as $h_{11/2}$) in an odd-A nucleus, the following relation has been shown [Hag89] to be valid for axially symmetric shapes in the cranking approximation:

$$\frac{\Delta B(M1)}{\langle B(M1)\rangle} = \frac{4(\Delta e'/\hbar\omega)}{1+(\Delta e'\hbar\omega)^2}. \tag{5.9}$$

The difference between the $B(M1)$ rates for $\Delta I = 1$ transitions from one signature to the other and vice versa is given by $\Delta B(M1) = B(M1; I \rightarrow I-1) - B(M1; I-1 \rightarrow I-2)$, and $\langle B(M1)\rangle$ is the mean value. The quantity $\Delta e'/\hbar\omega$ is the ratio of the experimental signature splitting of the Routhians divided by the rotational frequency. Assuming a constant rotational stretched $B(E2)$ rate, the $B(M1)$ values of Eq. 5.9 may be substituted by the measured $B(M1)/B(E2)$ ratios (see Fig. 5.7). If Eq. 5.9 can be generalised to the case of two unique-parity orbitals in an odd-odd nucleus (e.g the $\pi h_{11/2} \otimes \nu h_{11/2}$ configuration for ^{124}La) then it immediately implies that there should be no signature dependence in the $B(M1)$ rates when $\Delta e' = 0$, i.e $\Delta B(M1) \rightarrow 0$ around the signature-inversion spin $I_c = 18.5\hbar$. A comparison of the two sides in Eq. 5.9 therefore provides the test of triaxiality. The results of this test for Band 3 are shown in Fig. 5.13, where a constant difference in the ratios is observed for spins below $20\hbar$. However, at $I \approx 22\hbar$, which is just above the signature-inversion spin, the ratios become approximately equal. This behaviour could indicate a shape change from triaxial ($\gamma > 0°$) to axially symmetric ($\gamma = 0°$) around the inversion spin.

5.7.4 Band 5

Band 5 is somewhat anomalous as it could not be connected to the main structure of the constructed level scheme. It is seen to contain strong $\Delta I = 1$ transitions with positive A_2 coefficients for the angular distributions, which in turn implies that $\delta > 0$. This unusual

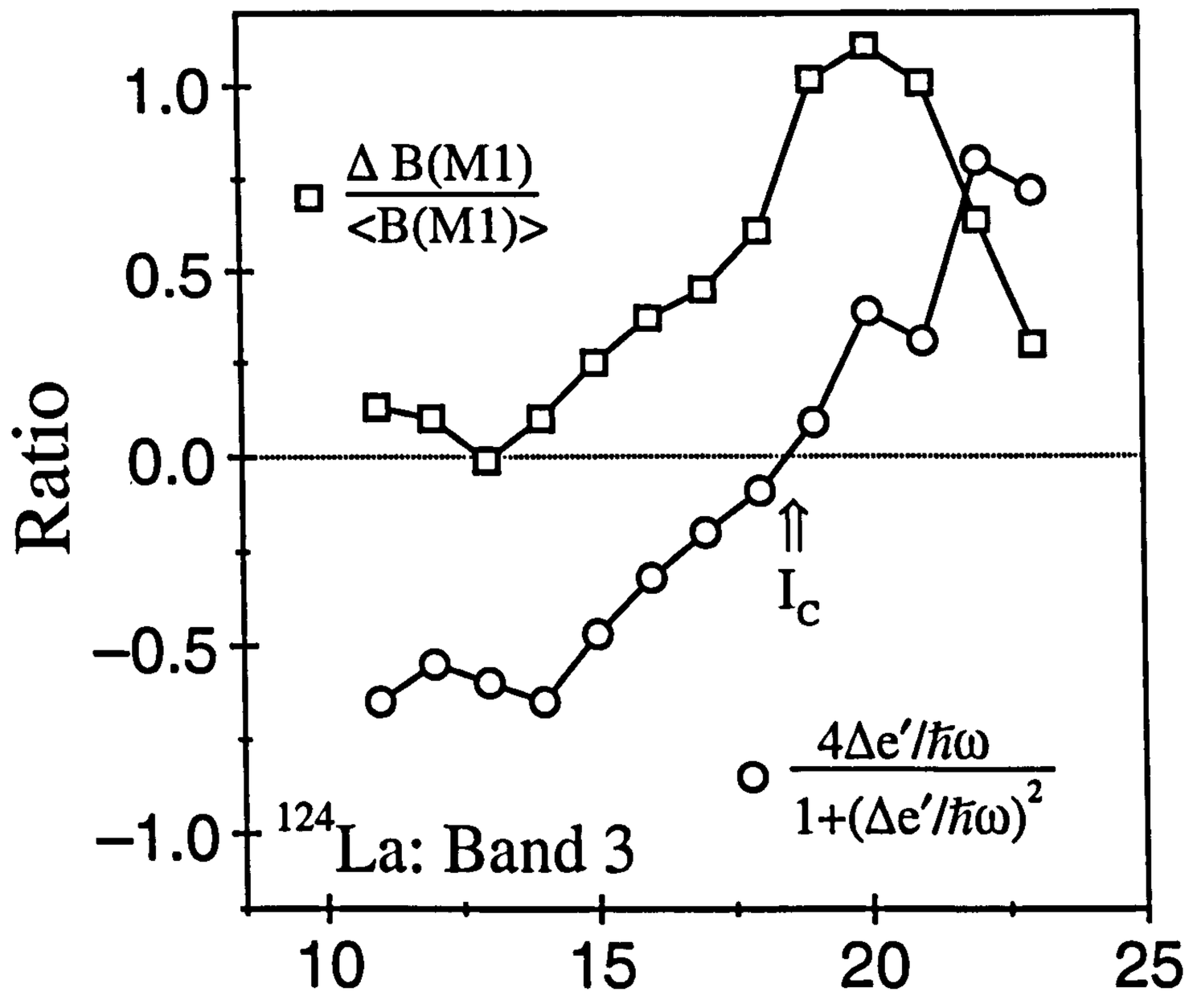

Figure 5.13: These given ratios plotted for Band 3 as a function of spin should be equal for an axially symmetric shape, as discussed in the text.

behaviour is characteristic of the $\pi g_{9/2}$ orbital that originates from below the spherical Z = 50 shell gap, but due to the large deformation ($\beta \approx 0.28$) is brought close to the $Z = 57$ Fermi surface. The influence of this orbital has been observed in the systematics of the $\Delta I = 1$ bands in this region, where $\pi g_{9/2} \otimes \nu h_{11/2}$ bands in doubly-odd antimony (Z = 51) [Vaj83] and iodine (Z = 53) [Qua84] have been found with positive multipole mixing ratios. Band 5 is thus assigned a similar $\pi g_{9/2} \otimes \nu h_{11/2}$ configuration with degenerate signature components Ce ($\alpha = 0$) and De ($\alpha = 1$). This configuration has $K^\pi = 8^-$ based upon the $\pi[404]9/2^+ \otimes \nu[523]7/2^-$ orbitals, which leads to the spin and parity assignments given in Fig. 4.12, indeed the high K nature of the bandhead is thought to explain the high-spin isomer observed by Idrissi *et al* [Idr92]. The positive mixing ratios, as discussed in Section. 5.6, is related to the sign of the quantity ($g_K - g_R$) for a prolate nuclear shape and when estimated using Eq. 1.70 is indeed found to be positive for this assigned configuration.

Unlike all the other bands observed, Band 5 is not built upon an $h_{11/2}$ proton orbital. This sequence therefore exhibits the EF proton alignment of an $h_{11/2}$ pair, as shown in Fig. 5.7; this first proton alignment is blocked in all the other bands as they are built upon a $h_{11/2}$ proton orbital. The alignment is seen experimentally to take place at a rotational frequency of $\omega \approx 0.30$ MeV/$\hbar$ which is close to the theoretically predicted frequency shown in Fig. 5.4. Similar alignments are seen in strongly coupled $\pi g_{9/2}$ bands of the neighbouring odd-A nuclei ^{121}La [Ced91], ^{123}La [Wys89], and ^{125}La [Har99]. Fig. 5.5 shows that both signature partners are degenerate below $I = 14\hbar$, though a small splitting is apparent above this spin with the expected $\alpha = 0$ component favoured.

This current band represents the first evidence for the $\pi g_{9/2} \otimes \nu h_{11/2}$ structure in odd-odd lanthanum ($Z = 57$) isotopes, even though the $\pi_{9/2}$ orbital is manifest in neighbouring odd-A ^{121,123,125}La isotopes. Furthermore, this orbital is a key ingredient of the highly deformed (or 'superdeformed') configurations ($\beta_2 \geq 0.35$) in heavier mass $A \sim 130$, $Z < 60$ nuclei [Gali94] [Gal94] [Bro97] [Har97] [Kon99] [Mul98] [Afa96].

5.8 Systematics of the mass~120 region

From the systematic study of the $\pi h_{11/2} \otimes \nu h_{11/2}$ bands observed in doubly odd lanthanum isotopes, it is found, see Fig. 5.14, that as the neutron number decreases, the intraband level spacing also decreases. This is a consequence of an increased moment of inertia, which is a function of deformation, thereby indicating that the deformation increases as the neutron Fermi surface drops away from $N = 82$. The same effect is seen with the isotones, where a systematic decrease in the transition energy within an isotone chain occurs as the number of protons increases. This is displayed in Fig. 5.15. Here the deformation, and hence the moment of inertia, increases as the Fermi surface moves away from the $Z = 50$ closed shell. The structure of the ^{124}La nucleus ascertained in the present study is consistent with these neighbouring isotonic and isotopic systematic trends, thereby adding support for the proposed spin-parity assignments and transition energies.

The rotational frequencies at which band crossings occur is plotted in Fig. 5.16 for the $\pi h_{11/2}$, and the $\pi_{9/2}$ configurations in odd-A lanthanum nuclei with $N = 64 - 74$. Data for ^{124}La have been added to the values shown in Ref. [Har99], and both data sets agree well with the systematics. While only a few bands based on the extruder [404]9/2$^+$ orbital in La

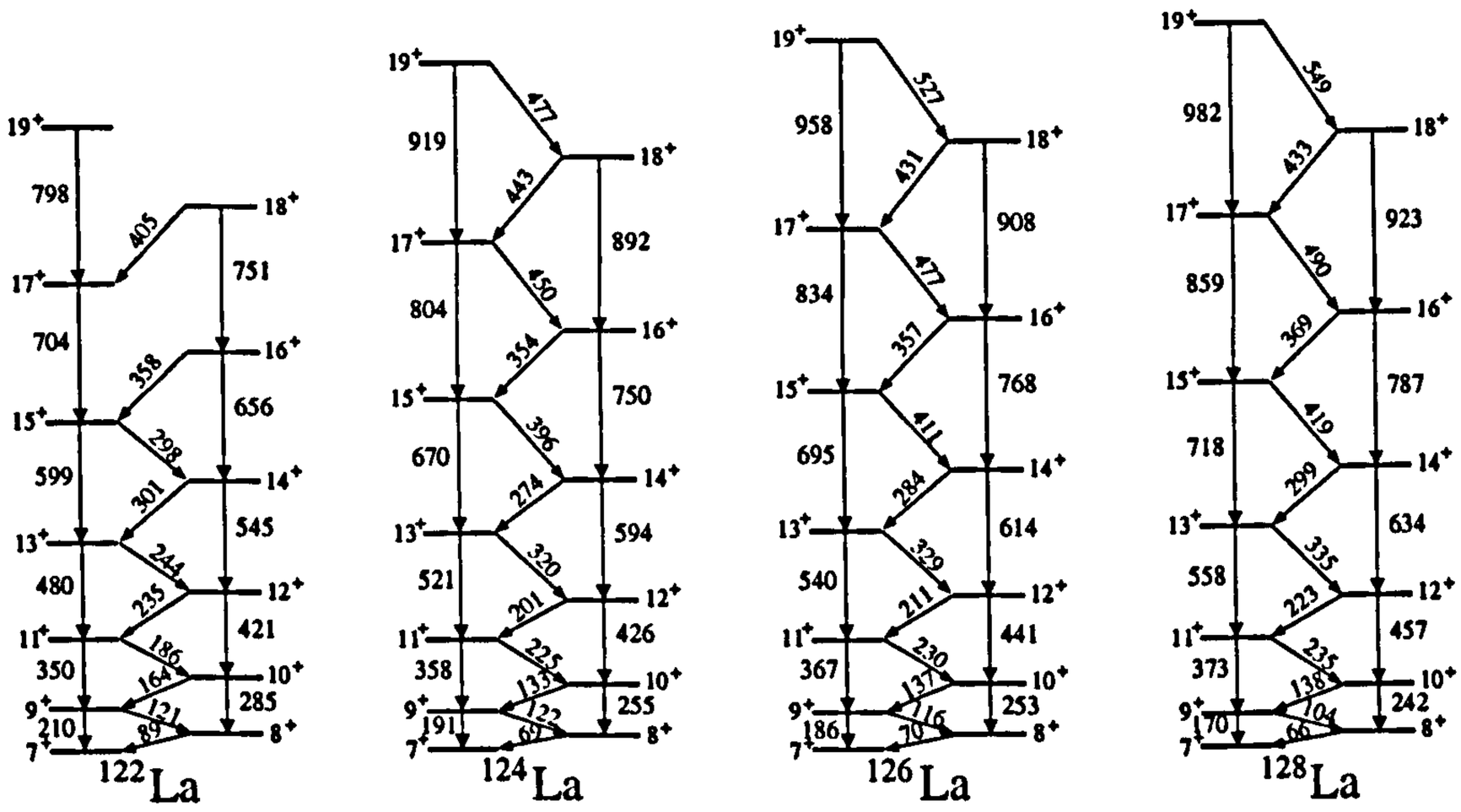

Figure 5.14: Illustrations of the energy levels schemes of the $\pi h_{11/2} \otimes \nu h_{11/2}$ configuration bands in the light odd-odd lanthanum isotopes for $N = 65 - 71$. Results for ^{122}La were obtained for the first time from the present experiment [Fle01]

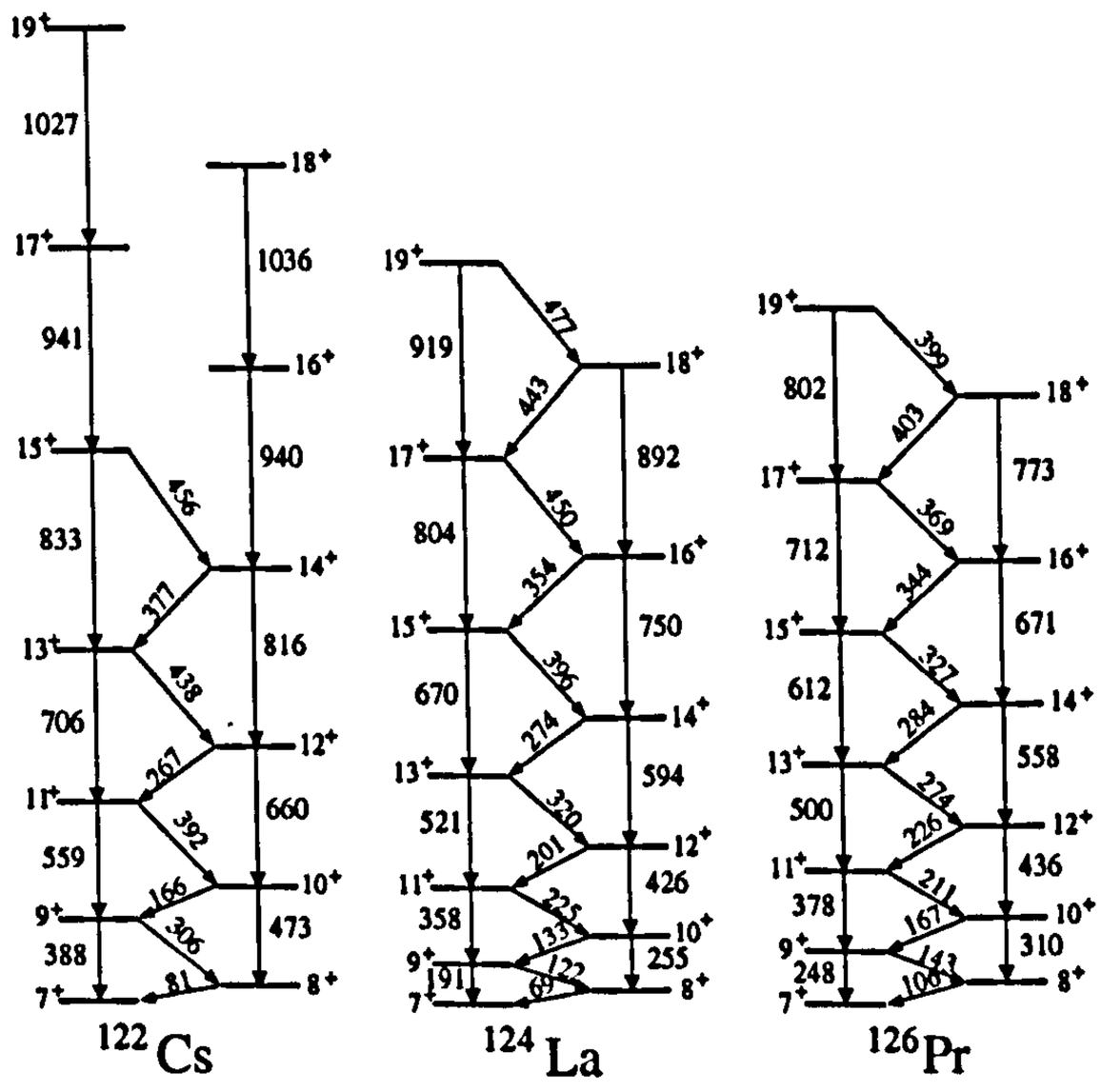

Figure 5.15: Illustrations of the energy levels schemes of the $\pi h_{11/2} \otimes \nu h_{11/2}$ configuration bands for ^{124}La and its neighbouring isotones.

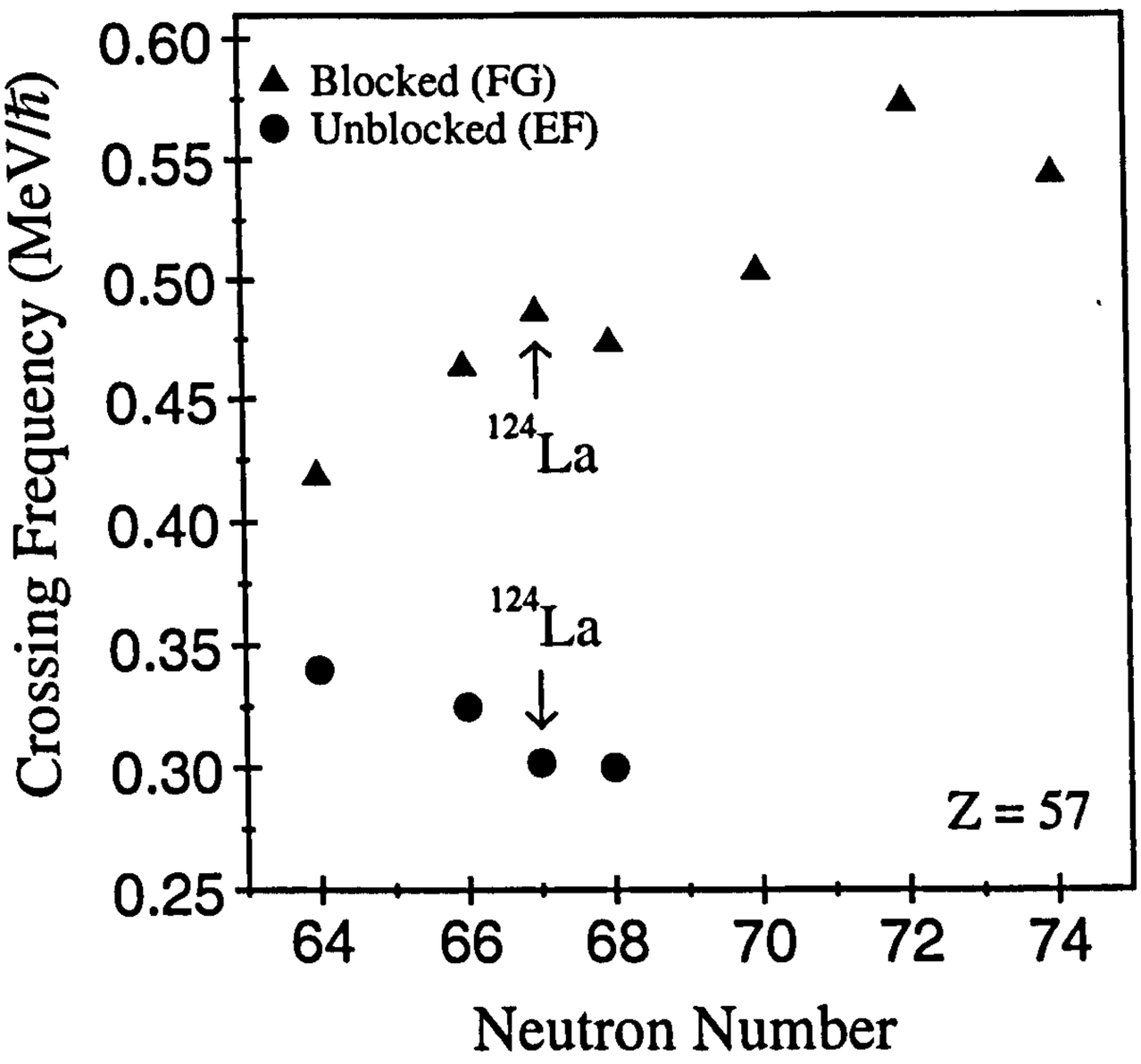

Figure 5.16: Proton crossing frequencies for lanthanum isotopes. The values for ^{124}La added to this study are marked and shown in the plot as squares.

nuclei have been extended into the band crossing region, they appear to cross in a frequency range close to the expected value and so the configuration of Band 5 can be confirmed with these systematics.

Chapter 6

Conclusion

The doubly odd nucleus $^{124}_{57}La_{67}$ has been studied using the $^{64}Zn(^{64}Zn,3p1n)^{124}La$ reaction at a bombarding energy of 260 MeV. The Gammasphere gamma-ray spectrometer, in conjunction with ancillary charged-particle and neutron detectors and the Argonne Fragment Mass Analyser, has been used to observe high-spin structures in this nucleus. The previously observed [Kom93] decay scheme has been confirmed and extended to higher spin. Two additional rotational bands have been discovered and from the observation of interband linking transitions, four of the five rotational bands have been connected. The electromagnetic character and multipolarity of these linking transitions have been determined using angular distribution and $\gamma - \gamma$ angular correlation ratios measurements, enabling the subsequent assignment of the spins and parities of the rotational bands. Furthermore, a comparison of the rotational behaviour of individual bands to cranking calculations has led to the configuration assignments of these bands.

Two of the bands have been assigned a $\pi h_{11/2} \otimes \nu h_{11/2}$ configuration (one yrast band and one excited band) and exhibit the phenomenon of signature inversion. The lowest state of the yrast band (Band 3) has been assigned a spin and parity of $I^{\pi} = 7^{+}$, which is supported by systematic studies of the neighbouring isotopes, and by the comparison of experimental values to those calculated by the core-quasiparticle coupling model. A signature inversion is observed in Band 3 *below* $I_c = (18.5\hbar)$, whereas the signature inversion exhibited in Band 4 is observed *above* $I_c = (18.5\hbar)$. The signature dependence (staggering) found in the yrast band is also evident in the $B(M1)/B(E2)$ ratios of reduced transition probabilities, although no change of phase (inversion) is observed; the ratios are largest for the transitions

from the $\alpha = 1$ signature to the $\alpha = 0$ signature.

A $\Delta I = 2$ band (Band 1) has been observed and is thought to be built upon the doubly-decoupled $\pi h_{11/2} \otimes \nu d_{3/2}$ configuration with $K^{\pi} = 1^{-}$. The experimental neutron alignment for this band occurs at higher spin than predicted from cranked shell calculations, this mirrors the neutron alignments in the $\pi h_{11/2}$ bands of neighbouring odd-A lanthanum isotopes. A signature partner band (Band 2) with an assigned $\pi h_{11/2} \otimes \nu d_{5/2}$ configuration has been observed, which is similar to the same configuration observed in ^{126}La. Finally, a strongly coupled band, based on a high-K ($K^{\pi} = 8^{-}$) $\pi g_{9/2} \otimes \nu h_{11/2}$ configuration (Band 5) has also been established. Gamma rays originating from Band 5 were not observed in prompt coincidence with the gamma rays from the remaining rotational bands. It is therefore presumed that Band 5 is built upon the 'high-spin' isomer observed in previous β-decay studies. This represents the first evidence for the $\pi g_{9/2}$ proton (hole) orbital in a doubly odd lanthanum isotope.

The extensive study of the nuclear structure of ^{124}La by gamma-ray spectroscopy has therefore contributed to a deeper understanding of doubly odd isotopes in this neutron deficient region of the Segré chart.

References

[Afa96] A. V. Afanasjev, and I. Ragnarsson, Nucl. Phys. **A608**, 176 (1996).

[And76] C. G. Andersson, S. E. Larsson, G. Leander, P. Möller, S. G. Nilsson, I. Ragnarsson, S. Åberg, R. Bengtsson, J. Dudek, B. Nerlo-Pomorska, K. Pomorski, and Z. Szymański, Nucl. Phys. **A268**, 205 (1976).

[AtlURL] "*Atlas Accelerator Facility*" URL:http://www.phy.anl.gov/atlas/

[Bea96] C. W. Beausang, and J. Simpson, J. Phys. G: Nucl. Phys. 22 **5**, 527 (1996).

[Ben84] R. Bengtsson, Nucl. Phys **A415**, 189 (1984).

[Ben79] R. Bengtsson, and S. Frauendorf, Nucl. phys. **A327**, 139 (1979).

[Ben84] R. Bengtsson, H. Frisk, F. R. May, and J. A. Pinston, Nucl. Phys. **A415**, 189 (1984).

[Ben93] Ragnar Bengtsson, Nucl. Phys **A557** 277c (1993).

[Bla91] M. Blann, Lawrence Livermore National Laboratory report, UCRL-JC-109052, November (1991).

[Bog58] N. N. Bogoliubov, Soviet Phys. JETP **7**, 41 (1958).

[Boh51] A. Bohr, Phys. Rev. **81**, 134 (1951).

[Boh53] A. Bohr, and B. R. Mottelson, Mat. Fys. Medd. Dan. Vid. Selsk. **27** No. 16 (1953).

[Boh75] A. Bohr, and B. R. Mottelson, *Nuclear Structure*, VolII. Benjamin, New York (1975).

[Boh81] A. Bohr, and B. R. Mottelson, Phys. Scr. **24**, 71 (1981).

[Bra72] M. Brack, J. Damgaard, A. S. Jensen, H. C. Pauli, V. M. Strutinski, and C. Y. Wong, Rev. Mod. Phys. **44** (1972).

[Bro97] T. B. Brown, J. Pfohl, M. A. Riley, D. J. Hartley, D. G. Sarantites, M. Devlin, D. R. LaFosse, F. Lerma, D. E. Archer, R. M. Clark, P. Fallon, I. M. Hibbert, D. T. Joss, P. J. Nolan, N. J. O'Brien, E. S. Paul, R. K. Sheline, J. Simpson, R. Wadsworth, and Y. Sun, Phys. Rev. C, **56**, R1210 (1997).

[Car99] M. A. Cardona, A. J. Kreiner, D. Hojman, G. Levinton, M. E. Debray, M. Davidson, J. Davidson, R. Pirchio, H. Somacal, D. R. Napoli, D. Bazzacco, N. Blasi, R. Burch, D. De Acuña, S. M. Lenzi, G. Lo Bianco, J. Rico, and C. Rossi-Alvarez, Phys. Rev. C **59**, 1298 (1999).

[Ced91] B. Cederwall, A. Johnston, B. Fabt, S. Juutinen, P. Ahonen, S. Mitarai, J. Mukai, and J. Nyberg, Z. Phys. A **338**, 463 (1991).

[Ced92] B. Cederwall, F. Lidén, A. Johnson, L. Hildingsson, R. Wyss, B. Fant, S. Juutinen, P. Ahonen, S. Mitarai, J. Mukai, J. Nyberg, I. Ragnarsson, and P. B. Semmes, Nucl. Phys. **A542**, 454 (1992).

[Cha02] H. J. Chantler, E. S. Paul, A. J. Boston, M. P. Carpenter, R. Charity, C. J. Chiara, P. T. W. Choy, C. N. Davids, M. Devlin, A. M. Fletcher, D. B. Fossan, D. G. Jenkins, N. S. Kelsall, T. Koike, D. R. LaFosse, P. J. Nolan, D. G. Sarantites, D. Seweryniak, J. F. Smith, K. Starosta, R. Wadsworth, and A. N. Wilson, Phys. Rev. C **66**, 014311 (2002).

[Cwi87] S. Cwiok, J. Dudek, W. Nazarewicz, W. Skalski, and T. Werner, Comput. Phys. Commun. **46**, 379 (1987).

[Dav89] C. N. Davids, and James D. Larson, Nucl. Instr. Meth **B40/41** 1224 (1989).

[Dav92] C. N. Davids, B. B. Back, K. Bindra, D. J. Henderson, W. Kutschera, T. Lauritsen, Y. Nagame, P. Sugathan, A. V. Ramayya, and W. B. Walters, Nucl. Instrum. Methods Phys. Res. B **70**, 358 (1992).

[Der74] E. Der. Mateosian, and A. W. Sunyar, At. Data Nucl. Data Tables **13**, 391 (1974).

[Dev96] M. Devlin, L. G. Sobotka, D. G. Sarantites, D. R. LaFosse, Nucl. Instr. Meth **A383**, 506 (1996).

[Dia94] H. Dias, and L. Losano, Phys. Rev. C **50**, 1377 (1994); and references therein.

[Dön79] F. Dönau, and U. Hagemann, Z. Phys. A **293**, 31 (1979); and references therein.

[Dön82] F. Dönau, and S. Frauendorf, *in Proceedings of the Conference on High Angular Momentum Properties of Nuclei, Oak Ridge, 1982*, edited by N. R. Johnson (Harwood Academic, New York 1983) p143.

[Dön87] F. Donau, Nucl. Phys. **A471**, 469 (1987).

[Dro80] Ch. Droste, D. Chlebowska, J. Dobaczewski, F. Dönau, A. Kerek, G. Leander, J. Srebrny, and W. Waluś. Nucl. Phys. A **341**, 98 (1980); and references therein.

[Eis70] J. M. Eisenberg, and W. Greiner, *Nuclear Models*, North Holland, Amsterdam. (1970).

[Fer65] A. J. Ferguson, *Angular Correlation Methods in Gamma-ray Spectrosopy*, North Holland, Amsterdam (1965).

[Fle01] A. M. Fletcher, private communication.

[Fra65] H. Frauenfelder, and R. M. Steffen, *Alpha-, Beta-, and Gamma-ray Spectroscopy* (ed. K. Siegbahn) p.997, North Holland, Ansterdam (1965).

[Gali94] A. Galindo-Uribarri, D. Ward, T. Drake, G. Hackman, V. P. Janzen, S. M. Mullins, S. Pilotte, D. C. Radford, I. Ragnarsson, N. C. Schmeing, and J. C. Waddington, Phys. Rev. C, **50**, R2655 (1994).

[Gal94] A. Galindo-Uribarri, S. M. Mullins, D. Ward, M. Cromaz, J. DeGraaf, T. E. Drake, S. Flibotte, V. P. Janzen, D. C. Radford, and I. Ragnarsson, Phys.Rev.C **54**, R454 (1994).

[Gal58] C. J. Gallagher, Jr. and S. A. Moszkowski, Phys. Rev. **111**, 1282 (1958).

[Gil75] R. D. Gill, *Gamma-ray Angular Correlations*, Academic Press, London (1975).

[Gus67] C. Gustafson, I. L. Lamm, and S. G. Nilsson. Arkiv Fysik **36** (1967).

[Hag89] G. B. Hagemann, and I. Hamamoto, Phys. Rev. C **40**, 2862 (1989).

[Ham83] I. Hamamoto, and B. R. Mottelson, Phys. Lett. **132B**, 7 (1983).

[Har65] S. M. Harris, Phys. Rev. **138**, B509 (1965).

[Har97] D. J. Hartley, J. Pfohl, M. A. Riley, D. G. Sarantites, M. devlin, D. R. LaFosse, D. E. Archer, T. B. Brown, R. M. Calrk, P. Fallon, I. M. Hibbert, D. T. Joss, P. J. Nolan, N. O'Brien, E. S. Paul, R. K. Sheline, J. Simpson,and R. Wadsworth, Phys. Rev. C, **55**, R985 (1997).

[Har99] D. J. Hartley, L. L. Riedinger , H. Q. Jin, W. Reviol, B. H. Smith, A. Galindo-Uribarri, D. G. Sarantites, D. R. LaFosse, J. N. Wilson, and S. M. Mullins, Phys. Rev. C **60**, 014308 (1999).

[Har01] D. J. Hartley, L. L. Riedinger, M. A. Riley, D. L. Balabanski, F. G. Kondev, R. W. Laird, J. Pfohl, D. E. Archer, T. B. Brown, R. M. Clark, M. Devlin, P. Fallon, I. M. Hibbert, D. T. Joss, D. R. LaFosse, P. J. Nolan, N. J. O'Brien, E. S. Paul, D. G. Sarantites, R. K. Sheline, S. L. Shepherd, J. Sipmson, R. Wadsworth, Jing-Ye Zhang, P. B. Semmes, and F. Dönau, Phys. Rev. C, **64**, 031304(R) (2001).

[Har02] D. J. Hartley, L. L. Riedinger, M. Danchev, W. Reviol, O. Zeidan, and Jing-ye Zhang, Phys. Rev. C **65**, 044329(R) (2002).

[Hec01] A. A. Hecht, C. W. Beausang, K. E. Zyromski, D. L. Balabanski, C. J. Barton, M. A. Caprio, R. F. Casten, J. R. Cooper, D. J. Hartley, R. Krücken, D. Meyer, H. Newman, J. R. Novak, E. S. Paul, N. Pietralls, A. Wolf, N. V. Zamfir, Jing-Ye Zhang, and F. Dönau, Phys. Rev. C **63**, 051302(R) (2001).

[Hil53] D. L. Hill, and J. A. Wheeler, Phys. Rev. **89**, 1102 (1953).

[Idr92] N. Idrissi, A. Gizon, J. Genevey, P. Paris, V. Barci, D. Barnćoud, J. Blachot, D. Bucurescu, R. Duffait, J. Gizon, C. F. Liang, and B. Weiss, Z. Phys. **A341**, 427 (1992).

[Ing54] D. R. Inglis, Phys. Rev. **96**, 1059 (1954).

[Ing56] D. R. Inglis, Phys. Rev. **103**, 1786 (1956).

[Kno89] G. F. Knoll, *RadiationDetectionandMeasurement* Second Edition., John Wiley ans Sons, New York (1989).

[Koi01] T. Koike, private communication.

[Kom93] T. Komatsubara, K. Furano, T. Hosoda, J. Mukai, T. Hayakawa, T. Morikawa, Y. Iwata, N. Kato, J. Espino, J. Gascon, N. Gjørup, G. B. Hagemann, H. J. Jensen, D. Jerrestam, J. Nyberg, G. Sletten, B. Cederwall, and P. O. Tjøm, Nucl. Phys. **A557**, 419c (1993).

[Kon99] F. G. Kondev, M. A. Riley, D. J. Hartley, T. B. Brown, R. W. Laird, M. Lively, J. Pfohl, R. K. Sheline, R. M. Clark, P. Fallon, D. G. Sarantites, M. Devlin, D. R. LaFosse, F. Lerma, R. Wadsworth, I. M. Hibbert, N. J. O'Brien, E. S. Paul, D. T. Joss, P. J. Nolan, S. L. Shepherd, D. E. Archer, and J. Simpson, Phys. Rev. C, **59**, 3076 (1999).

[Krä89] A. Krämer-Flecken, T. Morek, R. M. Lieder, W. Gast, G. Hebbinghaus, H. M. Jäger, and W. Urban, Nucl. Instrum. and Methods Phys. Res. A **275**, 333 (1989)

[Kra73] K. S. Krane, R. M. Steffen, and R. M. Wheeler, Nucl. Data Tables **A11** 351 (1973).

[Kre79] A. J. Kreiner, and M. A. J. Mariscotti, Phys. Rev. Lett. **43**, 1150 (1979).

[Kre80] A. J. Kreiner, and M. A. J. Mariscotti, J. Phys. G: Nucl. Phys. **6**, L13 (1980).

[Kre84] A. J. Kreiner, J. Davidson, M. Davidson, D. Abriola, C. Pomar, and P. Thieberger, Phys. Rev. C. **36**, 2309 (1987).

[Lee90] I. Y. Lee, Nucl. Phys. **A520**, 641c (1990).

[Lie78] R. M. Lieder, and H. Ryde, *Adv. in Nucl. Phys.*, M. Baranger and E. Vogt, Plenum Publ. Corp., New York, vol.10, (1978).

[Liu95] Y. Liu, Y. Ma, H. Yang, and S. Zhou, Phys. Rev. C **52**, 2514 (1995).

[Liu96] Y. Liu, J. Lu, Y. Ma, S. Zhou, and H. Zheng, Phys. Rev. C **54**, 719 (1996).

[Mat74] E. der Mateosian, and A. W. Sunyar, At. Nucl. Data Tables **13**, 391 (1974).

[May50] M. G. Meyer, Phys.Rev. **78**, 22 (1950).

[Mic] "*The Microball*", URL:http://wunmr.wustl.edu/ dgs/mball/

[Mor98] T. Morek, K. Starosta, Ch. Droste, D. Fossan, G. Lane, J. Sears, J. Smith, and P. Vaska, Eur. Phys. J. A **3**, 99 (1998).

[Mor63] H. Morinaga, and P. C. Gugelot, Nucl. Phys. **46**, 210 (1963).

[Mul98] S. M. Mullins, A. Galindo-Uribarri, C. E. Svensson, R. A. E. Austin, G. C. Ball, M. Cromaz, V. P. Janzen, D. C. Radford, I. Ragnarsson, J. C. Waddington, amd D. Ward, Phys. Rev. C, **58**, 2626 (1998).

[Mye69] W. D. Myers, and W. J. Swiatecki, Ann. Phys. (NY) **55**, 395 (1969).

[Naz85] W. Nazarewicz, J. Dudek, R. Bengtsson, and I. Ragnarsson, Nucl. Phys. **A435**, 397 (1985).

[Naz87] W. Nazarewicz, G. A. Leander, and J. Dudek, Nucl. Phys. **A467**, 437 (1987).

[Naz89] W. Nazarewicz, R. Wyss, and A. Johnson, Nucl. Phys. **A503**, 285 (1989).

[Neu] "*The Neutron Shell*", URL:http://wunmr.wustl.edu/ dgs/NeutronShell/

[Nil55] S. G. Nilsson, Mat. Fys. Medd. Dan. Vid. Selsk. **29** (1955) No. 16. *68, 70, 71, 72, 76.*

[Nol94] P. J. Nolan, F. A. Beck and D. B. Fossan, Annu. Rev. Nucl. Part. Sci. **45**, 561 (1994).

[Nor50] L. W. Nordheim, Phys. Rev. **78**, 294 (1950).

[Nya89] B. M. Nyakó, J. Gizon, D. Barnéoud, A. Gizon, M. Józsa, W. Klamra, F. A. Beck, and J. C. Merdinger, Z. Phys. A **332**, 235 (1989).

[Pau00] E. S. Paul, P. Bednarczyk, A. J. Boston, C. J. Chiara, C. Foin, D. B. Fossan, J. Genevey, A. Gizon, J. Gizon, D. G. Jenkins, N. Kelsall, N. Kintz, T. Koike, D. R. LaFosse,

P. J. Nolan, B. M. Nyakó, C. M. Parry, J. A. Sampson, A. T. Semple, K. Starosta, J. Timár, R. Wadsworth, A. N. Wilson, and L. Zolnai, Nucl. Phys. **A676**, 32 (2000).

[Pet96] C. M. Petrache, D. Bazzacco, S. Lunardi, C. Rossi-Alvarez, G. De Angelis, M. De Poli, D. Bucurescu, C. A. Ur, P. B. Semmes, and R. Wyss, Nucl. Phys. **A597**, 106 (1996).

[PGAC] "*FMA Experimental Apparatus*" URL:http://www.phy.anl.gov/fma/apparatus.html

[Qua84] M. A. Quader, W. F. Piel, Jr., S. Vajda, W. A. Watson III, F. C. Yang, and D. B. Fossan, Phys. Rev. C **30**, 1772 (1984).

[Rad95] D. C. Radford, Nucl. Instrum. Methods Phys. Res. A **361**, 297 (1995); **361**, 306 (1995).

[Rad97] D. C. Radford, http://radware.phy.ornl.gov/incub8r3.html.

[Rad00] D. C. Radford, http://radware.phy.ornl.gov.

[Rai50] J. Rainwater, Phys. Rev. **79** 432 (1950).

[Rai76] J. Rainwater, Rev. Mod. Phys. **48** 385 (1976).

[RCA70] RCA *Photomultiplier Manual*, Technical Series PT-61, RCA Solid State Division, Electro-optics and Devices, Lancaster, PA, 1970.

[Rie01] L. L. Riedinger, D. J. Hartley, A. Galindo-Uribarri, B. H. Smith, C. Baktash, M. P. Carpenter, M. Danchev, M. Devlin, C. J. Gross, R. V. F. Janssens, M. Lipoglavsek, S. D. Paul, D. C. Radford, W. Reviol, D. G. Sarantites, D. Seweryniak, C.-H. Yu, and O. Zeidan, Acta Phys. Pol. B **32**, 2613 (2001).

[Rin80] P. Ring, and P. Schuck, *The Nuclear Many-Body Problem*, Springer Verlag, Berlin (1980).

[Ros67] H. J. Rose, and D. M. Brink, Rev. Mod. Phys. **39** 2 (1967).

[Sar96] D. G. Sarantites, P.-F. Hua, M. Devlin, L. G. Sobotka, J. Elson, J. T. Hood, D. R. LaFosse, J. E. Sarantites, and M. R. Maier, Nucl. Instr. Meth **A381** 418 (1996).

[Sat91] W. Satula, S. Ćwiok, W. Nazarewicz, R. Wyss, A. Johnson, Nucl. Phys.**A529**, 289 (1991).

[Sem90] P. B. Semmes, and I. Ragnarsson, Proc. Inter. Conf. Nuclear Structure of the nineties, Oak Ridge, Tennessee, Vol 1, p. 62 (1990).

[Sem91] P. B. Semmes, and I. Ragnarsson, Conf. future directions in nuclear physics with 4π detection systems of the new generation, Strasbourg, March 1991.

[Sew94] D. Seweryniak, J. Nyberg, C. Fahlander, and A. Johnson, Nucl. instrum. and Methods Phys. Res. A **340**, 353 (1994).

[Smi98] J. F. Smith, C. J. Chiara, D. B. Fossan, G. J. Lane, J. F. Lewicki, J. M. Sears, and P. Vaska, Phys. Rev. c **58**, 3237 (1998).

[Sta97] K. Starosta, Ch. Droste, T. Morek, J. Srebrny, D. B. Fossan, S. Gundel, J. M. Sears, I. Thorslund, P. Vaska, M. P. Waring, S. G. Rohoziński, W. Satula, U. Garg, S. Naguleswaran, and J. C. Walpe, Phys. Rev. C **55**, 2794 (1997).

[Sta01] K. Starosta, T. Koike, C. J. Chiara, D. B. Fossan, D. R. LaFosse, A. A. Hecht, C. W. Beausang, M. A. Caprio, J. R. Cooper, R. Krücken, J. R. Novak, N. V. Zamfir, K. E. Zyromski, D. J. Hartley, D. L. Balabanski, Jing-ye Zhang, S. Frauendorf, and V. I. Dimitrov, Phys. Rev. Lett. **86**, 971 (2001).

[Sta02] K. Starosta, C. J. Chiara, Ch. Droste, D. B. Fossan, T. Koike, T. S. Kuo, D. R. LaFosse, T. Morek, S. G. Rohoziński, and J. Srebrny, Phys. Rev. C **65**, 044328 (2002).

[Ste72] F. R. Stephens, and R. S. Simon, Nucl. Phys. **A183**, 257 (1972).

[Str67] V. M. Strutinski, Nucl. Phys. **A95**, 420 (1967).

[Str68] V. M. Strutinski, Nucl. Phys. **A122**, 1, (1968).

[Sve97] C. E. Svensson, J. A. Cameron, S. Flibotte, G. Gervais, D. S. Haslip, J. M. Nieminen, J. C. Waddington, J. N. Wilson, G. C. Ball, A. Galindo-Uribarri, V. P. Janzen, D. C. Radford, D. Ward, M. Cromaz, and T. E. Drake, Nucl. Instrum. Methods Phys. Res. A **396**, 228 (1997).

[Taj94] N. Tajima, Nucl. Phys. **A572**, 365 (1994).

[Tim00] J. Timár, A. Gizon, P. Paris, J. Genevey, J. Gizon, F. Hannachi, C. F. Liang, A. Lopez-Martens, J. C. Merdinger, B. M. Nyakó,B. Weiss, and L. Zolnai, Eur. Phys. J. A **7**, 7 (2000).

[Tim02] J. Timár, J. Gizon, A. Gizon, D. Sohler, B. M. Nyakó, L. Zolnai, D. Bucurescu, Gh. Cata-Danil, A. J. Boston, D. T. Joss, E. S. Paul, A. T. Semple, C. M. Parry, Acta Physica Polonica **33**, 493 (2002).

[Vaj83] S. Vazda, W. F. Piel, Jr., M. A. Quader, W. A. Watson, III, F. C. Yang, and D. F. Fossan, Phys. Rev. C **27**, 2995 (1983).

[Wys88] R. Wyss, J. Nyberg, A. Johnson, R. Bengtsson, and W. Nazarewicz, Phys. Lett. **B215**, 211 (1988).

[Wys89] R. Wyss, F. Lidén, J. Nyberg, A. Johnston, D. J. G. Love, A. H. Nelson, D. W. Banes, J. Simpson, A. Kirwan, and R. Bengtsson, Nucl. Phys. **A503**, 244 (1989).

[Wys90] R. Wyss, W. Satula, W. Nazarewicz, and A.Johnson, *Contribution to the Pittsburg Conference on High Spin States in γ-soft nuclei*, (1990).

[Yam67] T. Yamazaki, At. Data Nucl. Data Tables **A3**, 579 (1967).

[Xu00] F. R. Xu, Nucl. Phys. **A669**, 119 (2000).

[Zhe01] R. Zheng, S. Zhu, N. Cheng, and J. Wen, Phys. Rev. C **64**, 014313 (2001); and references therein.